



---

IDENTIFICATION OF  
EMERGING PATTERNS  
IN  
COMPLEX SYSTEMS

---

Vom Fachbereich Physik  
der Technischen Universität Darmstadt

zur Erlangung des Grades  
Doctor rerum naturalium (Dr. rer. nat.)

genehmigte Dissertation von  
M.Sc. Jan Wissmann  
aus Offenbach

Erstgutachter: Prof. Dr. Kay Hamacher  
Zweitgutachter: Prof. Dr. Benno Liebchen

DARMSTADT 2023

Wissmann, Jan : Identification of Emerging Patterns in Complex Systems  
Identifizierung emergenter Strukturen in komplexen Systemen  
Darmstadt, Technische Universität Darmstadt,  
Jahr der Veröffentlichung der Dissertation auf TUprints: 2024  
Tag der mündlichen Prüfung: 30.10.2023

Veröffentlicht unter CC BY-SA 4.0 International  
<https://creativecommons.org/licenses/by-sa/4.0/>

## Erklärungen laut Promotionsordnung

### §8 Abs. 1 lit. c PromO

Ich versichere hiermit, dass die elektronische Version meiner Dissertation mit der schriftlichen Version übereinstimmt.

### §8 Abs. 1 lit. d PromO

Ich versichere hiermit, dass zu einem vorherigen Zeitpunkt noch keine Promotion versucht wurde. In diesem Fall sind nähere Angaben über Zeitpunkt, Hochschule, Dissertationsthema und Ergebnis dieses Versuchs mitzuteilen.

### §9 Abs. 1 PromO

Ich versichere hiermit, dass die vorliegende Dissertation selbstständig und nur unter Verwendung der angegebenen Quellen verfasst wurde.

### §9 Abs. 2 PromO

Die Arbeit hat bisher noch nicht zu Prüfungszwecken gedient.

Darmstadt, den 10.07.2023

.....  
Jan Wissmann



# Abstract

Synchronization describes the onset of a common rhythm between two linear or chaotic oscillators. Originally, the research was developed around the observation of regular oscillators. Later, similar effects were described for coupled chaotic systems.

In early experiments, chaotic systems were limited to identical synchronization. However, it was found that more complex types of synchronization also develop for chaotic systems. Current research also continues to focus on identical synchronization. We assume that this is due to the easy accessibility of identical synchronization.

In this paper, we present an alternative, information-theoretical approach to synchronization detection. Mutual information has been used as an indicator of synchronization in previous work. However, we can establish and prove an accessible, formal relationship between synchronization and mutual information. With this insight, we propose *Synchronized Mutual Information* (SMI) as a measure of synchronization. This measure represents the coherence of two trajectories in the range of 0 to 1. With complete knowledge of the phase space, the upper bound of this measure then corresponds to a synchronized system.

In addition to this basic measure, we propose an efficient implementation for estimating the SMI. We test this implementation on a coupled Lorenz/Rössler system and compare it with the "Auxiliary System Method".

We also use the SMI in systems with many coupled chaotic oscillators. To obtain an assessment of the overall system, we propose different aggregations of the SMI and test them on examples from the literature.

In recent years, the focus of research has shifted from fully synchronized systems to partially synchronized systems. Effects such as interrupted synchronization, cluster synchronization, and chimera states are of particular importance. We can show that our measurement can also contribute to a more accessible research of these systems.

Unlike other tools, the SMI works without knowledge of the system dynamics and can also be used for analysis when the equations of motion are unknown. We can show that the results of the SMI are equivalent to the results of the Transversal Lyapunov Exponent, while the SMI has a much wider range of applications.

Finally, by analyzing real-world applications, we demonstrate the applicability of SMI to real-world data. We analyze historical stock prices of companies listed in the Dow Jones and try to identify de-

dependencies between companies using cluster analysis. We also apply the SMI to an *in-vitro* model of neurons. Observing neurons over a longer period of time, we determine how the degree of interconnection of neurons is reflected in their synchronization.

# Zusammenfassung

Synchronisation beschreibt das Einsetzen eines gemeinsamen Rhythmus zwischen zwei linearen oder chaotischen Oszillatoren. Ursprünglich entwickelte sich die Forschung rund um die Beobachtung regelmäßiger Oszillatoren. Wenig später wurden ähnliche Effekte auch für gekoppelte chaotische Systeme beschrieben.

In frühen Experimenten beschränkte man sich bei chaotischen Systemen auf identische Synchronisation. Es wurde jedoch festgestellt, dass sich für chaotische Systeme auch komplexere Arten der Synchronisation ausbilden. Auch die aktuelle Forschung konzentriert sich weiterhin auf identische Synchronisation. Wir vermuten, dass dies auch an der einfachen Zugänglichkeit der identischen Synchronisation liegt.

In dieser Arbeit stellen wir einen alternativen, informationstheoretischen Ansatz zur Erkennung von Synchronisation vor. Transinformation wurde bereits in früheren Arbeiten als Indikator für Synchronisation verwendet. Wir können jedoch eine zugängliche, formale Beziehung zwischen Synchronisation und Transinformation herstellen und beweisen. Mit dieser Erkenntnis schlagen wir die *Synchronized Mutual Information* (SMI) als Maß für Synchronisation vor. Dieses Maß repräsentiert die Kohärenz zweier Trajektorien in einem Bereich von 0 bis 1. Bei vollständiger Kenntnis des Phasenraums entspricht die obere Schranke dieses Maßes dann einem synchronisierten System.

Neben diesem grundlegenden Maß schlagen wir eine effiziente Implementierung zur Schätzung des SMI vor. Wir testen diese Implementierung an einem gekoppelten Lorenz/Rössler-System und vergleichen sie mit der "Auxiliary System Method".

Wir verwenden die SMI auch in Systemen mit vielen gekoppelten chaotischen Oszillatoren. Um eine Beurteilung des Gesamtsystems zu erhalten, schlagen wir verschiedene Aggregationen der SMI vor und testen diese an Beispielen aus der Literatur.

In den letzten Jahren hat sich der Fokus der Forschung von vollständig synchronisierten Systemen hin zu teilweise synchronisierten Systemen verschoben. Dabei sind Effekte wie unterbrochene Synchronisation, Clustersynchronisation und Chimärenzustände von besonderer Bedeutung. Wir können zeigen, dass unsere Messung auch hier einen Beitrag zur einfachen Erforschung dieser Systeme leisten kann.

Im Gegensatz zu anderen Werkzeugen arbeitet die SMI ohne Kenntnis der Systemdynamik und kann auch zur Analyse verwendet werden, wenn die Bewegungsgleichungen unbekannt sind. Wir können zeigen, dass die Ergebnisse der SMI in den Ergebnissen des Transversalen Lyapunov-Exponenten entsprechen, während die SMI einen

viel größeren Anwendungsbereich hat.

Schließlich demonstrieren wir die Anwendbarkeit des SMI auf reale Daten, indem wir praktische Anwendungen analysieren. Wir analysieren historische Aktienkurse von im Dow Jones gelisteten Unternehmen und versuchen mittels einer Clusteranalyse Abhängigkeiten zwischen den Unternehmen herauszuarbeiten. Außerdem wenden wir den SMI auf ein *in-vitro* Modell von Neuronen an. Indem wir die Neuronen über einen längeren Zeitraum beobachten, stellen wir fest, wie sich der Vernetzungsgrad der Neuronen in der Synchronisation zwischen ihnen niederschlägt.



# Contents

Abstract	5
Zusammenfassung	7
<b>1 Complex Systems &amp; Synchronization</b>	<b>1</b>
1.1 Chaos	4
1.2 Synchronization between Chaotic Systems	9
<b>2 Novel Synchronization Measure</b>	<b>15</b>
2.1 Introduction to Information Theory	16
2.2 Information Theory and Deterministic Systems	19
2.3 Mutual Information in the Presence of Synchronization	20
2.4 Synchronous Mutual Information	24
2.5 Types of Synchronization	26
2.6 Estimating Mutual Information and Entropy	27
<b>3 Chaos &amp; Synchronization</b>	<b>35</b>
3.1 Driver/Response System	35
3.2 Linear Chain of Logistic Maps	41
3.3 General Remarks	50
<b>4 Partial Synchronization &amp; Complex Networks</b>	<b>51</b>
4.1 SMI and Partial Synchronization	53
4.2 Intermittent Synchronization	55
4.3 Cluster Synchronization	56
4.4 Chimera States	58
4.5 Nondeterministic Synchronization	64

<b>5</b>	<b>Synchronization in Real-World Systems</b>	<b>69</b>
5.1	Synchronization in Stock Markets	70
5.2	Synchronization of Neuronal Systems	79
<b>6</b>	<b>Discussion &amp; Outlook</b>	<b>87</b>
6.1	Advantages and Limitations of the SMI	90
6.2	Outlook	91
<b>A</b>	<b>Appendix</b>	<b>93</b>
A.1	Maximum Lyapunov Exponent	94
	<b>Bibliography</b>	<b>95</b>

# Complex Systems & Synchronization

# 1

„Everything is interaction“[Hum]h) was stated by Humboldt on his journey through South America where he observed that each living species is dependent on another. His observations laid the foundations for our modern studies of complex ecological networks [Fräo1]. This thesis is embedded in the field of complex systems theory, a field concerned with understanding interconnected systems.

Local—and seemingly minuscule—variations give rise to properties being lost in the ‘traditional’ methods of statistical mechanics. The significance of even small perturbations makes these systems notoriously hard to access with established quantitative methods. Nevertheless, many common phenomena emerge from these interactions. Although reliable long-term predictions remain challenging, advances in complexity theory help us to find meaningful models and properties of these systems. The field explores new frameworks to understand and describe systems where the dynamics emerging from the interactions is not well explained by the dynamics of the components themselves.

The insights gained within complexity theory find application in various disciplines, spanning from engineering to climate research to biology. Some examples include:

1. Power grids show many properties of a complex system. Quick localized changes in power production and consumption and line failures combined with the sensitivity to load changes of power plants result in a fragile setup that requires constant and rapid balancing. The decentralized structure and feedback loops, e.g. line failures, make central control of the structure a difficult problem. We might be able to build robust power grids at lower prices with insights gained from complexity theory [Sal18].
2. Microclimates depend on various input variables. Small fluctuations in some areas can lead to the breakdown of the mid-winter polar vortex, drastically changing the weather for many areas of the world. Local weather phenomena depend greatly on the state



Figure 1.1: Birds flying in a flock organize themselves by keeping a certain distance from each of their neighbors. With simple rules, they can create complex and rich patterns, implying a complex set of rules.

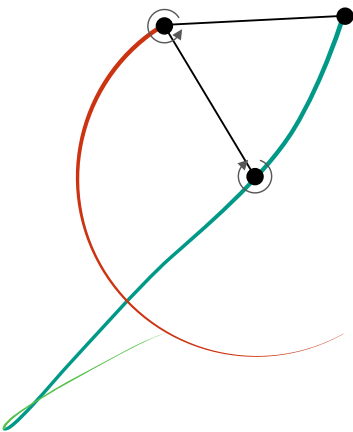


Figure 1.2: Trajectories of a double pendulum. Although its mechanical setup is simple, long-term predictions of position and speed are complicated. Small errors in friction, speed, and position result in large phase space variations.

of global phenomena. For example, the breakdown of the polar vortex in winter can quickly push otherwise stable weather in Europe and northern America on different attractors, allowing either for an early spring or deep cold winters [Law18; Gra20].

3. Migrating birds often organize themselves in flocks, forming large patterns in the sky (see Figure 1.1). These flocks appear as if the birds were following a single leader. However, rather than being guided by a central entity, their formations are the result of localized decisions made by each individual bird, based only on their immediate neighbors and nearby obstacles [Chr14].

The most impressive system is our brain. It allows us to explore and predict our environment, including discovering, exploring, and documenting the systems mentioned above. The complexity and plasticity of our brains arise from a network of many billion neurons. Mean-field theories, which lose the detail of interaction between neurons, cannot explain the observed patterns of human expression. Measurement of aggregated quantities of neuron dynamics can only offer superficial insight into the working mind. Our behavioral patterns do not emerge from scaled-up dynamics of isolated neurons, but from the coupling and interaction between neurons, formed by evolution, experience, and current environmental input [Gro13; Chi10, p. 321].

For complex systems, some scientists see the reductionist approach as failing [Maz08; Rego4]. Studying isolated objects must fail when the desired macroscopic properties emerge from interactions between the components of a system, rather than the dynamics of isolated components. While we might be able to overcome these limitations by building larger models, computational power is limited. Even now, the long-term prediction of a double pendulum (see Figure 1.2) is under active research [Vau10; Ouy20]. Coupling 100s of double pendulums and predicting their dynamics should exhaust even the strongest computers. Except that sometimes it does not.

When coupling two self-propelled systems, we can observe—under certain circumstances—that both systems converge on a common beat. At a critical coupling strength, the two systems will rapidly transition from a decoherent state to a synchronized state. In this synchronized state, the dynamics of the two systems often appear as if driven by a common third system. It can be observed in the pulsed flashing of fireflies, Mexican waves in the stadium or in firing patterns of neurons [Lop91; Gue17; McB15; Ram19; Pro20].

As with other complex systems, a small perturbation is the key to a new macroscopic phenomenon. A class of self-propelled oscillators with high sensitivity for small perturbations are chaotic systems. For a chaotic oscillator, points in phase space will diverge exponentially, even for small perturbations. Intuition dictates that this should make them bad candidates for synchronization. In practice, we find that coupled chaotic oscillators are not only capable of synchronization

but that these systems produce a rich zoo of synchronization types.

An introduction to complex system theory can be found in [Gro13]. See [Gono4; Boc18] for a general introduction to synchronization and [Pec15a] for a short history of the synchronization of chaotic systems.

In this work, we will propose a measure to reliably identify synchronization in simulated and real-world data. For the application of the measure, we focus on the synchronization of chaotic systems. We propose a novel 0-1 bound measure to detect synchronization between coupled components. The measure is first applied to systems taken from previous work. We compare the performance of our measure to two existing measures and discuss limitations and advantages. We argue that our approach follows a natural interpretation of synchronization and also give formal proof for this intuition.

Indeed, similar measures have been successfully applied in the past [Pal01; Ame15]. However, we could not find any existing work showing the equivalence between these methods and other definitions of synchronization. We extend previous work by providing a formal proof of the equivalence of these methods and synchronization.

Our method is designed as a plug-in method. Its implementation is independent of the dynamics of the systems, the user's only input being adequately sampled data. With the measure being constructed from common methods in information theory, it will benefit from future advances in Shannon entropy or MI estimators.

To benchmark and compare the measure, we apply it to various systems. We show that it can reliably detect synchronization in driver/response systems composed of a Lorenz and Rössler system. By applying it to a ring of logistic maps, we also show its performance on chaotic maps and larger systems.

Since the early work in the 1990s, research has shifted from studying fully synchronized systems to partial spatial and/or temporal synchronization. The measure is not limited to two-component or fully synchronized systems. We also explore the feasibility of partially synchronized, noisy, and real-world systems. Here, we can see that the measure can reliably distinguish between emerging synchronization and spurious correlations. We reconstruct mutual dependencies between Dow Jones listed companies by evaluating the correlations in historical stock indexes. We use the measure to show the emergence of synchronization between neurons, forming connections in an *in-vitro* model of hippocampal neurons.

The remainder of this chapter is dedicated to the introduction of basic concepts in chaotic systems and synchronization. In the second chapter, we will also present a few concepts of information theory as a starting point for further discussion of the properties of our measure.

## 1.1 Chaos

Chaotic systems produce observables with seemingly unordered or random states and can experience irregular oscillations. Non-linear behavior and feedback loops make these systems sensitive to their initial conditions. This means that small perturbations induce divergent trajectories. This sensitivity makes them hard to predict and often prevents comprehensive analytical analysis [Boc18, p. 5]. In contrast to systems with stochastic variables, however, chaotic systems have no random components. Being fully deterministic, identical initial conditions will return identical trajectories.

Early reports on chaotic systems date back to Poincarè [Oes07]. He found that ODEs with more than two dimensions could experience instability. However, since these systems must be studied numerically, with little available computational power, analysis of such models was impractical at that time. In the 1960s, Lorenz found that predictions from his weather model would change drastically with only a single small perturbation applied to intermediate results [Oes07].

Lorenz further explored his findings and was able to come up with an ODE consisting of three equations that could replicate the sensitivity observed in his model, [Lor63]. This matched the spirit of the time, as scientists from other disciplines reported similar behavior. In Russia, Chirikov explored the non-linear resonance of trapped particles in magnetic fields [Chi60] and Ruelle and Takens investigated turbulent flow [Rue71]. With the increased amount of computational power, the previous infeasible analysis could be conducted.

A chaotic system can be identified by its positive maximum Lyapunov exponent. Furthermore, we introduce three systems with chaotic behavior. In Section 1.1.2, the logistic map is introduced as an example for discrete systems, with the Lorenz and Rössler attractors, and two examples for continuous chaotic systems are presented in Section 1.1.3 and Section 1.1.4. All three systems are applied later in this thesis.

### 1.1.1 Lyapunov Exponent

To evaluate the sensitivity of a system to initial conditions, we can observe the distance between two trajectories  $z_1(t)$ ,  $z_2(t)$  in their phase space  $\mathbf{Z}$ . We place the starting points  $z_1(0)$  and  $z_2(0)$  close to each other and then track their distance  $|\delta z(t)|$ .

A comparison of their initial distance allows us to evaluate the stability of the system. The time dependency of the distance can be estimated by

$$|\delta z(t)| \sim e^{\lambda t} |\delta z_0| \quad (1.1)$$

where we call  $\lambda$  Lyapunov exponent. Unstable or chaotic systems are characterized by a positive Lyapunov exponent  $\lambda > 0$ . A van-

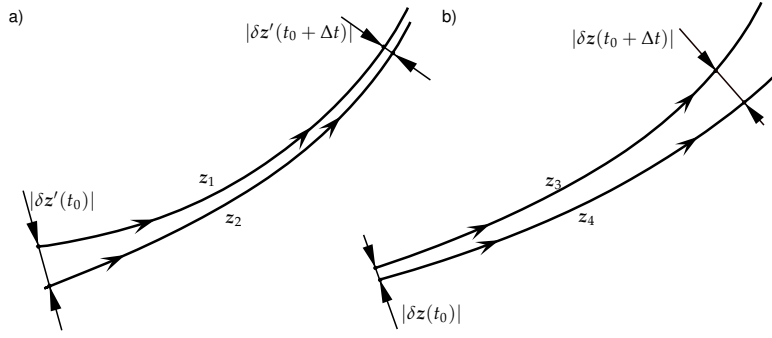


Figure 1.3: In chaotic systems, two trajectories  $z_3$  and  $z_4$  with similar initial conditions will diverge over time. In non-chaotic systems, in the same type of setup, the trajectories  $z_1$  and  $z_2$  converge. The plots show a non-chaotic system in a) and a chaotic one in b). The distance at time  $t_0 + \Delta t$  can be estimated by the Lyapunov exponent  $|\delta z(t_0 + \Delta t)| = e^{\lambda(t_0 + \Delta t)} |\delta z(t_0)|$ . For system a) the exponent is  $\lambda_a < 0$ , in system b)  $\lambda_b > 0$ .

ishing exponent indicates a non-chaotic system, where trajectories in systems with negative  $\lambda$  converge [Hir13, p. 209]. In Figure 1.3 we compare a stable with a chaotic system. As we see, the distances between the trajectories increase.

For multidimensional systems, each dimension is characterized by its own  $\lambda$ , thus in  $n$  dimensions, we obtain  $n$  Lyapunov exponents. For our purposes, only the maximum Lyapunov exponent of the spectrum is of interest. It alone determines whether the system is in a chaotic or linear regime. If any component of the Lyapunov spectrum is positive, its exponential growth will quickly dictate the overall distance, resulting in a chaotic system.

The maximum Lyapunov exponent can be defined as [Kan94]

$$\lambda = \lim_{t \rightarrow \infty} \lim_{|\delta z(0)| \rightarrow 0} \frac{1}{t} \log \frac{|\delta z(t)|}{|\delta z(0)|}. \quad (1.2)$$

As in practice, Lyapunov exponents can rarely be retrieved analytically. Various numerical techniques have been established to estimate the exponents. In Appendix Section A.1 we show an approach to calculate the maximum Lyapunov exponent for a discrete map.

The algorithm, first described in [Ben76], tracks the distance between two maps. Similarly to Equation (1.2), it calculates the Lyapunov exponent by normalizing the later distance  $\delta z(t)$  with the initial  $\delta z(0)$ . Due to the finite precision of computers, the implementation avoids the vanishing limit for the initial distance. For the same reason, larger distance values are also avoided. A threshold resets the system to the initial distance, preserving the direction between the systems.

### 1.1.2 Logistic Map

Originally constructed as a discrete-time model for population growth, the logistic map is now a common tool for creating chaotic patterns. The map is defined by

$$x[t + 1] = rx[t](1 - x[t]) \quad (1.3)$$

with its only parameter  $r$  in  $[0, 4]$ . The notation  $x[t]$  for time series with discrete time steps will be used throughout this thesis. As a

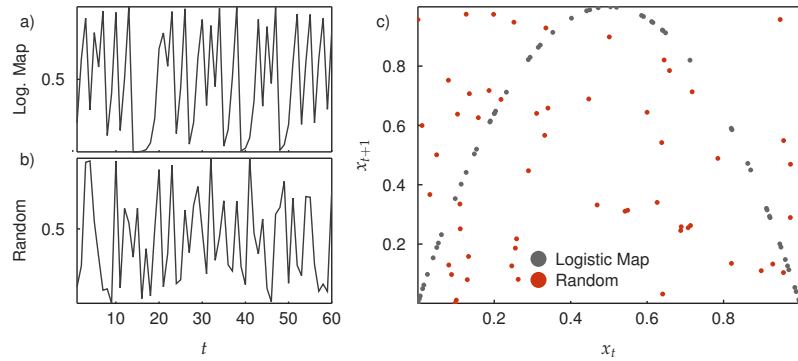
population model, it is bound between 0 and 1. Values outside this range diverge.

In contrast to a continuous version, the discrete logistic map experiences chaotic behavior for certain parameters. For most  $r > 3.57$  the logistic map is in the chaotic regime.

The logistic map also allows us to display the difference between chaos and randomness. In Figure 1.4 we compare a logistic map alongside a series of random values in  $[0, 1]$ . In Figure 1.4 a) and b) we compare the values as a function of step or time  $t$ . In this view, there is no noticeable difference between the two trajectories. However, we can uncover the deterministic structure of the logistic map with a Poincaré plot in Figure 1.4 c). By plotting consecutive pairs  $(x_t, x_{t+1})$  we catch the pattern that creates the logistic map. The series of random values on the other hand show no or only spurious structure <sup>1</sup>.

<sup>1</sup>The random values in this example are not truly random but were generated with a Mersenne-Twister algorithm. Incidentally, the quality of generators for pseudo-random numbers can be accessed by a high-dimensional Poincaré plot. [Knu97, p.93]

Figure 1.4: The difference between a chaotic and a random system is only obvious with the right representation of the data. We have generated a time series from a logistic map in the chaotic regime ( $r = 4$ ) in a) and compare it with a time series of (pseudo-)randomly chosen points in b). The values of the random time series are normalized such that their minimum value is 0 and their maximum is 1. Only in the Poincaré plot in c) can we see a qualitative difference between the two series. The points generated from the logistic map all lie on a quadratic curve, while we find no order for the random point.



### 1.1.3 Lorenz Attractor

The Lorenz attractor was first introduced in [Lor63]. Having been created as a simple system to study the chaotic behavior found in earlier weather models, the Lorenz attractor is still in use today to study chaotic dynamics.

The model was derived from equations that describe the velocity of an incompressible viscous fluid between two plates. The temperature difference between the plates create a density gradient which then, with the gravitational forces, leads to a movement of the fluid.

The dynamics of a Lorenz system are given by [Lor63]

$$\begin{aligned} \frac{d}{dt}x_1 &= \sigma(x_2 - x_1) \\ \frac{d}{dt}x_2 &= x_1(r - x_3) - x_2 \\ \frac{d}{dt}x_3 &= x_1x_2 - bx_3 \end{aligned} \quad (1.4)$$

with the parameters  $r$ ,  $b$  and  $\sigma$  all positive. The system is not chaotic for all parameters. Parameters for which chaos is observed can be



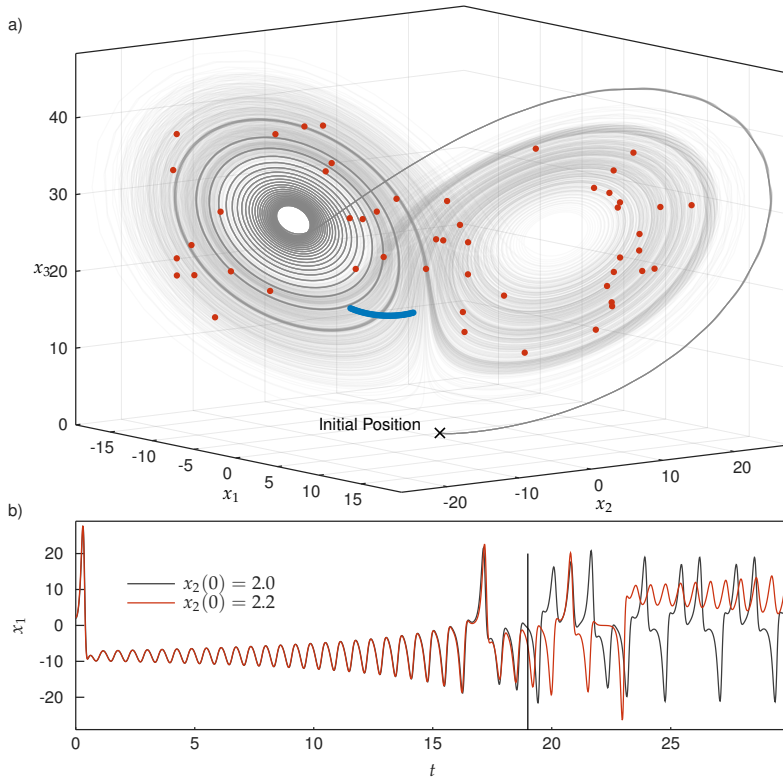


Figure 1.5: Despite similar initial conditions, trajectories in a Lorenz system quickly diverge after some time. An ensemble of trajectories was created with the initial conditions  $x_1(0) = x_3(0) = 0$  and  $x_2(t)$  randomly chosen in  $[2.0, 2.2]$ . The system is shown in a). The initial positions are marked with  $\times$ , their positions at  $t \sim 20$  are marked with a blue, and the positions at the end of the simulation with a red dot. With the blue dots, we can observe that while the trajectories are still similar, the distance between them has already grown. In the final position of this calculation, their states are distributed throughout the phase space. This divergence can also be observed in b) where we have plotted only the  $x_1$  axis for the initial conditions  $x_2(0) = 2.0$  and  $x_2(0) = 2.2$ . The line near  $t = 20$  marks the same time as the blue dots in a). In b), we can see how both trajectories are in close proximity until they separate around  $t \sim 20$  and then quickly diverge and show different oscillation patterns.

found in the literature, e.g. in the original work [Lor63] or the values taken in the example in Figure 1.5.

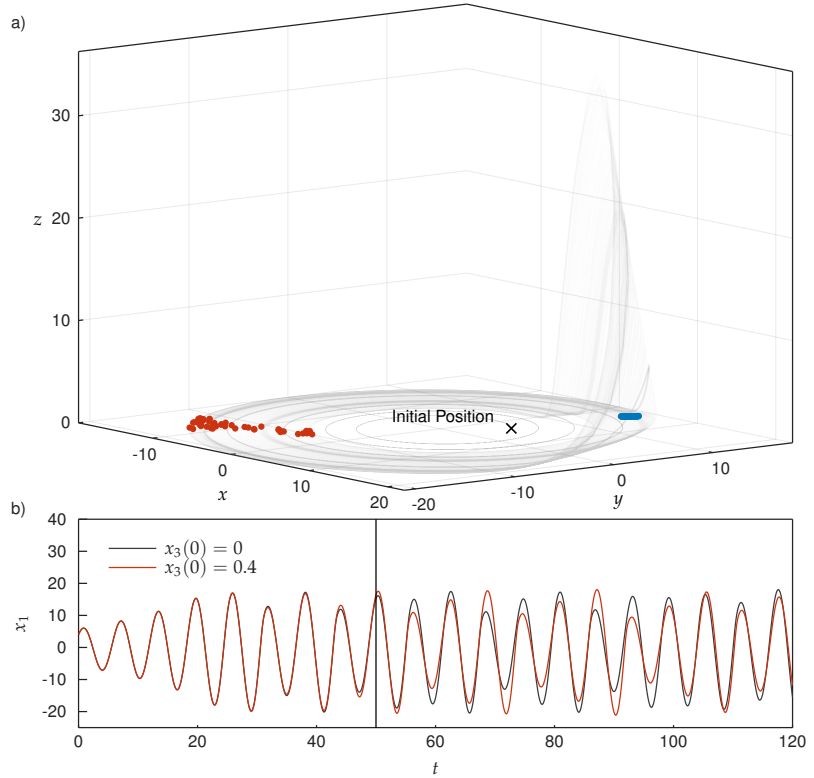
For a further analysis of the Lorenz system, we refer the reader to a detailed analysis in, e.g. [Hiro4]. It shows that the two attracting points we see in Figure 1.5 exist only for  $r > 1$ . Smaller  $r$  will result in a single origin that acts as a sink for the trajectory [Hir13].

In Figure 1.5, we show two trajectories for the Lorenz system with the parameters  $\sigma = 10$ ,  $b = 8/3$ ,  $r = 28$  taken from the original work [Lor63]. For the initial values  $(x_1, x_2, x_3)$  we have chosen values between  $(0, 2, 0)$  and  $(0, 2.2, 0)$ . In Figure 1.5 a) we see that all trajectories start very close from each other. However, they quickly diverge, and after a short amount of time, their positions are scattered all over the attractors.

This becomes even more clear when we look at Figure 1.5 b) where the  $x_1$  component is shown for two initial values  $x_2(0) = 2.0, 2.2$ . The dynamics of both trajectories starts out to be almost indistinguishable. However, at about  $t = 18$  we see that the trajectories begin to diverge, showing a very different behavior as the trajectories begin to oscillate between and within the two attractors. In situations where we can only estimate the initial parameters with finite precision, long-term predictions of the behavior will fail.

The dynamical systems in Figure 1.5 a) and b) were created with Julia (Version 1.5) [Bez17] using a Runge-Kutta solver, more specifically the Tsit5 solver provided with [Rac17].

Figure 1.6: The Rössler system provides more minimal dynamics while preserving the chaotic behavior of the Lorenz system. Trajectories are simulated with initial conditions  $x_1(0) = x_2(0) = 4$  and  $x_3$  randomly chosen in  $[0, 0.4]$ . In a) we show their behavior in 3D. Similar to the plot of the Lorenz attractor in Figure 1.5, the trajectories diverge over time. While all trajectories have their origin at the position marked  $\times$ , they spread out over the phase space. Blue shows that the trajectories are relatively tightly packed, while the red dots at the end of the simulation are scattered throughout the attractor. In b) we compare the  $x_1$  axis of two trajectories with initial conditions  $x_3(0) = 0$  and  $x_3(0) = 0.4$ . We also show the position of the blue points with the vertical line near  $t = 50$ . We see how the trajectories are very close in the beginning but diverge around  $t \sim 50$ . Their phases seem to be stable, but as we see with the red dots in a), the phase correlation also decays.



#### 1.1.4 Rössler Attractor

Another common system for the creation of chaos is the Rössler attractor [Rös76], inspired by the visuals of the Lorenz system, Rössler created an attractor with only a single fix point [Let10]. The equations of motion for the system are given by

$$\begin{aligned} \frac{d}{dt}x_1 &= -x_2 - x_3 \\ \frac{d}{dt}x_2 &= x_1 + ax_2 \\ \frac{d}{dt}x_3 &= p + x_3(x_1 - \mu). \end{aligned} \quad (1.5)$$

with its parameters  $a, p, \mu$ . The parameters often used to achieve chaos are  $a = 0.1, p = 0.1$ , and  $\mu = 28$ . In Figure 1.6 we see an ensemble of trajectories for the above parameters with different initial values. Figure 1.6 a) shows the evolution of the trajectories over time, where the initial tight ensemble quickly diverges.

Figure 1.6 b) shows the  $x_1$  component. In contrast to the Lorenz system, the Rössler system settles on a single attractor. Its defining visual feature is the strong slope for trajectories farther away from the attractor. As with the Lorenz attractor, we see that with increasing time  $t$  the trajectories from both initial values start to diverge.

The dynamical systems in Figure 1.6 a) and b) were created with Julia (Version 1.5) [Bez17] using a Runge-Kutta solver, more specifically the Tsit5 solver provided with [Rac17].

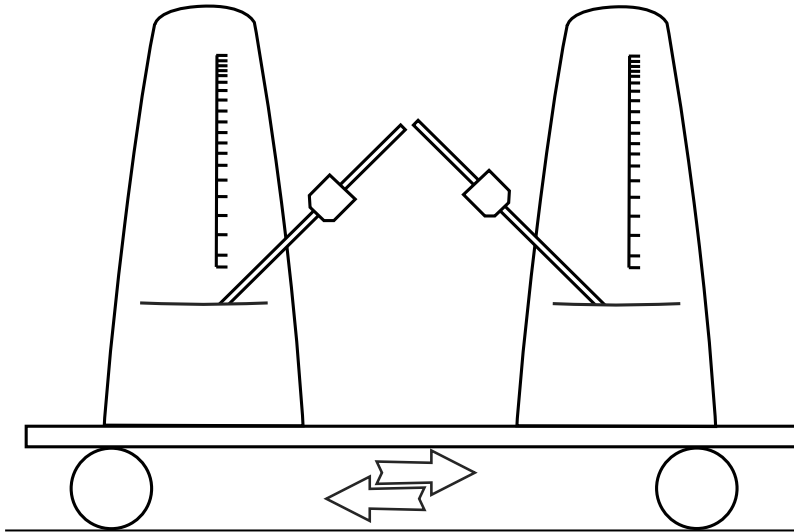


Figure 1.7: A variation of Huygens' experiment to synchronize pendulum clocks. Two mechanical metronomes are placed on a board that pivots on two free wheels. The wheels allow the board to move freely and thus transmit the momentum of the swinging pendulum. This ultimately results in the synchronization of the metronomes.

## 1.2 Synchronization between Chaotic Systems

In this section, we give a brief introduction to the notion of synchronization and an overview of the various interpretations of synchronization used in this work. For a more exhaustive introduction to the synchronization of chaotic systems, we refer to [Pik01; Gon04; Boc18].

The first report on the synchronization of oscillators dates back to Huygens in the 1700s [Oli15]. He found that his pendulum clocks would synchronize when installed on a wooden beam. In his time, the clocks would quickly run out of phase with each other. However, the small momentum transferred in the beam was enough to establish a fixed phase shift between the clocks. A variation of Huygens' experiment is depicted in Figure 1.7.

In 1975 Kuramoto started modern research on synchronization when he was able to derive a mathematical model of phase oscillators that settled on a common frequency under weak coupling [Kur75].

While unlikely candidates, it was soon found that synchronization could also be observed between chaotic systems. Early work in this field dates back to [Fuj83] and gained some momentum with the application of chaotic systems to transmit secret messages [Pec90]. A brief history of chaotic synchronization by one of its pioneers can be found in [Pec15b]. Various types of (chaotic) synchronization have been found and unified in a framework [Boc01].

Results from the synchronization of chaotic systems have been used in control theory. By applying small perturbations in the non-synchronous system, a desired state can be maintained [Boc00; Fra05]. The methods developed here were also used to analyze mental states

in the brain [Nato4].

Since Lorenz's research on weather prediction, chaos theory plays a major role in the analysis of weather models. The most immediate impact was the realization that the predictions must be calculated in ensembles [Sli11]. Other approaches showed how seasonal predictions could be made [Pal93], avoiding precise daily predictions and favoring trends. The infrequent breakdowns of the polar vortex bifurcation points are typical to chaotic systems where the weather for the next period can settle on different attractors [Cám19].

Synchronized chaotic systems were proposed to transmit secret messages. Early work on the topic boosted research in the synchronization of chaotic systems. While the field is still under active research, the focus has shifted from electrical to optical transmission [Pec15a; Yao17; Ucho5].

The most general (continuous) equation for synchronized two-component systems can be written as

$$\begin{aligned}\frac{d}{dt}x_1 &= F_1(x_1) - K_1(x_1, x_2) \\ \frac{d}{dt}x_2 &= F_2(x_2) - K_2(x_2, x_1)\end{aligned}\tag{1.6}$$

with  $F_i$  describing the dynamics of each system and  $K_i$  some coupling function.

In this work, we will focus on *diffusive* coupling, which corresponds to one-dimensional coupling function

$$K_i(x_1, x_2) = c_i(x_1 - x_2) .\tag{1.7}$$

In Section 3.1, we apply a unidirectional coupling scheme, also called master-slave coupling. Here, only one of the systems receives feedback from its partner, we can write this as

$$\begin{aligned}\frac{d}{dt}x_1 &= F_1(x_1) \\ \frac{d}{dt}x_2 &= F_2(x_2) - c(x_2 - x_1) .\end{aligned}\tag{1.8}$$

Although the previous section has different attractors for each component, in Section 3.2 we investigate a larger system with identical oscillators. It is a multi-component system and we extend Equation (1.6) as

$$\frac{d}{dt}x_i = F(x_i) - \sum_j L_{ij}c(x_i - x_j) .\tag{1.9}$$

The coupling between the components is in the elements of the weighted adjacency matrix  $L_{ij}$  with  $L_{ii} = 0$ .

In Chapter 4 we will go beyond these simple coupling schemes of Chapter 2 and look at complex networks. While the underlying mechanics of synchronization are generally well understood, the stability of noisy systems and identification of synchronized states is still under active research [Kat20; Tim18].

This section will introduce some of the known types of synchronization and give a short overview of the unifying framework. From this we will later be able to construct a novel measure and show its features on typical coupled chaotic systems.

### 1.2.1 Identical Synchronization

In systems with identical attractors and mutual coupling, we can observe Identical Synchronization (IS). We can rewrite the equations of motion of Equation (1.6) and obtain

$$\begin{aligned}\frac{d}{dt}\mathbf{x} &= \mathbf{F}(\mathbf{x}) - c(\mathbf{x} - \mathbf{y}) \\ \frac{d}{dt}\mathbf{y} &= \mathbf{F}(\mathbf{y}) - c(\mathbf{y} - \mathbf{x}).\end{aligned}\tag{1.10}$$

Systems experience IS when there exists at least one trajectory such that  $x(t) = y(t)$ . In [Fuj83] the authors find that the Lyapunov exponent can be used to determine whether a system experiences IS.

Similarly to the Lyapunov exponent for chaotic systems in Section 1.1.1, it is used here to predict the divergence of both states. If the maximum Lyapunov exponent for  $x(t) = y(t)$  is positive, the two trajectories diverge and we cannot have identical synchronization. If it is negative, the identical state is attracting, and the system is synchronous.

Although IS can be analyzed analytically for some cases (e.g. [Fuj83; Ant17]), in most cases, we have to study IS numerically.

### 1.2.2 Generalized synchronization

Synchronization in regular oscillators is identified via their phase relation. This allows the synchronization to be identified with offsets or different amplitudes. Chaotic systems generally do not have a well-defined phase, so in early work synchronization could only be identified between identical trajectories (IS). This made it impossible to identify synchronization between non-identical oscillators.

In [Rul95] an approach was proposed to evaluate synchronization between a driver-response system

$$\begin{aligned}\frac{d}{dt}\mathbf{x} &= \mathbf{F}_1(\mathbf{x}) \\ \frac{d}{dt}\mathbf{y} &= \mathbf{F}_2(\mathbf{y}) - c(\mathbf{y} - \mathbf{x})\end{aligned}\tag{1.11}$$

where  $\mathbf{y}$  can act as a proxy of  $\mathbf{x}$ .

Since the dynamics of both systems are different, the trajectories will not converge for typical coupling values.

According to [Rul95] two systems are synchronized when there exists a function for all  $t$

$$\boldsymbol{\phi}(\mathbf{x}(t)) = \mathbf{y}(t).\tag{1.12}$$

We will call  $\phi$  the *synchronization function*. This aptly named Generalized Synchronization (GS) would apply in all cases where a unique relation from the driver to the response system could be found. IS remains as a special case of GS where the synchronization function  $\phi$  is the identity.

Typical approaches for stability analysis as the conditional Lyapunov exponent do not work for GS. Other methods such as the auxiliary system method were proposed in [Aba96]. In Chapter 2 we will use this method to derive a method to easily identify systems with GS.

### 1.2.3 Attempts on Unifying Theories

Next to IS and GS, various additional types of synchronization were discussed. This includes phase [Pik97], anticipated synchronization [Mas01] and lag synchronization [Ros97].

To define some common ground for synchronization, some attempts to unify the definitions were initiated. In this work, we focus on the framework proposed in [Boc01], extending the idea in [Bro00].

From the work in [Boc01] we can derive the previously mentioned types of synchronization as special cases of their definition. We will develop these ideas further and show that the so-called mutual information is related to this abstract notion of synchronization and the definitions of [Aba96].

Similar to GS, the unified framework considers that two trajectories must be synchronized, if there exists a synchronization function  $\phi$ . In contrast to GS, the requirement for a synchronization function is relaxed. It must only exist in an invertible projected phase space of both trajectories. Transformation of the phase space allows for other types of synchronization beyond GS.

We assume a phase space  $Z \in \mathbb{R}^{m_1+m_2}$  with its (mutually exclusive) subsets  $X \in \mathbb{R}^{m_1}$  and  $Y \in \mathbb{R}^{m_2}$ . Two trajectories  $x \in X$  and  $y \in Y$  form a joint trajectory  $z$  within the phase space. We assume that if we can find a unique projection from  $x$  to  $y$ , the systems are synchronous. This is complicated when our trajectory is curved and we have no homeomorphism between  $x$  and  $y$ . An illustration of the problem is shown in Figure 1.8. With a diffeomorphism  $\mathcal{F} : Z \in \mathbb{R}^{m_1+m_2} \mapsto W \in \mathbb{R}^{d_1+d_2}$  we can straighten out the manifold.

In the new space  $W$  we can find a function  $\phi$  between the points. Any point  $\tilde{x}$  can then be transformed into  $W$ , and with the function  $\phi$  we can find the corresponding  $\tilde{y}$ . As the projection  $\mathcal{F}$  between the spaces is invertible, we can find the parameters of the projection in the original phase space. Although the synchronization function exists only in  $W$ , the corresponding pairs can still be found due to the diffeomorphism  $\mathcal{F}$ .

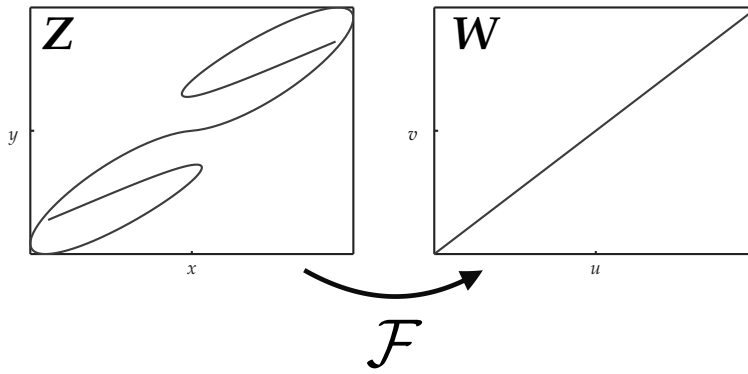


Figure 1.8: A curved manifold is straightened out (Adapted from [Boc01]). A diffeomorphism  $\mathcal{F}$  is used to "flatten" the points in  $Z$  so that for each value  $u$  in  $W$  we can find a  $v$  via  $\phi(u) = v$ . The diffeomorphism between  $Z$  and  $W$  allows us to project the pair of  $(u, v)$  back to  $(x, y)$ .

Boccaletti [Boc01] requires the components of the  $W$  space dimension  $d_1$  and  $d_2$  to be smaller or equal to their counterparts  $m_1$  and  $m_2$ . We construct two additional projections  $\mathcal{P}_1 : \mathbb{R}^{d_1+d_2} \mapsto \mathbb{R}^{d_1}$  and  $\mathcal{P}_2 : \mathbb{R}^{d_1+d_2} \mapsto \mathbb{R}^{d_2}$ . These give us the subsets  $\mathbf{U} \in \mathbb{R}^{d_1}$  and  $\mathbf{V} \in \mathbb{R}^{d_2}$ . A system is then defined as synchronous if the previous transformation and an additional function  $\phi : \mathbf{U} \mapsto \mathbf{V}$  exist.

Next, we will look at the exact definition of the synchronization function  $\phi$ . In Section 1.2.2 we introduced a synchronization function for the definition of GS. Due to the conceptual and practical similarities, we will keep the symbol and the name here. We call  $\phi$  a synchronization function when for any point on the trajectory  $(\tilde{\mathbf{u}}, \tilde{\mathbf{v}})$

1.  $\phi(\tilde{\mathbf{u}}) = \tilde{\mathbf{v}}$
2.  $\phi$  is continuous at  $\tilde{\mathbf{u}}$
3. from having a pair  $\varepsilon$  and  $\delta$  that satisfies a relation where  $|\mathbf{u} - \tilde{\mathbf{u}}| < \delta$  implies  $|\phi(\mathbf{u}) - \tilde{\mathbf{v}}| < \varepsilon$ , then for this pair  $(\varepsilon, \delta)$  it follows that if  $|\mathbf{u}(t) - \tilde{\mathbf{u}}| < \delta$ , then  $|\mathbf{v}(t) - \tilde{\mathbf{v}}| < \varepsilon$  locally.

For a complete derivation of the definition, the reader is referred to the original work [Boc01] or to some later coverage of the topic [Boc18].





## Novel Synchronization Measure

In this chapter, we introduce a measure of synchronization based on information theory. Unlike similar approaches, it is bounded between 0 (no synchronization) and 1 (full synchronization). We will prove that the measure approaches 1 only for synchronous systems.

We build on the idea of [Rul95; Brooo; Boco1], who worked towards a fundamental definition of synchronization in chaotic systems. While [Brooo] first explicitly tried to unify the growing zoo of synchronization types, Boccaletti in [Boco1] showed a framework from which he was able to derive all existing synchronization types. We will define a measure, the synchronized mutual information, which detects the existence of a synchronization function and thus determines whether a system is synchronous. Primarily, the measure is well suited to detect GS. However, the results of [Boco1] allow us to construct some strategies that allow the detection of other types of synchronization.

Our measure is based on Shannon entropy and mutual information. A coarse-grained variant of mutual information was proposed in [Palo1] to assess potential synchronization averaged over sliding time windows, eventually requiring large quantities of data. We are not aware of any previous work that has been able to show a direct relationship between the existence of a synchronization function and mutual information. In order to show that our proposed measure actually identifies the existence of a synchronization function, we need to recall some fundamental properties of information theory.

In [Piko1] the authors distinguish between active and passive experiments. In active experiments, we can freely manipulate all parameters of the system and always observe the explored phase space. In passive experiments, the system is a black box with only a few knobs to tune. We are left with fewer analytical methods and have to rely on the recorded values (which are often only a slice of the phase space). Like other MI-based methods, our proposal is particularly well suited to passive experiments. We are not aware of any MI-based method that has been able to demonstrate a direct correspondence between its values and synchronization in the system.

## 2.1 Introduction to Information Theory

This section serves as a quick reminder of the basic measures of information theory. Its central concept is entropy, a measure of the amount of information contained in a signal.

The foundations of information theory are closely related to the description of entropy in [Sha48] as a measure of the amount of information a noisy transmission can carry. A rigorous introduction to the topic can be found in [Mac03; Yeu02].

A few words about notation: The observed *random* variable is written as  $X$  with its possible observations  $X_i$ . We will also refer to  $X_i$  as the symbol. Each observation is assigned a probability  $p(X = X_i) = p(X_i)$ . Later we will also use the joint probability  $p(X_i, Y_j)$ . We restrict ourselves to discrete probability distributions.

### 2.1.1 Shannon Entropy

Shannon's entropy originated in the study of signal transmission. The transmission would be the random variable  $X$  (since the receiver would not know its content) with  $X_i$  the received symbol. Its central unit is the *bit*, calculated by

$$h(X_i) = -p(X_i) \log_2 p(X_i), \quad (2.1)$$

is the information content of an observation. The unit is given by the base of the logarithm and is called *nat* for the natural logarithm. As the unit plays no further role in our discussion, we will omit the base in any further notation.

Next, we want to estimate the information that we expect from a signal. To do so, we study the slice of a random process with two symbols  $\theta$  and  $1$ :

... 1 1 1 1 0 1 1 1 0 0 1 1 1 0 1 1 1 1 1 1 ...

So how much information does this signal give us? Since we sampled the signal ourselves, we know that  $p(\theta) = 0.2$  and  $p(1) = 0.8$  (which is also correctly reflected in the observed symbols). The information content of the symbols with lower probability is higher, but the other symbol is observed more often. We calculate the expected information per symbol by

$$H(X) = -\langle \log p(X_i) \rangle = -\sum_i p(X_i) \log p(X_i) \quad (2.2)$$

for a symbol in our signal  $X$  [Gro13]. We call this expectation  $H(X)$  the entropy [Sha48].

We wonder whether high- or low-probability events have a greater impact on the overall entropy. The answer is found in Figure 2.1, which shows how each probability affects the information contribution of a single symbol. It shows that both certain events and

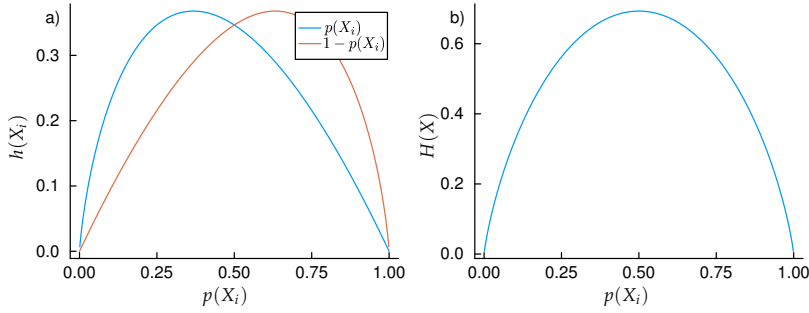


Figure 2.1: In a binary distribution, the contribution of each outcome  $X_i$  to the total entropy peaks at values smaller than 0.5, however, the entropy is at its maximum when both outcomes are equally likely. In a) we see the information  $h$  of a single outcome on the probability of observing that symbol. Although the information gain for a single outcome is at a maximum for symbols observed less than 50 % of the time, b) shows that the entropy of the binary distribution peaks when both outcomes are equally likely.

non-events contain no information. Comparing the information of a single symbol and the entropy of a random process with two possible outcomes, the entropy peaks for equal distribution of information for an equal distribution of information, while the peak for a single event is slightly skewed towards the lower probability events. This concept can be generalized and it can be shown that the entropy for a random variable with  $N$  possible observations attains its maximum value when all probabilities are equal, thus

$$p(x_i) = \frac{1}{N}. \quad (2.3)$$

Finally, a note on the properties of Shannon entropy: Shannon entropy is only well defined for discrete random variables. Extending the measure to the continuous regime is not as simple as replacing the sum by an integral without losing some of the properties of the discrete case. Shannon himself made this mistake and proposed [Sha48, p. 653] a continuous measure by replacing the sum with an integral. This type of entropy is now known as differential or continuous entropy. In particular, it is not guaranteed that the differential entropy is  $\geq 0$  [Cov05, p. 243].

The correct extension to the continuous regime was later shown by [Jay63, p. 201] and is known as the limiting density of discrete points. However, this work restricts itself to Shannon entropy. In practice, we will find that many estimators are derived for differential entropy. Users should be aware that our results do not provide a basis for the use of differential entropy estimators; further discussion of this extension to the estimation of the measure proposed in Section 2.4 can be found in Section 2.6.5.

The total amount of information we have can always only increase our knowledge of the system. The same is true for the entropy and

$$H(X) \geq 0 \quad (2.4)$$

means, we can never unlearn. This becomes clear when we look at Equation (2.2). Due to the logarithm and upper bound of any probability value, all terms in the sum must be negative (and the sign inverts this).

We can deduce the upper limit from Figure 2.1 and see that the upper bound of the entropy must be given for a system with equal proba-

bilities. For a random variable with  $N$  possible observations, we can therefore conclude

$$H(X) \leq -\log \frac{1}{N}. \quad (2.5)$$

### 2.1.2 Mutual Information

So far we have introduced entropy as a measure of the expected information of an independent random variable. In many cases, we can observe correlations between two signals  $X$  and  $Y$ . Information theory provides us with tools to study the content of information and the correlation between these variables. Together, the random variables have a joint probability distribution  $p(X_i, Y_j)$  with its marginals  $p(X_i) = \sum_j p(X_i, Y_j)$  and  $p(Y_j) = \sum_i p(X_i, Y_j)$ . The joint entropy is a direct extension of the entropy for marginal distributions

$$H(X, Y) = - \sum_{X_i, Y_j} p(X_i, Y_j) \log p(X_i, Y_j). \quad (2.6)$$

Its upper and lower bounds are given by the entropy of its marginal  $H(X)$  and  $H(Y)$  via [Mac03]

$$\max[H(Y), H(X)] \leq H(X, Y) \leq H(X) + H(Y). \quad (2.7)$$

Correlations in the marginals of bivariate distributions allow a prediction of one variable whenever the other variable is known. We can measure the information of  $X$  remaining when  $Y$  is known with the conditional entropy

$$H(X|Y) = - \sum_{i,j} p(X_i, Y_j) \log \frac{p(X_i, Y_j)}{p(Y_j)}. \quad (2.8)$$

If  $X$  and  $Y$  are independent of each other,  $p(X_i, Y_j) = p(X_i)p(Y_j)$  (Equation (2.8)) simplifies to

$$H(X|Y) = - \sum_j p(Y_j) \sum_i p(X_i) \log p(X_i) = H(X) \quad (2.9)$$

and as expected, the conditional entropy becomes the entropy for marginal distributions if  $X$  is fully independent of  $Y$ . This can be shown by replacing  $p(X_i, Y_j)$  with  $p(Y_j)$  in Equation (2.9) [Mac03]. These cases give the upper and lower limit of the conditional entropy

$$0 \leq H(X|Y) \leq H(X). \quad (2.10)$$

With joint and conditional entropy, we can measure how much information is contained in the joint distribution or how much information one provides to the other. Another measure is the shared information between  $X$  and  $Y$ . This is calculated using the mutual information (MI)

$$I(X; Y) = \sum_i \sum_j p(X_i, Y_j) \log \frac{p(X_i, Y_j)}{p(X_i)p(Y_j)}. \quad (2.11)$$

The MI can be expressed in terms of joint, conditional, and Shannon entropy. We will use the following expressions later. We find that the MI can be expressed by

$$\begin{aligned} I(X; Y) &= H(X) + H(Y) - H(X, Y) \\ &= H(X) - H(X|Y) \\ &= H(Y) - H(Y|X). \end{aligned} \quad (2.12)$$

These terms allow us to derive an upper and lower bound on the MI by the entropy of its marginal distributions. By Equation (2.10) and Equation (2.7) we can show that

$$0 \leq I(X; Y) \leq \min[H(X), H(Y)] \quad (2.13)$$

which can also be found in [Maco3].

## 2.2 Information Theory and Deterministic Systems

The previous section introduced Shannon entropy  $H(X)$  and mutual information  $I(X, Y)$  as measures of the variability and (generalized) correlation of the random variables  $X$  and  $Y$  to compute both the entropy and the Mutual Information (MI) for a time series. We need to find a reasonable way to estimate a probability distribution within a time series. In other words: we need to find a representation of the time series as a random variable and identify the states of the trajectories with symbols of the random variable.

Since we are mainly operating on recorded time series, we will only deal with those trajectories that are a countable set of vectors or scalars  $x[t]$ . To identify these trajectories with a probability distribution, we define a symbolization function  $S : \mathbb{R} \mapsto \Omega$  (with the sample space  $\Omega$ ), which assigns a symbol to each value in  $x[t]$

$$S(x[t]) = X_i. \quad (2.14)$$

Several points in time can be assigned with the same symbol  $X_i$ . Therefore, we do not identify a symbol by the time  $t$  but with  $i$ .

By assigning a symbol to each point in time, we can calculate a discrete probability distribution. The symbols  $X_i$  are then the outcomes of a random variable (which we also call  $X_i$ ). We then find that if we pick an arbitrary point in time  $t$ ,  $p(X_i)$  will be the probability that the symbol assigned to  $x[t]$  is  $X_i$ .

The symbolization function  $S$  must balance two requirements: First, it must be a “good” representation of the structure of the phase space (The meaning of this is further discussed in Section 2.6.4) and at the same time provide enough samples (within the restrictions of the measurement) for each symbol to allow a proper estimation of its probability.

To derive the symbols of the bivariate probability distribution we assign a unique symbol to each unique pair of symbols from both

trajectories at the same time  $t$ :

$$(X_i, Y_j) = S(\mathbf{x}[t]) \otimes S(\mathbf{y}[t]). \quad (2.15)$$

With this approach, we lose the information about the temporal order. Since the relationship between the two trajectories should be fully encoded in the state of the common phase space, all information is carried over into the joint distribution.

This leaves us with the question of how we can assign symbols to each potentially multi-dimensional vector of the trajectory and calculate the respective probabilities. Here we will mainly discuss an approach that symbolizes the vector for each time point. This restriction is not necessary, and other approaches to symbolization might also work.

For a finite series, we could simply assign a different symbol to each unique vector. For an accurately precise estimation, we need to have several samples per symbol. For coarse-grained symbols, we will lose details of the correlation between the trajectories. Fine-grained approaches will result in undersampled distributions and will lead to a possible overestimation of the correlation.

Probably the most common method is equidistant binning. We divide the phase space into equal-sized bins and assign each point to the bin it falls into. The number of bins  $N_{\text{Bins}}$  and their size and position are chosen according to the data set. Although this method gives good results, especially for low-dimensional data in higher-dimensional phase spaces, the method can yield to undersampling. For equal bins  $n$  in each dimension  $d$ , the total number of bins increases with  $n^d$ .

### 2.3 Mutual Information in the Presence of Synchronization

Following Equation (2.13), we know that the MI  $I(Y; X)$  is bound by the entropy of  $H(X)$  and  $H(Y)$ . In this section, we will show that approaching this upper bound indicates a synchronized system.

In this section, we will show that the MI can indicate the existence of a synchronization function. More specifically, we will show that

$$I(X; Y) = \min[H(X), H(Y)] \iff \exists f : \mathbb{R}^{m_1} \rightarrow \mathbb{R}^{m_2} \forall x \in \mathbb{R}^{m_1}, y \in \mathbb{R}^{m_2} \text{ with } f(x) = y \text{ (} f(y) = x \text{)} \quad (2.16)$$

where  $f$  is the synchronization function. We build our proof on the framework of synchronization proposed in [Boco1] (a short introduction is given in Section 1.2.3).

### 2.3.1 An Existing Function Implies Maximum Mutual Information

This section proves the implication  $\exists f : R^{m_1} \rightarrow R^{m_2} \forall x \in R^{m_1}, \forall y \in R^{m_2}$  with  $f(x) = y$  then  $I(X; Y) = \min[H(X), H(Y)]$  (see Equation (2.16)). We need to show that if there is a synchronization function  $f$ , then the I is equal to its bound given by its marginal entropies.

As we want to avoid a special case where either of the marginal entropies approaches zero, we will restrict ourselves to non-constant trajectories.

A short note on the notation: Sometimes we will write  $f(X_i) = Y_j$  by which we mean that we calculate

$$S(f(x[t])) = Y_j \text{ for } S(x[t]) = X_i. \quad (2.17)$$

**Theorem 1:** If there exists a function  $f(x[t]) = y[t]$  for all  $t$  and two non-constant trajectories  $x[t]$  and  $y[t]$  then  $H(Y) \leq H(X)$ .

*Proof.* If there exists a function  $f(x[t]) = y[t]$  we can rewrite the joint probability function  $p(X_i, Y_j)$  of the trajectories  $x[t]$  and  $y[t]$  as

$$p(X_i, Y_j) = p(X_i, f(X_i)) = p(X_i). \quad (2.18)$$

The same relation allows us to rewrite the marginal probability  $p(Y_j)$  as a sum of  $p(X_i)$

$$p(Y_j) = \sum_{X_i} p(X_i, Y_j) = \sum_{X_i: f(X_i)=Y_j} p(X_i). \quad (2.19)$$

This means we can rewrite the entropy  $H(Y)$  in terms of the random variable  $X$

$$\begin{aligned} H(Y) &= - \sum_{Y_j} p(Y_j) \log p(Y_j) \\ &= - \sum_{Y_j} \sum_{X_i: f(X_i)=Y_j} \left[ p(X_i) \log \left( \sum_{X_k: f(X_k)=Y_j} p(X_k) \right) \right]. \end{aligned} \quad (2.20)$$

We want to estimate the upper bound of  $H(Y)$ . Since the logarithm is strictly monotonically increasing, we can write

$$- \log(p(X_i) + p(X_k)) \leq - \log(p(X_i)) \quad (2.21)$$

and consequently

$$- \log \left( \sum_{X_k: f(X_k)=Y_j} p(X_k) \right) \leq - \log p(X_i). \quad (2.22)$$

Every  $p(X_i)$  in Equation (2.20) is estimated with the previous relation. This gives

$$H(Y) \leq - \sum_{Y_j} \sum_{X_i: f(X_i)=Y_j} p(X_i) \log p(X_i) \quad (2.23)$$

by only using those  $X_k$  in the sum of Equation (2.20) where  $X_k = X_i$ . Due to the synchronization function  $f$  we know that for each  $\mathbf{x}[t]$  there exists exactly one  $\mathbf{y}[t]$ . Values  $X_i$  in the double sum above equation will consequently only be visited in one outer sum. One  $X_i$  can only map to one  $Y_i$ . We then rewrite the equation we have derived with

$$H(Y) \leq - \sum_{X_i} p(X_i) \log p(X_i) = H(X) \quad (2.24)$$

and complete the proof.  $\square$

We now proceed to show that the upper bound for the MI is given by  $H(X)$  if there exists a synchronization function  $f$ .

**Theorem 2:** If there exists a function  $f$  for two non-constant trajectories  $\mathbf{x}[t]$  and  $\mathbf{y}[t]$  such that  $f(\mathbf{x}[t]) = \mathbf{y}[t]$  for all  $t$ , then  $I(X; Y) = \min[H(X), H(Y)]$ .

*Proof.* If there exists a function  $f(\mathbf{x}[t]) = \mathbf{y}[t]$  we can rewrite the joint probability function of the trajectories  $\mathbf{x}[t]$  and  $\mathbf{y}[t]$  as

$$p(X_i, Y_j) = p(X_i, f(X_j)) = p(X_i). \quad (2.25)$$

We use this relation to rewrite the MI

$$I(X; Y) = \sum_{X_i, Y_j} p(X_i, Y_j) \log \frac{p(X_i, Y_j)}{p(X_i)p(Y_j)} \quad (2.26)$$

$$= \sum_{X_i, Y_j} p(X_i, Y_j) \log \frac{p(X_i)}{p(X_i)p(Y_j)} \quad (2.27)$$

$$= - \sum_{X_i, Y_j} p(X_i, Y_j) \log p(Y_j) \quad (2.28)$$

where we preserved the joint distribution outside the logarithm for the next step. Since the remaining distribution in the logarithm is independent of  $X_i$  we insert the joint probability of  $p(Y_j) = \sum_{X_i} p(X_i, Y_j)$

$$- \sum_{Y_j} \left[ \log p(Y_j) \sum_{X_i} p(X_i, Y_j) \right] = - \sum_{Y_j} p(Y_j) \log p(Y_j) \quad (2.29)$$

$$= H(Y) = I(X, Y). \quad (2.30)$$

$\square$

Thus, we have established a direct connection between the existence of the synchronization function  $f$  and the MI. If  $f$  exists, the MI will be equal to the lower of the marginal entropies.

**Theorem 3:** If there exists a function  $f$  for two non-constant trajectories  $\mathbf{x}[t]$  and  $\mathbf{y}[t]$  such that  $f(\mathbf{x}[t]) = \mathbf{y}[t]$  for all  $t$ , then the  $I(X; Y) = \min[H(X), H(Y)]$ .



*Proof.* If there exists a  $f(X) = Y$  then from Theorem 1 we know that  $H(Y)$  will be smaller than  $H(X)$ . Thus

$$\min[H(X), H(Y)] = H(Y) \quad (2.31)$$

Theorem 2 allows us to replace  $I(X; Y)$  by  $H(Y)$ . We can then write

$$I(X; Y) = H(Y) = \min[H(X), H(Y)] = H(Y) \quad (2.32)$$

which is true.  $\square$

### 2.3.2 Mutual Information and the Existence of a Function

In this part, we will prove the other implication in the equivalence of Equation (2.16). We will show that if the MI is equal to the bound given by the lower of its two marginal entropies, there exists a function  $f$  that maps a point in  $X$  to  $Y$ .

**Theorem 4:** If the  $I(X; Y) = \min[H(X), H(Y)]$  there exists a function  $f$  such that  $f(x[t]) = y[t]$  and/or  $f(y[t]) = x[t]$ .

*Proof.* With Equation (2.12) we write the  $I$  as

$$I(X; Y) = H(Y) - H(Y|X) \quad (2.33)$$

where we assume w.l.o.g. that  $H(Y) \leq H(X)$ . For the right term to be equal to  $I(X, Y)$ , the conditional entropy  $H(Y|X)$  has to be zero (without the entropy also being zero). The conditional entropy can be written as

$$H(Y|X) = - \sum_{i,j} p(X_i, Y_j) \log \frac{p(X_i, Y_j)}{p(X_j)} \quad (2.34)$$

where the single terms only evaluate to zero where either  $p(X_i, X_j) = 0$  or  $p(X_i) = p(X_i, Y_j)$ . This is only the case if  $y[t]$  is perfectly predicted by  $x[t]$ , essential if there exists a function  $f(x[t]) = y[t]$ .  $\square$

**Theorem 5:** If there exists *no* synchronization function  $f$  such that there are two trajectories  $x[t]$  and  $y[t]$  such that  $f(x[t]) = y[t]$  (or vice versa) for all  $t$ , then the  $I(X; Y) < H(Y)$  (or  $< H(X)$ ) strictly.

*Proof.* This lemma can be shown by contradiction to Theorem 4. If the  $I(X; Y) = H(Y)$  then, due to Theorem 4, there exists a synchronization function.  $\square$

We know now that for non-constant trajectories  $x[t]$  and  $y[t]$  if the  $I(X; Y) = \min[H(X), H(Y)]$  there exists a synchronization function  $f$ . Furthermore, if no such function exists, then it must be that the  $I(X; Y) < \min[H(X), H(Y)]$ .

## 2.4 Synchronous Mutual Information

So far we have shown that the MI is sensitive to the presence of synchronization. In this section, we will use the previous findings to propose the Synchronized Mutual Information (SMI). The SMI is a measure of synchronization based on information theory. While MI has been used in previous methods to find synchronization, we have proved a link between the existence of a synchronization function and MI.

Later in this section, we will also consider the special case of vanishing marginals. The SMI diverges when one of the entropies of the MI's marginals approaches zero. We have studied all cases of vanishing marginals in Section 2.4.2.

### 2.4.1 Definition

For now, we define a mutual information theory-based measure.

**Definition 1:** Let there be two trajectories  $x[t]$  and  $y[t]$  and with their assigned random variables  $X$  and  $Y$ . We then call

$$\text{SMI}(X;Y) = \begin{cases} \frac{I(X;Y)}{\min[H(X),H(Y)]} & \text{if } H(X) \neq 0 \neq H(Y) \\ 1 & \text{if } H(X) = 0 = H(Y) \\ 0 & \text{if } H(X) = 0 \text{ or } H(Y) = 0 \end{cases} \quad (2.35)$$

the synchronous mutual information (SMI).

We can immediately see that the SMI must be bounded between 0 and 1. Since neither the entropy nor the MI can be negative Equation (2.4), the MI must be less than the entropy of one of its arguments (see Equation (2.13)). Furthermore, in the following paragraphs, we will show that this measure is indeed a good measure for synchronization. We achieve this by first showing that the normalization for the SMI corresponds to the definition of synchronization as given by [Boc01] and in [Rul95].

### 2.4.2 Limit of a Vanishing Mutual Information

As a simple normalization of the MI

$$\frac{I(X;Y)}{\min[H(X),H(Y)]} \quad (2.36)$$

is not well defined if the entropy of one or both of  $x[t]$  and  $y[t]$  approach zero, we have defined special values for these cases. Here, we give a short justification for each of these choices and show that they do not contradict the central case.

In order to find reasonable values for each of the cases, we explore the limit of trajectories approaching a constant value. We describe these using a general contingency table

$X_{\epsilon}, Y_{\epsilon}$	$Y_{1,\epsilon}$	$Y_{2,\epsilon}$	
$X_{1,\epsilon}$	$1 - k - \alpha\epsilon$	$g\epsilon$	$1 - k + (g - \alpha)\epsilon$
$X_{2,\epsilon}$	$k + (\alpha - 1)\epsilon$	$(1 - g)\epsilon$	$k + (\alpha - g)\epsilon$
	$1 - \epsilon$	$\epsilon$	$1$

To keep the probabilities well defined, we apply some restrictions on the parameter so that  $\alpha \geq 1$ ,  $0 \leq g, k < 1$ . We see that with this contingency table, the limit entropy for  $\tilde{y}$  is

$$\lim_{\epsilon \rightarrow 0} H(Y_{\epsilon}) = \lim_{\epsilon} [-(1 - \epsilon) \log(1 - \epsilon) - \epsilon \log \epsilon] = 0 \quad (2.37)$$

where the limit for  $H(X_{\epsilon})$  is not zero for  $k \neq 0$ . This allows us to control the different cases with  $k$  and check how the results depend on the “speed” with which the joint probabilities approach zero.

First, we will look at the case where  $k > 0$ . We can write the MI

$$\begin{aligned} I(X_{\epsilon}, Y_{\epsilon}) = & -(g - 1) \epsilon \log \left( -\frac{g - 1}{(\alpha - g) \epsilon + k} \right) + g \epsilon \log \left( -\frac{g}{(\alpha - g) \epsilon + k - 1} \right) \\ & + ((\alpha - 1) \epsilon + k) \log \left( -\frac{(\alpha - 1) \epsilon + k}{(\alpha - g) \epsilon^2 - (\alpha - g) \epsilon + (\epsilon - 1) k} \right) \\ & - (\alpha \epsilon + k - 1) \log \left( -\frac{\alpha \epsilon + k - 1}{(\alpha - g) \epsilon^2 - (\alpha - g + 1) \epsilon + (\epsilon - 1) k + 1} \right) \end{aligned} \quad (2.38)$$

and see that indeed, the limits are

$$\lim_{\epsilon \rightarrow 0} I(X_{\epsilon}, Y_{\epsilon}) = 0 \quad (2.39)$$

and

$$\lim_{\epsilon \rightarrow 0} \frac{I(X_{\epsilon}, Y_{\epsilon})}{H(Y_{\epsilon})} \rightarrow \frac{0}{0} \quad (2.40)$$

To find a non-diverging limit, we apply the rule of l’Hopital and find the derivative

$$\begin{aligned} I'(X_{\epsilon}, Y_{\epsilon}) = & (\alpha - 1) \log \left( -\frac{(\alpha - 1) \epsilon + k}{(\alpha - g) \epsilon^2 - (\alpha - g) \epsilon + (\epsilon - 1) k} \right) \\ & - \alpha \log \left( -\frac{\alpha \epsilon + k - 1}{(\alpha - g) \epsilon^2 - (\alpha - g + 1) \epsilon + (\epsilon - 1) k + 1} \right) \\ & - (g - 1) \log \left( -\frac{g - 1}{(\alpha - g) \epsilon + k} \right) \\ & + g \log \left( -\frac{g}{(\alpha - g) \epsilon + k - 1} \right) \end{aligned} \quad (2.41)$$

and

$$H'(Y) = \log(1 - \epsilon) - \log \epsilon. \quad (2.42)$$

By removing terms that do not contribute to the limit of  $\epsilon \rightarrow 0$ , we

derive with

$$\begin{aligned} \lim_{\epsilon \rightarrow 0} I'(X_\epsilon, Y_\epsilon) &= \lim_{\epsilon \rightarrow 0} \left[ - (g - 1) \log \left( \frac{1 - g}{k} \right) \right. \\ &\quad \left. + g \log \left( \frac{g}{1 - k} \right) \right. \\ &\quad \left. + 2\alpha - 2 \right] [-\log \epsilon]^{-1} = 0 \end{aligned} \quad (2.43)$$

which is dominated by the log approaching infinity. A second glance at the terms shows us that the result is independent of  $\alpha$  and  $g$ . Only where  $k = 0$  do we have to look at the system again. The same analysis can be applied for  $k = 0$  and, again with l'Hopital, we find that

$$\lim_{\epsilon \rightarrow 0} \frac{I(X_\epsilon, Y_\epsilon)}{H(Y_\epsilon)} \Big|_{k=0} = \lim_{\epsilon \rightarrow 0} \frac{I'(X_\epsilon, Y_\epsilon)}{H'(Y_\epsilon)} \Big|_{k=0} = 1 - g. \quad (2.44)$$

We should consider here that in the case where both  $H(X_\epsilon)$  and  $H(Y_\epsilon)$  vanish,  $H(Y_\epsilon)$  is not necessarily smaller than  $H(X_\epsilon)$ . However, since we cannot determine  $g$  for a constant trajectory, we cannot find a unique limit for the SMI where  $H(Y_\epsilon) = H(X_\epsilon) = 0$ .

While we can show that in the case of strictly one entropy being zero is a good continuation in Equation (2.35), for the case of both entropies evaluating to zero, we can only show that our definition does not contradict the limit of vanishing entropies (see Equation (2.43)). It is chosen such that the results of the SMI replicate those of the identical synchronization.

## 2.5 Types of Synchronization

In previous parts, we have shown that the MI can indicate the presence of a synchronization function. According to the work of [Boco01], synchronization is defined by the presence of such a function. In Boccaletti's work, the synchronization function does not necessarily have to exist between the trajectories in their phase space. If we can find a diffeomorphism  $\mathcal{F}$  in another phase space with a function between the trajectories in the new phase space, we can also speak of synchronization.

In the simplest case, the diffeomorphism is the identity operator and projects the phase space of the trajectories onto itself. If we find a synchronization here, the system is in GS. Furthermore, a synchronization function  $f = 1$  means that the system is in IS.

When we use an unaltered phase space and calculate the SMI there, we test the system for GS.

While in its general form, the I is restricted to detect only GS, for certain classes of synchronization, reasonable candidates for the diffeomorphism  $\mathcal{F}$  can be easily tested. The transformation into the  $W$ -space allows us to identify any relations there. Below are two examples of such transformations.

For lagged synchronization, we expected two systems to follow an identical trajectory but shifted by a fixed amount in time. We can set  $\mathbf{u}(t) = \mathbf{x}(t)$  and  $\mathbf{v}(t) = \mathbf{y}(t - \tau)$  and again end up with a system where we can predict the existence of a synchronous function. In a practical application, we would need to test some candidates  $\tau$  to see if we could identify synchronous behavior in any of them. Although delayed synchronization implies identical but shifted trajectories  $|\mathbf{x}(t) - \mathbf{y}(t - \tau)| = 0$ , with our method we can also identify structures where there is a  $K$  such that  $|\mathbf{K}(\mathbf{x}(t)) - \mathbf{y}(t)| = 0$ , essentially a time-delayed GS.

Finally, phase synchronization (PS) can also be detected. An entropy-based method is proposed in [Tas98], detecting phase synchronization between two trajectories by extracting the phase with a Hilbert transformation

$$g(\mathbf{y}) = \frac{1}{\pi} \int_{-\infty}^{\infty} \frac{x(t)}{y-t} dt. \quad (2.45)$$

To find phase information, other methods can be used, too. According to [Boc01] any proper phase function  $\Psi : \mathbf{x}(t) \rightarrow [0, 2\pi[$  can be used to construct  $\mathcal{F}$  with its components  $\Psi(\mathbf{x}(t))$ ,  $\Psi(\mathbf{y}(t))$ . While systems that fulfill

$$|\Psi(\mathbf{x}(t)) - \Psi(\mathbf{y}(t))| < R \quad (2.46)$$

are understood to be phase synchronous, [Ros96] we again are able to find richer patterns. In [Kra04a] a further discussion of the extraction of phases in chaotic systems can be found.

## 2.6 Estimating Mutual Information and Entropy

To compute the entropy of a given trajectory  $x[t]$ , we need to assign a probability distribution to this function. In the previous chapter, we discussed one possible approach to find the probability of getting a particular value by choosing any value in the trajectory. In most cases, we will not even be able to get an analytical form of the trajectories. To be able to assign a probability distribution to the trajectory, we have to estimate the property from the sampled set.

### 2.6.1 Entropy

Naturally, the quality of our estimate will depend on the available data and the resolution and distribution of our symbolization. However, the estimation method itself also has a big impact on the quality of the results. The most obvious method is to count all occurrences of values in  $X$  and assign the relative frequency of each value as the probability in  $p(X_i)$ . Similarly, we compute the joint distribution of  $p(X_i, Y_j)$  by counting the frequencies of all tuples  $(X_i, Y_j)$ . We plug these probabilities into Equation (2.11) and obtain

$$\langle H(X) \rangle_{\text{naive}} = \sum_{X_i} \frac{N(X_i)}{N} \log \frac{N(X_i)}{N}, \quad (2.47)$$

the naive estimator where  $N = \sum_i N(X_i)$ . While it will also converge to the true entropy in the limit of infinite samples, it has been shown to underestimate the entropy for any finite number of samples [Gra88; Krao4b].

The Bayesian estimator of the entropy of a random variable  $X$  can be written as

$$\langle H(\Theta)|X \rangle = \int_{\Theta} d\Theta p(\Theta|X) H(\Theta) \quad (2.48)$$

where  $\Theta$  are the parameters of a probability distribution and  $p(\Theta|X) = \frac{p(X|\Theta)p(\Theta)}{p(X)}$  is the probability of those parameters given the observed random values  $X$ .  $H(\Theta)$  is the entropy of the distribution. Shannon entropy is defined by

$$H(\Theta) = \sum_i p_i(\Theta) \log p_i(\Theta) = \sum_i h_i(\Theta) \quad (2.49)$$

which allows us to write Equation (2.48) as

$$\begin{aligned} \langle H(\Theta)|X \rangle &= \int_{\Theta} d\Theta p(\Theta|X) \sum_i h_i(\Theta) \\ &= \sum_i \int_{\Theta} d\Theta p(\Theta|X) h_i(\Theta). \end{aligned} \quad (2.50)$$

The naive estimator is based on the Poisson distribution, which we characterize with a parameter  $\lambda_i$  for each symbol  $X_i$ . This assumption implies that the probability of observing each  $X_i$  is independent of observing all other symbols. We insert  $\Theta = (... \lambda_i ...)$  into the above equation and since  $\int_{\lambda_j} d\lambda_j p(\lambda_j|X) h(\lambda_j) = 1 h(\lambda_j)$  we can write

$$\langle H(\Theta)|X \rangle \approx \sum_i \dots \int_{\lambda_j} d\lambda_j p(\lambda_j|X) h(\lambda_j) \dots \quad (2.51)$$

$$= \sum_i \int_{\lambda_i} d\lambda_i p(\lambda_i|X) h(\lambda_i). \quad (2.52)$$

In a final assumption, we expect the estimation of an entropy term to be equal to the estimator of the probability of the symbol, e.g.  $\langle h(\lambda)|X \rangle = h(\langle \lambda|X \rangle)$  and we obtain

$$\langle H(\Theta)|X \rangle \approx \sum_i \left( \int_{\lambda_i} d\lambda_i p(\lambda_i|X) \lambda_i \right) \quad (2.53)$$

where  $\int_{\lambda} d\lambda p(\lambda|X) \lambda$  is just the estimator for  $\lambda$  for which we know

$$\int_{\lambda} d\lambda p(\lambda|X) \lambda = \hat{\lambda} = \frac{N(X_i)}{N}. \quad (2.54)$$

Putting everything together, we derive the aforementioned naive estimator in Equation (2.47).

Let us see if we can do better. By removing the assumption that  $\langle h(\lambda)|X \rangle = h(\langle \lambda|X \rangle)$  it was previously shown by Grassberger that the bias is, while not completely removed, reduced [Gra88]. The author found that we can write Equation (2.52) as

$$\langle H(\Theta)|X \rangle \approx \hat{H}_G(X) = \log N - \frac{1}{N} \sum_i N(X_i) G_{N(X_i)}, \quad (2.55)$$

where

$$G_n = \Psi(n) + (-1)^n \int_0^1 dx \frac{x^{n-1}}{x+1} \quad (2.56)$$

with the digamma function  $\Psi(n)$ . The full derivation of the Grassberger entropy is found in [Gra88] with a revised version published later in [Grao8].

Furthermore, we can remove the assumption that the probabilities of the symbols being independent of each other (which allowed us to write Equation (2.52)). This can be done using a Dirichlet distribution. One such example is the NSB estimator from [Nemo4]. There are also estimators for continuous systems where the sum in the entropy is replaced by an integral. These continuous entropies do not guarantee some of the properties of the Shannon entropy that we will need later. Although the NSB estimator can be used, we used the Grassberger estimator during the work on this thesis because it is easier to use.

### 2.6.2 Mutual Information

The MI between two trajectories  $x[t]$  and  $y[t]$  is estimated by

$$\langle I(\Theta) | X, Y \rangle = \int_{\Theta} d\Theta p(\Theta | X, Y) I(\Theta) \quad (2.57)$$

where  $\Theta$  are the parameters for the joint distribution. Due to Equation (2.12) the above equation can be rewritten to

$$\langle I(\Theta) | X, Y \rangle = \int_{\Theta} d\Theta p(\Theta | X, Y) (H_X(\Theta) + H_Y(\Theta) - H(\Theta)) \quad (2.58)$$

where  $H_X(\Theta)$  is the entropy over the marginal  $X$  marginal and  $H(\Theta)$  the joint entropy. We can resolve the sum in the last term and derive with an estimator

$$\langle I(\Theta) | X, Y \rangle = \langle H_X(\Theta) | X, Y \rangle + \langle H_Y(\Theta) | X, Y \rangle - \langle H(\Theta) | X, Y \rangle. \quad (2.59)$$

We insert the Grassberger estimator from Equation (2.55) and get

$$I_G(X, Y) = H_G(X) + H_G(Y) - H_G(X, Y). \quad (2.60)$$

This approach, while naive, serves its purpose. It should be noted that while the MI has its lower bound at zero, this estimator can have negative values, especially in cases where there is little or no correlation between  $X$  and  $Y$ .

### 2.6.3 Reference Implementation

In the previous section, we introduced the SMI as a classifier for synchronization between two trajectories. So far we assumed that a probability distribution is available. In practice, the distribution will not be readily available and we have to derive it from the samples ourselves. In Section 2.6.1 and Section 2.6.2 we discussed various methods to estimate entropy and MI for a given set of samples.

We motivated the Grassberger estimator  $H_G(X)$  which we will use within this thesis.

We want to estimate the SMI from Section 2.6.2 and first have to check if all or one entropy is zero. Where only one entropy is zero, we will also return 0 as the result, when both are zero, we will return 1. W.l.o.g we assume that  $0 < H(Y) < H(X)$  and the SMI can be calculated by

$$\begin{aligned} \langle \text{SMI}(X; Y) \rangle &= \left\langle \frac{I(X; Y)}{H(Y)} \right\rangle \\ &= \int_{\Theta} d\Theta p(\Theta | X, Y) \left( 1 + \frac{H_X(\Theta)}{H_Y(\Theta)} - \frac{H(\Theta)}{H_Y(\Theta)} \right) \end{aligned} \quad (2.61)$$

for which we assume that the parameters of  $\Theta$  for each variable  $X$  and  $Y$  do not mix. With a second assumption, that  $\left\langle \frac{1}{h(\Theta)} \right\rangle = \frac{1}{\langle h(\Theta) \rangle}$  we derive with

$$\begin{aligned} \langle \text{SMI}(\Theta) | X, Y \rangle &= 1 + \frac{\langle H_X(\Theta) \rangle}{\langle H_Y(\Theta) \rangle} - \frac{\langle H(\Theta) \rangle}{\langle H_Y(\Theta) \rangle} \\ &= 1 + \frac{H_G(X)}{H_G(Y)} - \frac{H_G(X, Y)}{H_G(Y)}. \end{aligned} \quad (2.62)$$

The results of the last equation are then used to calculate those branches of the SMI where the entropies of both values are greater than zero. In Section 2.6.2 we gave the algorithm that calculates  $H_G$ . The algorithm was first introduced in [Gra88]. For the implementation, we use an approximation of the Grassberger function  $G(n)$  given in [Sta16] for the count of events  $n \geq 50$ . In this implementation, we write Grassberger's estimator from Equation (2.55) as

$$\hat{H}_G(X) = G(N) - \frac{1}{N} \sum_i N(X_i) G_{N(X_i)}. \quad (2.63)$$

The algorithm to calculate  $\hat{H}_G(X)$  is given in Algorithm 2.1.

#### 2.6.4 On Good Binning

We have established the Grassberger estimator to calculate the SMI. Throughout this work, we use a linear binning approach. Although it works well for the chosen systems, especially in higher dimensions, individual bins quickly become undersampled. To better understand the limitations of the linear binning approach (Figure 2.2), we will examine a sample set.

We create two fully correlated trajectories that share a phase space  $x, y$  with

$$\begin{aligned} x(t) &= t \\ y(t) &= \frac{t}{2} + \sin(t). \end{aligned} \quad (2.64)$$

Figure 2.2 shows the resulting phase space with two binning approaches. In Figure 2.2 a) we see how with a generous amount of



Listing 2.1: Implementation for the Grassberger entropy estimator . The user provides the frequencies of all observed symbols. The algorithm is described in Equation (2.63).

```

using SpecialFunctions # SpecialFunctions.jl package required

function grassberger_function(ni)
    n = ni - (ni % 2)
    if n == 0
        return 0
    end
    if n >= 50
        a = 1. / (24*n^2)
        b = 7. / (960*n^4)
        c = 31. / (8064*n^6)
        return log(2*n) + a - b + c
    end

    return -log(2) + 2 * digamma(2 * n) - digamma(n)
end

# frequencies: List of Integers
function grassberger_entropy(frequencies)
    gb_weighted_events = 0
    for f in frequencies
        gb_weighted_events += f*grassberger_function(f)
    end
    events = sum(frequencies)
    entropy = grassberger_function(events) -
        (1. / events) * gb_weighted_events
    return entropy
end

```

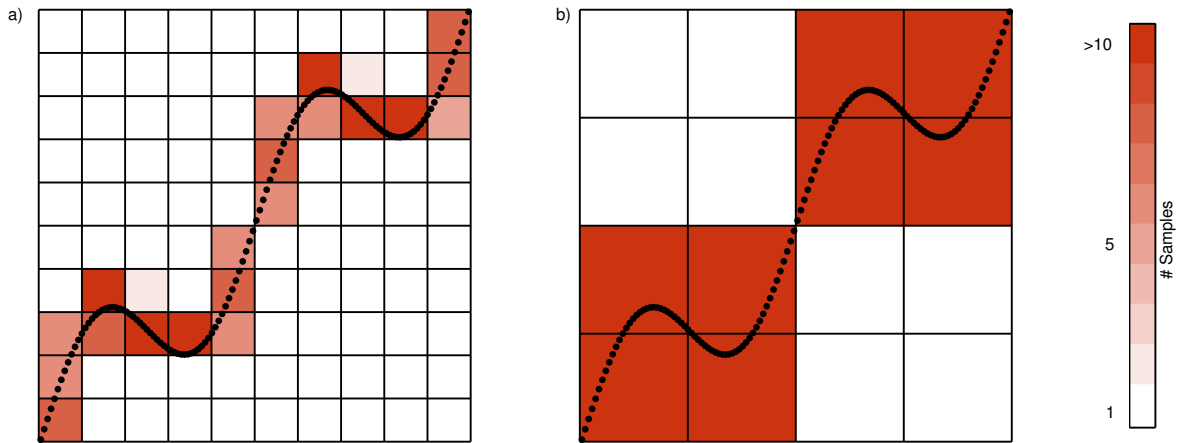


Figure 2.2: A good binning strategy is necessary to preserve the structure of the sampled function while not undersampling individual bins. The symbols for a sinus curve superimposed with a line are derived with an equally spaced binning strategy (see Equation (2.64)). We see that for strategy a), while the form of the function is better preserved by the bins, individual bins are undersampled. The second binning strategy b) has larger bins and thus more samples per bin; however, it does not preserve the structural features of the function as well. For better results, adaptive binning strategies can be applied, but are neither shown here nor applied within this work.

bins, many are unused (which is not a problem), and some undersampled. In contrast, in Figure 2.2 b) the bins are well populated, however, the structure of the phase space is lost.

In Figure 2.3 we study the measured SMI for a random distribution and the system defined in Equation (2.64). The SMI is calculated for each random and regular system with  $n$  samples and either 10 or 100 different numbers of bins. For the regular system, we expect the SMI to be evaluated to 1. The random system should not show any correlation and we expect the SMI to vanish. We see that the variation of the SMI quickly stabilizes where the number of samples exceeds the number of different symbols. With an undersampled set, we were unable to reliably distinguish between spurious and real correlations.

Interestingly, we can see some “oscillation” for higher numbers of sampling points. The curve sampling is performed with equal intervals between the points. We assume that the oscillation reflects aliasing effects from the finite resolution of the binning process and that certain distances between the points are better suited for each chosen binning approach.

### 2.6.5 Alternative Estimators

As we have seen in the previous section, linear binning algorithms can show problems with a representative sampling of the phase space. The good news is that the SMI can be used with other estimators. While linear binning is sufficient for many use cases, it is especially limited in higher dimension and phase spaces with a complex structure.

The obvious solution seems to be to avoid a naive dissection of the phase space into equally sized volumes. By adapting the size of the bins to approach equal sampling, information losses should be

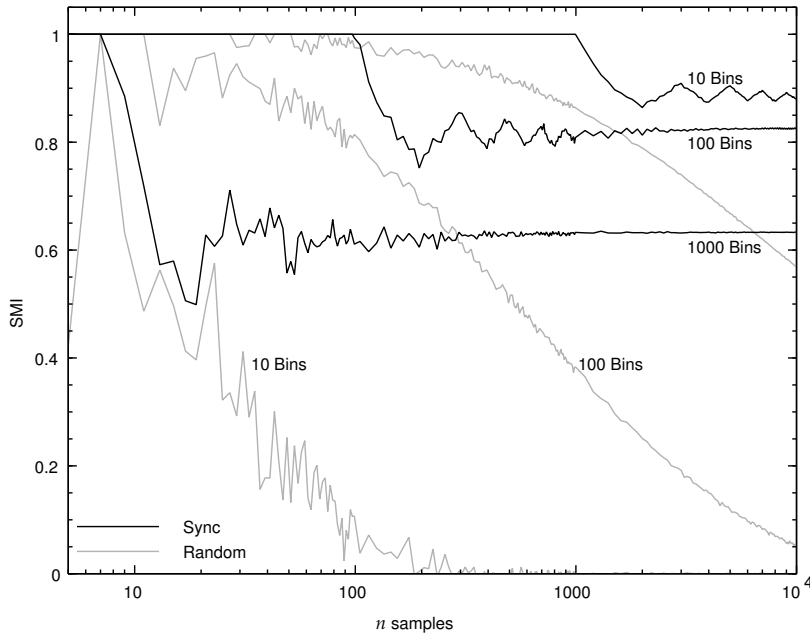


Figure 2.3: Uncorrelated systems can only be distinguished from synchronized systems if enough samples are available. The function shown in Figure 2.2 (and generated from Equation (2.64)) is sampled with  $n$  points and then the SMI is calculated with either 10, 100, or 1000 bins in each dimension. The SMI we expect for a correlated system, such as Equation (2.64), is one. However, the results obtained with finite sampling and finite bin size show that this value is not reached. Nevertheless, when the correlated data points are compared with uncorrelated points from a two-dimensional random distribution, it shows that with enough samples the correlated system can be distinguished from the uncorrelated, the contrast depending on the number of bins and the number of samples.

minimized.

This is exactly what happens in adaptive sampling approaches. There are methods for adaptive binning, for example [Wor15; Sano1]. Other methods use different approaches to estimate the histogram. In [Gen14] the histogram is replaced by a Bayesian approach with a constant-value probability density function and a Dirichlet prior. For estimators of discrete sets of data, we finally find the NSB estimator proposed in [Nemo4]. It lifts the assumption that the frequencies of single symbols can be calculated independently and is thus able to compensate for some bias. For datasets with an unknown or (countably) infinite number of symbols, the estimator in [Arc14] is a good option, although for synchronous systems the assumption of infinite support is not compatible with the dissipative nature of these systems.

An entirely different approach to estimation can be taken for differential entropy. The KSG estimator [Krao4b] calculates the density of points in an area around each point. The density is then used as a proxy for the probability of a point. While the original method estimates the entropy, in [Krao4b] the method is extended to mutual information by choosing a similar approach to that in Equation (2.55). The paper proposes two methods. In later work, one of these methods received an additional bias correction [Gao16].

The Kraskov entropy estimates a proxy density for each point by calculating the next  $N$  neighbors. This allows for better adaptation to the dynamics of the systems than using a static binning method. As mentioned above, this method is based on differential entropy. Differential entropy replaces the discrete/categorical distribution of the Shannon entropy with a continuous probability distribution. Shan-

non himself proposed to simply replace the sum with an integral and derived with

$$H_D(\bar{X}) = - \int_{\mathbb{R}^n} dx p(x) \log p(x) \quad (2.65)$$

for a continuous random variable  $\bar{X}$  in Euclidean space. It was shown in [Jay63] that the correct extension of Shannon entropy to continuous probability distributions is given by

$$H_L(\bar{X}) = - \int_{\mathbb{R}^n} dx p(x) \log \frac{p(x)}{m(x)}. \quad (2.66)$$

Otherwise similar to differential entropy, it normalizes  $p(x)$  with  $m(X)$ . It gives the densities of the sampling. While the differential entropy depends on the particular choice of dimension, this effect is canceled by the limited entropy of discrete points. This is an approach to the problem that is not very widespread and thus will not be treated in this work. Since differential entropy does not guarantee any of the properties used to show the effectiveness of the SML, it does not provide a suitable alternative.

# Chaos & Synchronization

In this chapter, we will apply the Synchronized Mutual Information derived in the previous chapter (see Equation (2.35)) to some typical toy systems.

As a test system for continuous systems, we will use a driver/response system by coupling a Rössler to a Lorenz system. To test the performance on mutually coupled systems, we apply the SMI to a linear chain of logistic maps, exploring different coupling parameters, including a single-step delay coupling.

## 3.1 Driver/Response System

The first model to which we will apply the SMI is a driver/response. Each system will have different dynamics. We follow the type of system introduced in Equation (1.8).

As a benchmark, we use a coupled Lorenz-Rössler system. A short overview of each system is given in Section 1.1.3 and Section 1.1.4.

The equations of motion for the coupled system are given as

$$\begin{aligned}\frac{d}{dt}x_1 &= -x_2 - x_3 \\ \frac{d}{dt}x_2 &= x_1 + ax_2 \\ \frac{d}{dt}x_3 &= p + x_3(x_1 - \mu)\end{aligned}\tag{3.1}$$

$$\begin{aligned}\frac{d}{dt}y_1 &= \sigma(y_2 - y_1) - \kappa(x_1 - y_1) \\ \frac{d}{dt}y_2 &= y_1(r - y_3) - y_2 \\ \frac{d}{dt}y_3 &= y_1y_2 - by_3\end{aligned}\tag{3.2}$$

where the driver  $\mathbf{x}$  is a Rössler attractor and the response  $\mathbf{y}$  is a Lorenz system. The diffusive coupling function  $c$  from Equation (1.8) is here given as

$$c(\mathbf{x} - \mathbf{y}) = \kappa(x_1 - y_1),\tag{3.3}$$

where  $\kappa$  is a scalar coupling the Lorenz with the Rössler system.

The system was introduced in [Aba96] as an example system to show the performance of the auxiliary system method.

### 3.1.1 Methods

For the auxiliary system method, we introduce a second response system. It has the same parameters as the reference system

$$\begin{aligned}\frac{d}{dt}y'_1 &= \sigma(y'_2 - y'_1) - \kappa(x_1 - y'_1) \\ \frac{d}{dt}y'_2 &= y'_1(r - y'_3) - y'_2 \\ \frac{d}{dt}y'_3 &= y'_1y'_2 - by'_3\end{aligned}\tag{3.4}$$

however, its initial parameters are slightly perturbed between different simulations.

In their paper [Aba96], the authors proved that if the reference system  $\mathbf{y}$  and the auxiliary system  $\mathbf{y}'$  converge, then  $\mathbf{y}$  and  $x$  are synchronous. They used this method to show that their coupled system experiences GS

To track the distance between the auxiliary and reference systems, we allow the trajectories to settle on their attractors and then calculate the average Euclidean distance  $d$

$$d = \sqrt{\frac{1}{3N} \sum |\mathbf{y}(t) - \mathbf{y}'(t)|^2}\tag{3.5}$$

for the times  $t$ .

A disadvantage of the method is its sensitivity to initial parameters. Although convergence between the auxiliary and reference systems implies synchronization, its absence is not a sign of decoherence. Depending on the displacement, the auxiliary system may end up in an attractor different from the reference system. In these cases, the reference and auxiliary systems will diverge, even when the driver and the driven system are synchronized. This drawback was already noted in the original paper [Aba96].

The simulations were carried out using *julia* with the differential equation package [Bez17; Rac17]. We used a Runge-Kutta solver with a fixed step size of 0.0002 s, more specifically the provided Tsit5 solver [Tsi09]. Parameters and initial conditions are taken from [Aba96] and are given in Table 3.1.

We allow an equilibration time of 50 s. For another 150 s, the system was recorded for its analysis.

We calculate the SMI by two different methods. To use the SMI as defined in Equation (2.35), we have to use the full phase space. This is our first approach, and we call it SMI<sup>3</sup>. We want to see if the SMI can also yield helpful results if the full phase space is not available. To test this, we restrict the SMI to use only data from  $x_1$  and  $y_1$  and call this approach SMI<sup>1</sup>.

Parameter	Value	Variable	Value
$a, p$	0.2	$x_1, x_2$	1
$b$	$8/3$	$x_3$	0
$r$	28	$y_1$	1
$\sigma$	10	$y_2$	5
$\mu$	5.7	$y_3$	10
$\kappa$	0 – 20	$y'_1$	$1 \pm 0.5 \cdot 10^{-3}$
		$y'_2$	$5 \pm 0.5 \cdot 10^{-3}$
		$y'_3$	$10 \pm 0.5 \cdot 10^{-3}$

Table 3.1: Parameters for the Lorenz driven Rössler system, see Equation (3.1), Equation (3.2) and Equation (3.4).

Strictly speaking, the equivalence between the existence of a function connecting  $x$  and  $y$  and the SMI<sup>1</sup> attaining the maximum value of one is not guaranteed anymore. However, in many practical applications, we cannot access the full phase space and have to derive our conclusions with the available data. Evaluating the system, we compare the performance of the reduced phase space SMI<sup>1</sup> with the full phase space SMI<sup>3</sup>.

### 3.1.2 Results

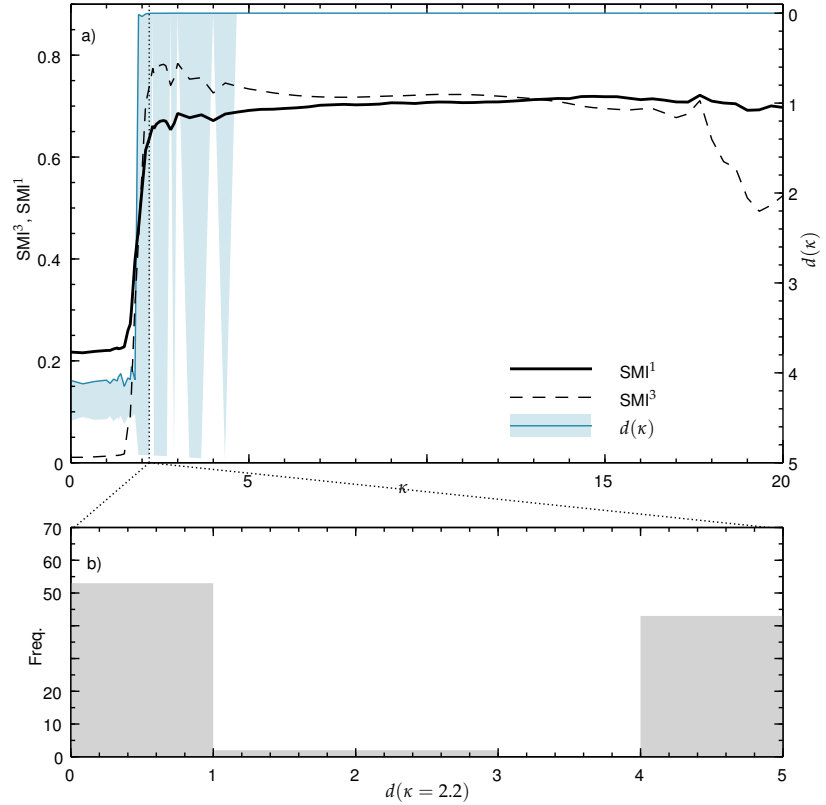
For each coupling strength  $\kappa$ , we calculated the distance  $d$  between the auxiliary and reference systems (see Equation (3.5)) and the SMI. To calculate the SMI, each point in time has to be converted into a symbol representing an individual bin. Bin boundaries were determined by dividing the phase space into equal bins so that each dimension has 10 equally sized bands between the minimum and maximum values.

With the resulting label frequency, we calculate the SMI following the algorithm provided in Section 2.6.3. The results obtained for the coupling values  $\kappa$  between 0 and 20 are shown in Figure 3.1. As mentioned earlier, the auxiliary system method can show non-converging auxiliary and reference systems even in cases where the driver and response system are synchronized. To mitigate this problem, we calculated  $d$  for 100 different initial parameters for each  $\kappa$ , uniformly distributed within the bounds given in Table 3.1. In Figure 3.1 a) we show the minimum and maximum values of  $d$  as a blue ribbon. The minimum values are highlighted by the darker blue line. Since the existence of a converged auxiliary/reference pair indicates synchronization, this line can also be used as a positive proof of synchronization.

For the minimum values of  $d$  we see a clear separation between the incoherent regime  $\kappa \leq 2.2$  and the synchronous regime for  $\kappa > 2.2$ . This separation is also obtained by the SMI.

For the auxiliary system method, the results would have been ambiguous if we had not repeated the simulation with different initial parameters. In Figure 3.1 b) we show the distribution  $d$  for the same  $\kappa = 2.2$  with different initial parameters. Here, we can clearly see

Figure 3.1: When distinguishing between the synchronized and the unsynchronized regime, the results of the SMI match that of the auxiliary system method. Since the SMI does not use an auxiliary system, its results do not depend on the right choice of displacement. The results of both methods for coupling  $\kappa$  between 0 and 20 are presented in a). Two approaches were used to compute the MI: For  $\text{SMI}^3$  the full phase space of the driver/response system was used,  $\text{SMI}^1$  relies on the use of  $x_1$  and  $y_1$ . For the auxiliary system method,  $d$  was calculated with several different displacements of the auxiliary system from the response system. The minimum and maximum average differences  $d$  for each  $\kappa$  are shown as a blue ribbon. Minimum values are highlighted with the darker blue value, since the vanishing  $d$  for a given  $\kappa$  shows synchronization. We can be sure that the systems were synchronized, however, with the auxiliary system method several attempts might have been necessary. In b) we show a cut through the ribbon for  $\kappa = 2.2$ . It shows that the distance between reference and auxiliary systems usually falls into two categories: Converged or far apart.



where the auxiliary and reference systems have gone into different basins of attraction and where they have converged.

From the point of view of the auxiliary system method, the actual transition between the synchronized and incoherent regimes is unclear. It is possible that with the right choice of perturbation, synchronized systems could have been found for even smaller  $\kappa$ . This uncertainty is eliminated by the SMI.

The results in Figure 3.1 also show that the maximum values of  $d(\kappa)$  are not outliers. There is a real risk that the auxiliary system will settle on a different attractor from the reference system. In the early work on the comparison,  $d$  was calculated for only a single displacement at each  $\kappa$ . In the transition from incoherent to synchronous regime,  $d$  would make several jumps, indicating a change from synchronous to incoherent and back for several consecutive  $\kappa$ .

In Section 2.4 it was shown that the SMI is exactly 1 for synchronized systems and synchronized systems only. This is true if the distribution underlying the time series is known perfectly. However, in reality, this is not the case. We have to estimate the probability distribution from the available data. This means that even in fully synchronized systems, our SMI will not be 1. As we can see in our example, the contrast between synchronized and incoherent systems is nevertheless strong enough to be a useful measure for both,  $\text{SMI}^1$  and  $\text{SMI}^3$ .



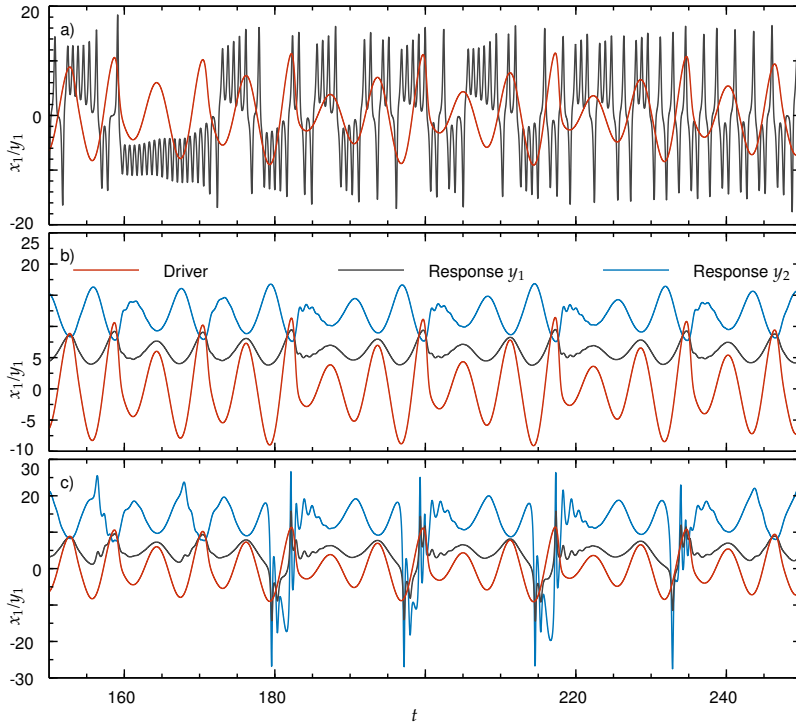


Figure 3.2: The results of the SMI in Figure 3.1 are confirmed by visual inspection of some trajectories. Sample trajectories of the first component of the driver and response systems for a)  $\kappa = 1$ , b)  $\kappa = 2$  and c)  $\kappa = 3$ . In a)  $x$  and  $y$  are decoherent, for b) and c) they are synchronized. In c) we observe amplitude "bursts" in the response system. While still synchronized, these bursts might be the reason for the decreased  $\text{SMI}^3$  at  $\kappa \approx 19$ . In b) and c) we show  $y_2$  in addition to  $y_1$  and  $x_1$ . It shows a blow-up of the difference between the minimum and maximum values for  $\kappa = 19$ .

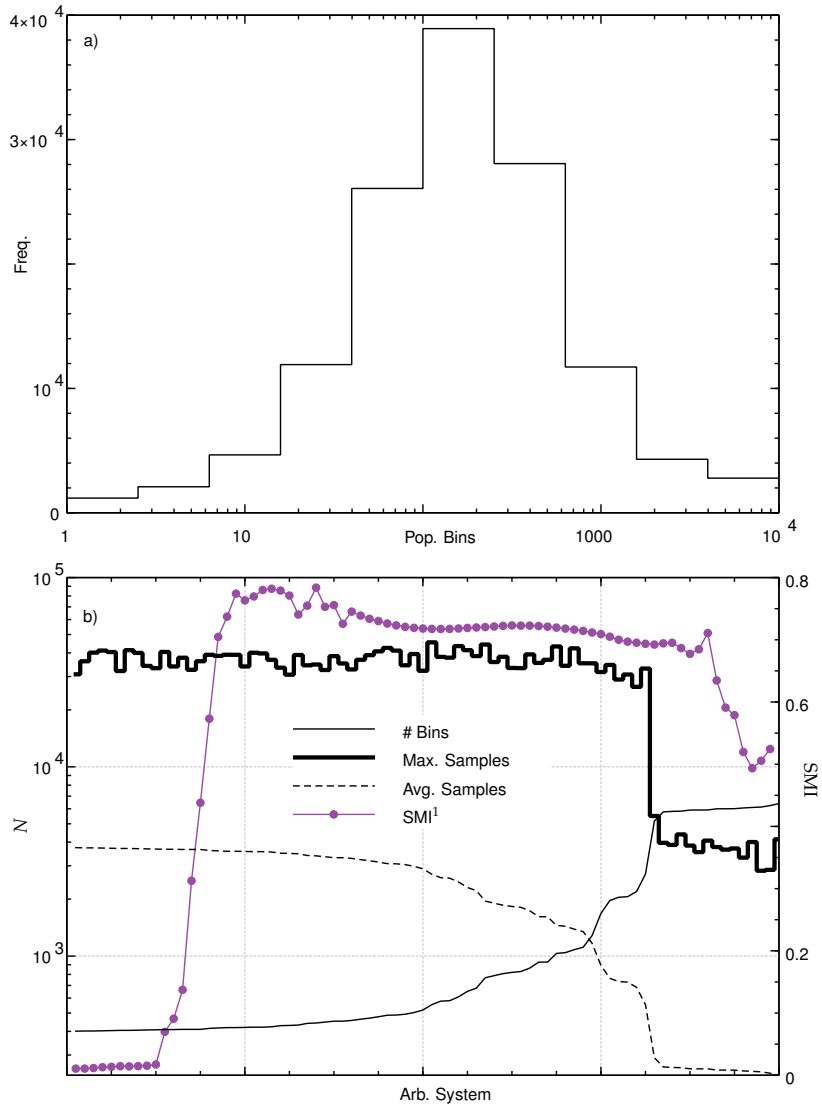
Already in Section 2.6.4 we saw that the performance of the SMI is limited by the quality of the estimation of our probability distribution. With finite sampling and phase space resolution, a SMI of 1 is only expected in rare cases, especially in multidimensional systems. However, imperfect knowledge is part of any numerical method. We will concentrate on the sharp contrast between the synchronous and asynchronous regimes.

In Figure 3.1, we observe a decrease in  $\text{SMI}^3$  for  $\kappa \approx 19$ . So far, the reason for this decrease is unclear, as the systems are synchronized. The  $\text{SMI}^1$  does not show this decrease. In Figure 3.2 we compare the trajectories for  $x_1$  and  $y_1$  for different  $\kappa = 1, 10, 19$ . Additionally, in Figure 3.2 b) and c) we also plot  $y_2$ . Comparing  $y_2$  with  $\kappa = 10$  and  $\kappa = 19$  we see sporadic increases in amplitude. Due to the binning process, this can decrease the efficiency of the binning and the decreased contrast in  $\text{SMI}^3$ .

Since  $\text{SMI}^1$  operates on the  $x_1$  and  $y_1$  components, we do not see such a decrease. By comparing  $x_1$  and  $y_1$  for  $\kappa = 10$  and  $\kappa = 19$ , we find that the difference between the minimum and maximum values does not increase as strongly, leading to a more efficient use of the bins.

As for each time series, there are a high number of possible bins ( $10^6$ ) for  $\text{SMI}^3$ , and undersampling can occur. For undersampled systems, the SMI cannot distinguish between synchronous and incoherent systems. Since we have only 750,000 data points per system, a homogenous distribution of the points in the phase space would lead to undersampling.

Figure 3.3: While naive calculations of the average number of samples per bin for the SMI<sup>3</sup> suggest undersampling with our binning approach, we can show that in practice most of the bins are empty, while the rest are well sampled. With a resolution of 10 bins in each dimension, the phase space for each of our models is divided into 10<sup>6</sup> bins. For a homogeneously sampled phase space and the 750000 samples recorded for the Lorenz/Rössler system, this would result in an undersampling of the phase space. The number of populated bins  $N$  is shown in a histogram in a) for all Lorenz/Rössler systems. A bin is populated if it contains at least one sample. Our results show that most of the bins have no samples, decreasing the number of relevant bins several orders of magnitude below the theoretical maximum, resulting in a potentially well-sampled SMI. In b), we show the maximum number of samples for each system, along with the respective number of populated bins  $N$  and their SMI. The models are sorted by  $N$ .



In Figure 3.3 a) and b) we can see the population of the bins. First, we recognize that in Figure 3.3 b) the number of populated bins is well below 10<sup>4</sup>. This leaves more than 75 samples per bin on average—enough for a good estimate. We can also see from Figure 3.3 a) that most of the bins have more than 50 samples.

In Figure 3.3 a) we can also see the distribution of the population of the bins. We observe that most of the bins have a sufficient number of samples. Figure 3.3 b) also shows the maximum and minimum amount of samples per bin. We used two methods to evaluate the bin population. As a first approach, we count how many bins have a non-zero population. Second, we artificially decreased the amount of available data and checked whether we still would derive meaningful results. In Figure 3.4 we show the convergence of the SMI<sup>3</sup>.

The sampling is further tested by checking the stability of the SMI as the sample length varies. If the SMI converges as the sample length

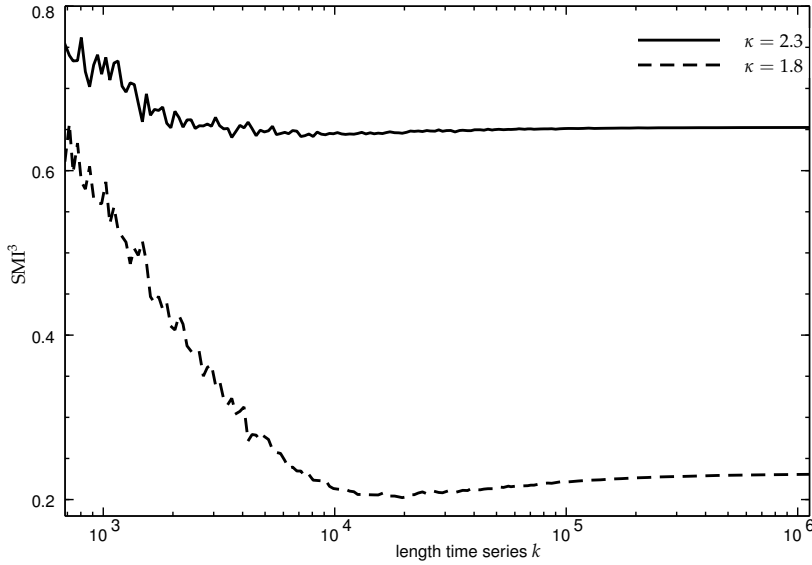


Figure 3.4: We can show that the  $\text{SMI}^3$  converges to a stable value with the chosen number of samples for both the synchronized and the unsynchronized regime. To see if the results for the  $\text{SMI}^3$  can be attributed to undersampling, we checked its convergence behavior by reducing the number of available samples. The number of samples to which the  $\text{SMI}^3$  was applied is given by  $k$ . Plotted are two systems for  $\kappa = 1.8, 2.3$  (one value before and one after the synchronization threshold of  $\kappa$ ). Both systems show that they have converged to a stable value when more than  $10^5$  samples are used. In our findings, we calculated the  $\text{SMI}^3$  (and  $\text{SMI}^1$ ) with even more samples and consequently don't expect any increase or decrease in the results.

increases, this is a sign that the best estimate has been obtained with the current setup. We have plotted the convergence of the  $\text{SMI}^3$  for  $\kappa = 1.8, 2.3$  in Figure 3.4. By skipping every  $n$ -th value vector in a time series, we reduced the available samples without changing the dynamics of the system. The length of the longest time series is the data we used in our evaluation above. From the plot, we can see that the  $\text{SMI}^3$  has converged well.

As the result for the  $\text{SMI}^3$  converges with the available  $10^6$  samples, we did not perform similar tests for the  $\text{SMI}^1$ . The number of dimensions is reduced in  $\text{SMI}^1$ , while the number of samples per trajectory remains the same, so undersampling becomes much less of a problem. A time series with a length of  $10^6$  samples has enough samples for the 20 different bins for each of the systems.

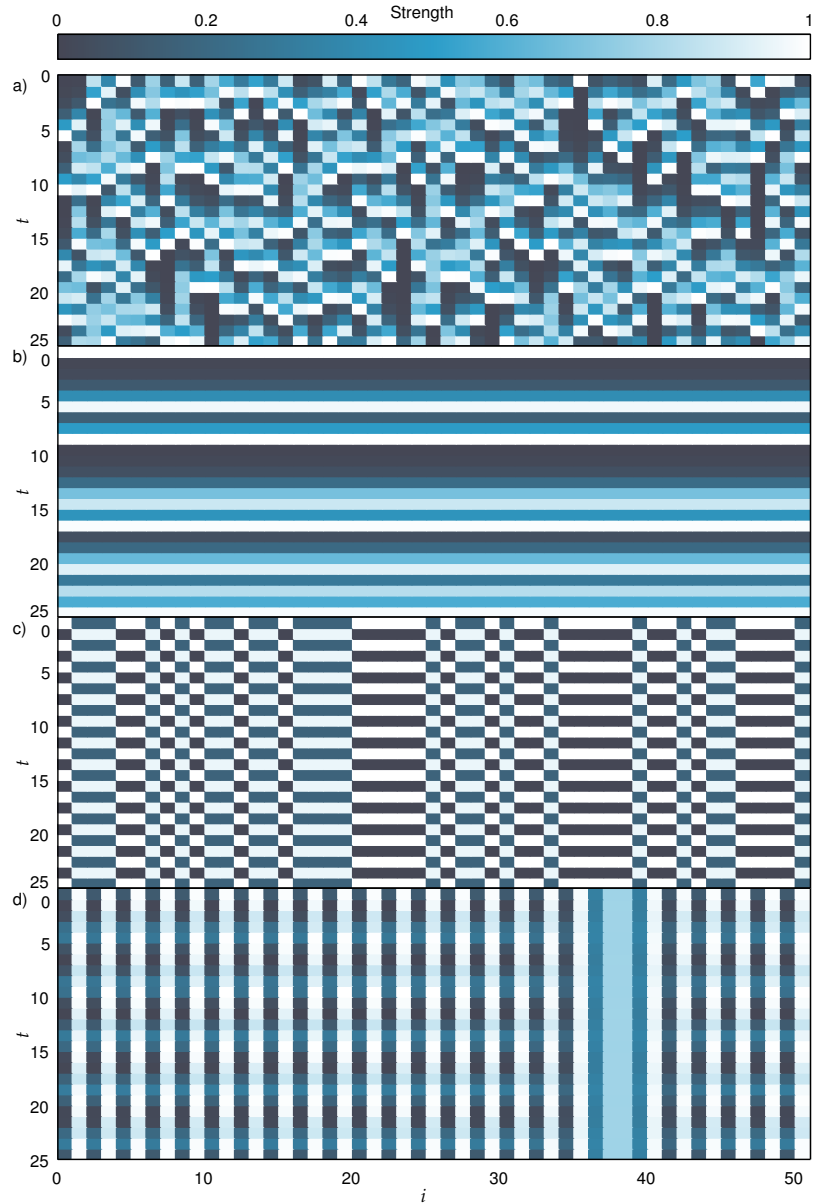
The results show that even with a simple binning scheme, the SMI is a reliable estimator for synchronization. Even with a reduced phase space, the  $\text{SMI}^1$  was still able to contrast between the synchronous and decoherent regimes.

### 3.2 Linear Chain of Logistic Maps

Having shown the performance of the SMI for a driver/response system, we now turn to the study of the synchronization of mutually coupled logistic maps. We have discussed the logistic map previously in Section 1.1.2.

The setup of our work was proposed in [Ant17; Con18]. The authors construct a coupling scheme that allows for continuous transition from next-neighbor to homogeneous coupling with a single parameter. Additionally, a delay of one step can be introduced. In their work, the authors tested for identical synchronization.

Figure 3.5: Snapshots of a system of coupled logistic maps with different coupling parameters show a variety of types of synchronization as well as an unsynchronized model. Snapshots of the linear chain of logistic maps from Equation (3.9) were created with different coupling values  $\epsilon$  and  $\beta$  were created. The columns show different oscillators  $i$  in the system, and their respective values at a time step  $t$  are color-coded. The snapshots show the systems in different regimes of synchronization. a) shows the uncoupled regime and no synchronization, b) shows IS, c) and d) are in the regime of GS.



This restriction allows them to derive analytical limits for regimes of synchronous parameters. In Figure 3.5 we see snapshots of four different systems with different coupling parameters.

However, their work is limited to IS. Figure 3.5 shows a slice of the system proposed in [Ant17]. While Figure 3.5 a) shows an uncoupled system, the other snapshots show synchronous behavior. Only Figure 3.5 b) experiences IS, Figure 3.5 c) and d) can be identified with GS. As we shall see, the SMI allows us to extend the sensitivity in a typical toy model.

The SMI is calculated between two systems. In a multi-component system, the two-component SMI must be aggregated to estimate the state of all components. We will discuss two schemes for such aggregation. The results in this section are taken from [Wis23].

### 3.2.1 System Dynamics

The coupling scheme proposed in [Ant17] is based on a linear chain of logistic maps. It allows a continuous transition between the next-neighbor and global coupling configuration via a single parameter  $\alpha$ . The nodes also feature delayed self-feedback.

The coupling to neighboring maps is given by

$$D(r) = r^{-\alpha} / \sum_{l=1}^{N'} l^{-\alpha} \quad (3.6)$$

with the distance  $r = |i - j|$  of maps  $i$  and  $j$ . Since we go in each direction of the chain, we only sum over half of the components,

$$N' = (N-1)/2 \quad (3.7)$$

and thus  $N$  must be a multiple of 2. Normalization ensures that the contributions from all the maps do not exceed 1. This is necessary since the logistic map diverges for values outside the range between 0 and 1.

The neighborhood parameter  $D(r)$  can be continuously adjusted between global coupling ( $\alpha = 0$ ) and local coupling. For  $\alpha \rightarrow \infty$  each component is coupled only to its nearest neighbor.

A one-step delay feedback is realized with the coupling parameter  $\beta$ , the general coupling can be tuned with  $\epsilon$ . The delay is realized as a diffusive coupling

$$\hat{x}_i[t] = \beta x_i[t-1] + (1-\beta)x_i[t] \quad (3.8)$$

which can account for delayed and non-delayed dynamics.

Combining the delay from Equation (3.8) together with the weights of the Equation (3.6), the system is defined as:

$$x_i[t+1] = (1-\epsilon)F(x_i[t]) + \epsilon \sum_{j \neq i}^N D(|i-j|)F(\hat{x}_j[t]). \quad (3.9)$$

The parameters  $\epsilon$ ,  $\beta$  and  $\alpha$  ensure that the values of  $x_i[t]$  are always bound by  $[0, 1]$ . The local dynamic is given by the logistic map

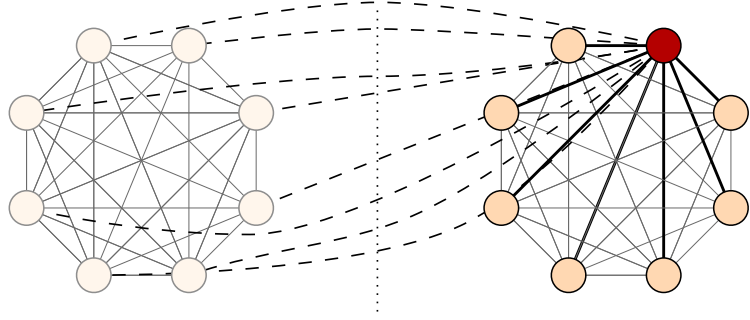
$$F(x[t]) = 4x[t](1-x[t]). \quad (3.10)$$

Figure 3.6 shows an exemplified coupling for a network of 8 oscillators.

### 3.2.2 Extension from Pairwise SMI

Two options present themselves when extending the pairwise SMI as a measure of synchronization in a cluster. IS can be identified with the synchronization error, a deviation from the mean-field for each component.

Figure 3.6: Coupling scheme of the ring network given in Equation (3.9). All possible couplings are given for an example oscillator (red node). The coupling strength to neighboring oscillators can be changed depending on their distance (bold lines). The coupling into the past can be tuned into all nodes at the same strength (dashed lines) so that the oscillators effectively see the mean-field of the past system.



In [Ant17]) this is achieved by measuring the mean synchronization error over all trajectories

$$\sigma^2 = \frac{1}{T} \sum_t \sqrt{\frac{1}{N} \sum_j^N (x_j[t] - \langle x_k[t] \rangle_k)^2} \quad (3.11)$$

where  $\langle x_k[t] \rangle_k$  is the average overall trajectories for a point in time  $t$ .

Our first proposed extension of the SMI is based on the mean-field approach of the synchronization error. A mean-field trajectory  $Z$  is the set of the sum of all values for each timestep  $t$

$$Z = \left\{ \frac{1}{N} \sum_j x_j[0], \dots, \frac{1}{N} \sum_j x_j[T] \right\}. \quad (3.12)$$

The synchronization will be calculated relative to the mean-field of the system. This gives us the Mean Field Synchronized Mutual Information (MFSMI)

$$\text{MFSMI}(X_i \dots; Z) = \frac{1}{N} \sum_i \text{SMI}(X_i; Z) \quad (3.13)$$

with  $N$  being the total number of elements.

However, in this approach, we lose much of the information between individual components to the mean-field. Therefore, the second proposal preserves these relationships by calculating the pairwise SMI. The average of these pairwise synchronizations then gives the Average Synchronized Mutual Information (ASMI)

$$\text{ASMI}(X_i \dots) = \frac{2}{N(N-1)} \sum_{i,j < i} \text{SMI}(X_i; X_j). \quad (3.14)$$

In the case of IS, the mean-field of the system is equal to each of its components. Therefore, we expect that both previously proposed aggregation schemes to identify IS. However, for regions where the system is in IS, we expect different results. The MFSMI expects all systems to synchronize to their common mean-field, while the ASMI expects all systems to synchronize with each other.

In order to illustrate the difference between the two measures, let us look at a simple example before applying them to the system of

logistic maps. Three trajectories  $X_1$ ,  $X_2$  and  $X_3$  are going to consist of repeating patterns given by

$$\begin{aligned} X_1 &= [\dots, 2, 7, 8, 4, \dots] \\ X_2 &= [\dots, 6, 4, 7, 4, \dots] \\ X_3 &= [\dots, 4, 4, 0, 4, \dots] \end{aligned} \quad (3.15)$$

resulting in a mean-field trajectory

$$Z = [\dots, 4, 5, 5, 4, \dots]. \quad (3.16)$$

While the SMI between each system yields one, the average of the mean is not able to preserve the structure of all trajectories. As expected, this results in the  $\text{ASMI} = 1$  while  $\text{MFSMI}$  is smaller than 1.

We compare both measures to see if these differences are observed in practice. The main advantage of the  $\text{MFSMI}$  is its scaling with the number of components in the system. While for the  $\text{ASMI}$ , the number of calculations grows with  $\frac{N^2}{2} - N$ , the  $\text{MFSMI}$  grows only linearly with  $N$ .

There is also an approach to the problem of multiple systems of synchronization. The MI can be extended from a comparison between two random variables to a multivariate mutual information. Its properties are, however, vastly different from the univariate MI so it is not clear if a synchronization measure can be constructed. This is a topic of further research and will not be explored in this work.

### 3.2.3 Results

We want to compare the results of [Ant17] for identical synchronization with the mutual information. Therefore, we replicate the coupling scheme and search for synchronization in the parameter range. Simulations of Equation (3.9) are carried out using *python 3.7* [Olio7] with the *numpy 1.18* [Har20] library and with *snakemake 5.19* [Kös12].

Simulations are carried out for the parameters given in Table 3.2. We use  $N = 51$  maps for the simulation and a total of 1100 steps.

Parameter	Value/Range
$r$	4
$\epsilon$	$[0, 1]$
$\beta, \beta_{L_1}, \beta_{L_2}$	$[0, 1], 0.3, 0.8$
$\alpha, \alpha_L$	$[0, 3], \infty, 0.5$
$N$	51
$T_E$	1000
$T_M$	100
$\Theta_\sigma$	$< 10^{-6}$
$\Theta_{\text{total}}, \Theta_{\text{local}}$	$> 0.95$

Table 3.2: Parameter and parameter range for the simulation of the coupled logistic map Equation (3.9).

Initial values are randomly generated using the Mersenne-Twister algorithm [Mat98]. Since we need an additional delayed state, two initial states  $x_i[t] \in [0, 1]$  are created. The first  $T_E = 1000$  time steps are omitted, allowing the system to converge to its attractor. This leaves  $T_M = 100$  steps to apply the SMI to.

A system is in IS if  $\sigma$  from Equation (3.11) approaches zero. To account for the finite precision and time of our simulation, we choose a cut-off value  $\sigma < \Theta_\sigma = 10^{-6}$  where we classify two systems to be synchronized.

For the application of MFSMI and ASMI we discretize each trajectory by sorting the values into 10 bins evenly distributed within the minimum and maximum of each trajectory. We then calculate the mutual information-based synchronization measure SMI using the Grassberger algorithm with the implementation proposed in Section 2.6.3.

As discussed in Section 3.1.2, the SMI is not expected to approach one. Finite sampling and the finite number of bins allow for an imperfect sampling of the distribution.

As a threshold for synchronization, we choose  $\Theta_{\text{MFSMI}} = \Theta_{\text{ASMI}} = 0.95$ . The thresholds  $\Theta_\sigma$ ,  $\Theta_{\text{total}}$  and  $\Theta_{\text{local}}$  were chosen empirically, the results are stable for small perturbations of the threshold.

In Figure 3.7, the effect of the chosen threshold on the classification is shown. Figure 3.7 a) shows the number of systems identified as synchronous by ASMI and MFSMI as a function of the chosen threshold. In Figure 3.7 b) we see the same for IS.

As can be seen from these comparisons, the chosen threshold can be changed significantly without changing the result of the experiment. For  $\sigma$  in Figure 3.7 a), we see that we can change the threshold by several orders of magnitude without producing a relevant change in the output.

In Figure 3.7 a) we can see a small artifact from the estimation of the SMI: The ASMI can give negative values. The MI estimator proposed in Equation (2.60) is a combination of Grassberger entropy estimators. Although the bias of the naive entropy estimator is eliminated with the estimator proposed by Grassberger, it does not retain the properties of MI.

As in the original work of [Ant17], we compare the ASMI, MFSMI and  $\sigma$  with the Lyapunov exponent of the system (see Section 1.1.1). The maximum Lyapunov exponent is given by  $\beta_{L_{1,2}} = 0.3, 0.8$  and  $\alpha = 0.5$  with the algorithm given in the Appendix Section A.1. The results are plotted in Figure 3.8 for  $\epsilon \in [0, 1]$ .

The Lyapunov exponent indicates that the chaotic regime of the linear chain falls within the same region where MFSMI and ASMI show no synchronization. For  $\beta_{L_1}$  chaotic behavior vanishes for  $\epsilon \sim 0.3$  where the systems (as indicated by MFSMI and ASMI) shift to the synchronous state. In contrast, identical synchronization is



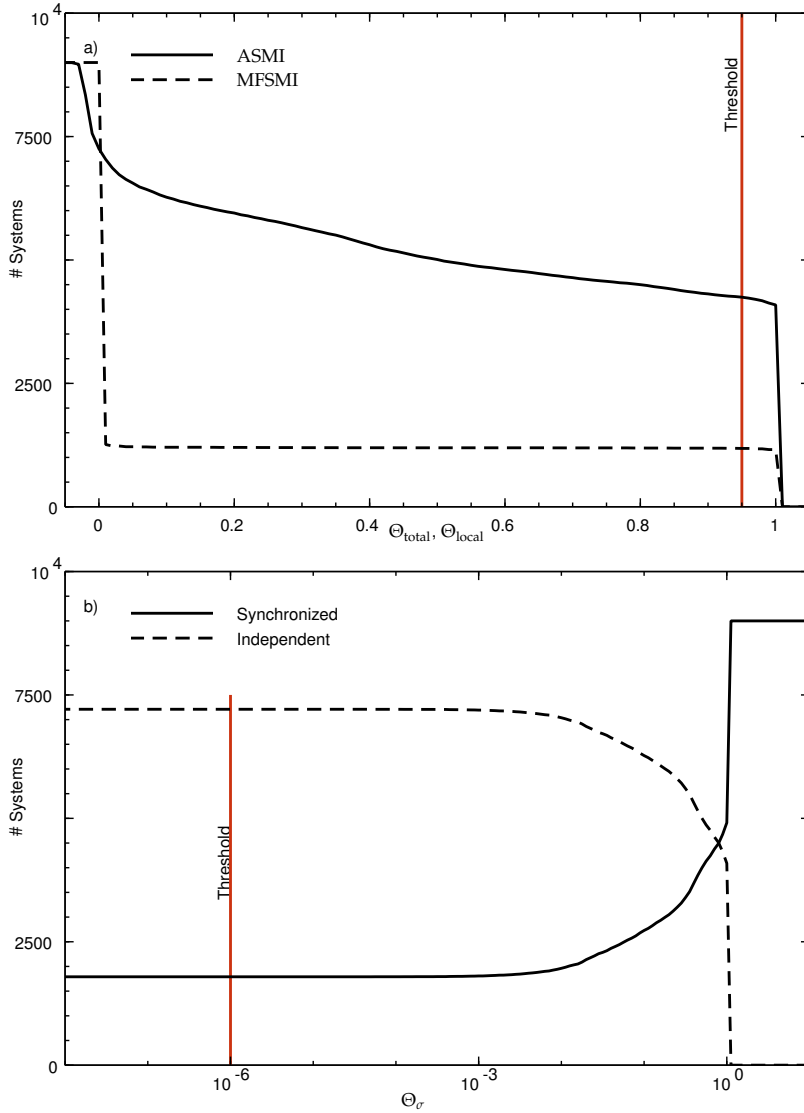


Figure 3.7: Changing the threshold of the SMI and  $\sigma$  within reasonable limits doesn't change the outcome of our results. To show that our thresholds for  $\sigma$ , MFSMI, and ASMI are well-founded, we compare them with variations of said thresholds. The number of synchronized systems is plotted as a function of the threshold. Additionally, the threshold used within this work is marked as a red line. In a) the function is given for MFSMI and ASMI, and b) shows the values for  $\sigma$ . We can see that, within reasonable limits, changes in the threshold don't affect our results, as few systems would switch from the synchronized to the unsynchronised regime and vice versa.

registered for  $\epsilon \sim 0.4$ . We observe similar results for  $\beta_{L_2}$  with a synchronous/non-chaotic island at  $\epsilon \sim 0.2$ .

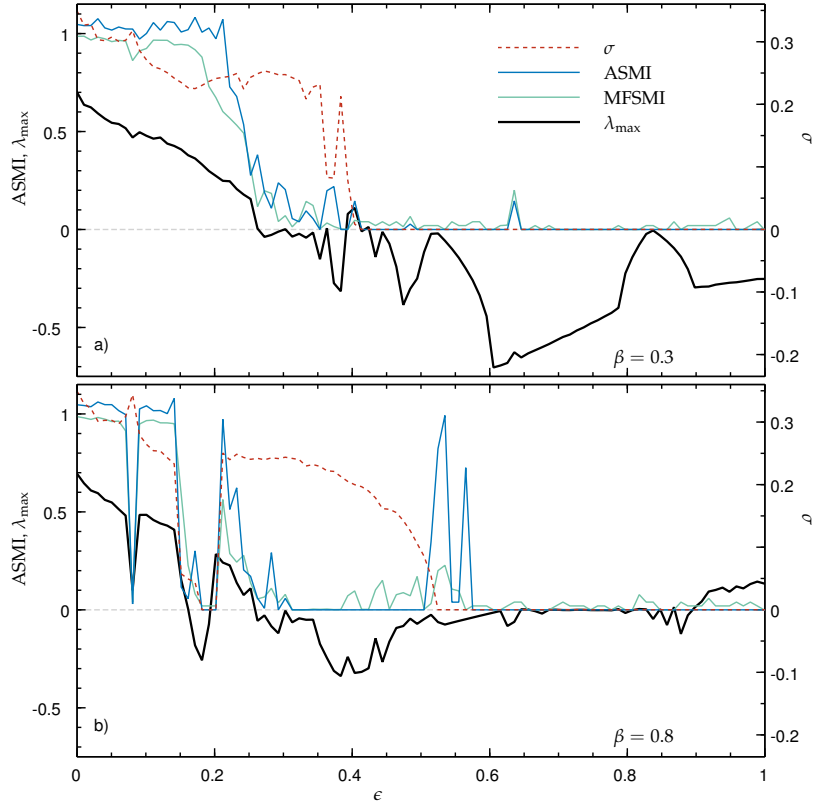
However, identical synchronization is lost until  $\epsilon \sim 0.6$ , ASMI and MFSMI only indicate a short asynchronous regime. An interesting observation is the increase in the MFSMI and the ASMI in  $\epsilon \sim 0.55$  where  $\sigma$  tends to 0.

Interesting is also the behavior for  $\epsilon > 0.9$  where the system shifts into a chaotic regime while  $\sigma$ , MFSMI and ASMI indicate synchronization.

We also see that the ASMI identifies the synchronous regimes of the MFSMI plus extra regimes. This is consistent with what we expected from the derivation of the measures in Section 3.2.2 and shows that there are practical differences between ASMI and MFSMI.

To further explore the difference between ASMI and MFSMI further and compare them to IS we increase the parameter space in our sim-

Figure 3.8: The MFSMI doesn't work as expected in all cases, the ASMI is more generally applicable when synchronization between all oscillators in a system is of interest. The largest Lyapunov exponent (see Section 1.1.1) from the linear chain described in Section 3.2. Results are shown for  $\beta = 0.3$  a) and  $\beta = 0.8$  b). Together with the Lyapunov exponent, we have plotted the SMI as a function of  $\sigma$ . For better readability, the SMI is plotted as  $1 - \text{SMI}$  and is now synchronous for 0. As we can see, synchronization can still appear while the system is in a chaotic state, though this seems only to be the case for generalized and not identical synchronization. Also here, it is obvious that the SMI covers a larger area of synchronization. It also shows that the mean-field MFSMI is less general and shows artifacts for  $\epsilon \approx 0.5$  and  $\beta = 0.8$ .



ulations.

We run simulations for  $\beta \in [0, 1]$ ,  $\epsilon \in [0, 1]$ . For  $\alpha \in [0, 3]$  we execute dense simulations and additionally next-neighbour coupling with  $\alpha \rightarrow \infty$ .

The results are shown in Figure 3.9 as a color-coded map where  $\sigma$ , MFSMI and ASMI are the detected synchronizations. Color-coding shows the intersections of the regimes of the three synchronization measures.

Important are the gray regions where all regions found synchronization. We see that the regimes of IS are completely covered by MFSMI and ASMI, as well. For  $\beta = 0.4$  and  $\beta = 0.3$ , we find a few cases where there is a regime of MFSMI but not ASMI. The opposite, where we have regimes of ASMI but not of MFSMI, are visible for different ranges and show that ASMI is also more extensive in practice. We also see larger regimes of both ASMI and MFSMI without identical synchronization. This is particularly interesting for  $\beta \in [0, 0.3]$ , where there is an additional island of synchronization for  $\epsilon = 0.3$ , which is not seen with with IS.

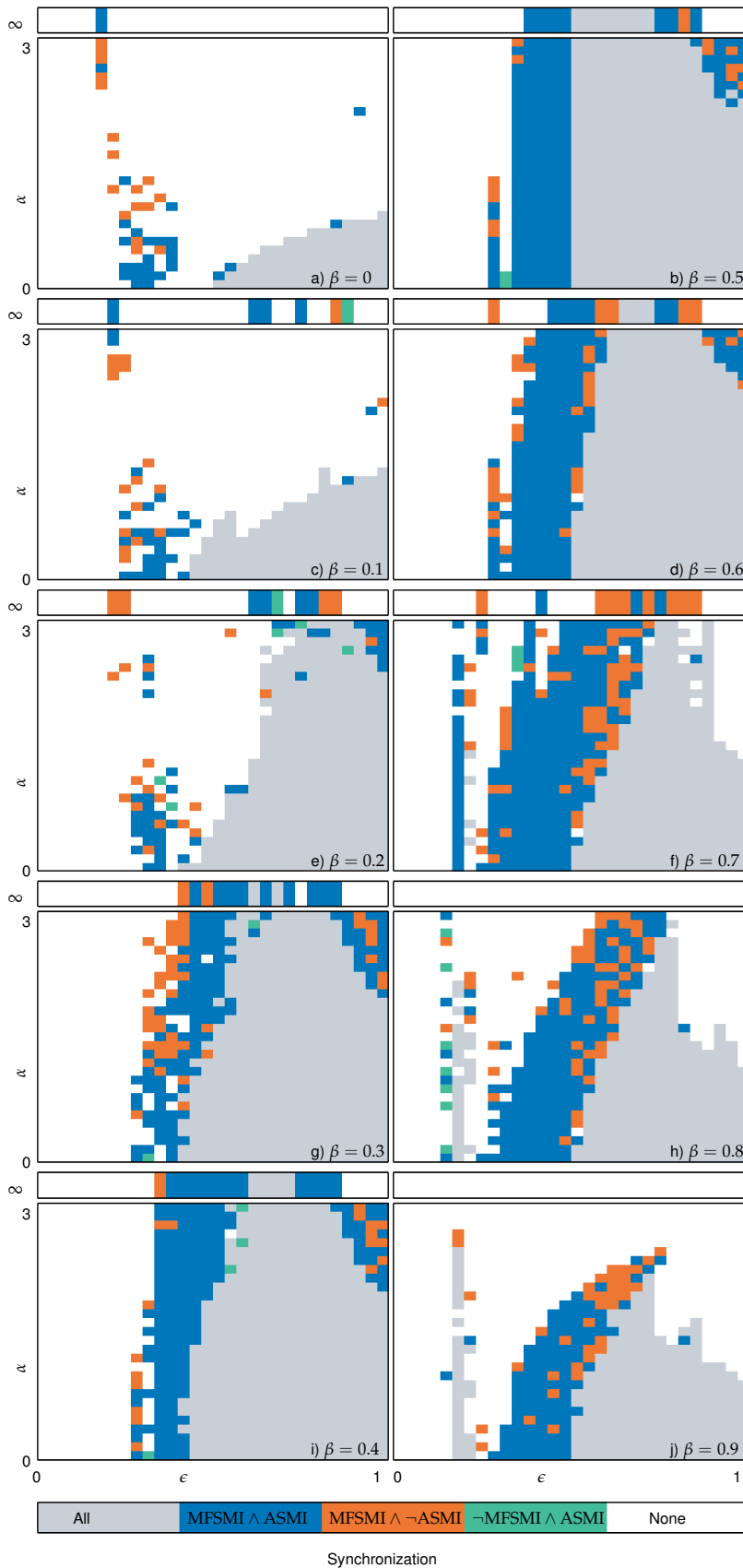


Figure 3.9: Using the SMI we can unveil new regimes of synchronization in a system of coupled logistic maps (Equation (3.9)). We compare three different measures of synchronization  $\sigma$ , MFSMI and ASMI for the linear chain of logistic maps. We have used logical operators to distinguish between the different cases. The  $\wedge$  represents an *and* operation and  $\neg$  represents an inversion. All parameters  $\beta$ ,  $\epsilon$ ,  $\alpha$  are varied, and the resulting synchronization regimes are color-coded. A system is regarded to be synchronized where its relevant measure exceeds some threshold. Gray marks the regimes where all measures show synchronization. This implies that these are also the regimes of IS. MFSMI  $\wedge$  ASMI shows areas with both ASMI and MFSMI, MFSMI  $\wedge$   $\neg$ ASMI is without ASMI and  $\neg$ MFSMI  $\wedge$  ASMI without MFSMI. Figures a) to c) show that a new island of synchronization forms for  $\epsilon \approx 0.3$ . The main regime of synchronization expands considerably compared to the IS only case.

### 3.3 General Remarks

As already discussed in Section 2.6.4 due to the finite samples and bin sizes, the SMI does not approach 1, even in synchronous phases. However, for both the driver/response and the linear chain, we observed a strong contrast between synchronous and asynchronous areas.

For the driver/response system in Section 3.1 we found that the SMI performs well in identifying synchronization, even avoiding the pitfalls of the auxiliary system method. We tested the applicability of the method for incomplete phase spaces by calculating the SMI for a single dimension only.

As we have seen from the results of Section 3.2, clear results can be achieved with only a few available samples. We can see a strong contrast between synchronized and decoherent regimes with only 100 samples per trajectory.

Furthermore, we were able to see that GS often "pre-empts" IS in a transitory regime: Some parameters first show GS that later manifests itself in IS for continuous tuning. Previously, logistic maps were prepared for IS. We are unaware of any studies on coupled maps that are sensitive for GS.

# Partial Synchronization & Complex Networks

In the previous chapter, we studied systems more complex than two-component synchronization with linear logistic chains. We observed synchronization between multiple oscillators after a long equilibration time. In the previous study, the system would either converge on a synchronous trajectory from random initial values, or it was considered to be asynchronous. Analyzing the state of the system, we disregarded other dynamics such as the transition from the initial state to the synchronized state. Furthermore, the extended SMI based uses are only sensitive to dynamics where each component of the system is synchronized with each other.

However, these limitations raise the question of whether other interesting phenomena can be detected in the transients, in a subset of the components, or whether a non-equilibrium state exists. Research on this partially synchronized system came into focus after the notion of synchronization was well established, around 2004. It was started by finding so-called chimera states.

The chimera is a creature of Greek mythology with the body of a lion, the head of a goat, and the tail of a snake. For our purposes, it describes a system in which the symmetry of synchronization is broken, with one cluster in a synchronized state and the other in an incoherent state. The first description of the phenomenon is generally attributed to [Kuro2]<sup>1</sup>, the notion of the chimera state was coined in [Abro4].

Chimera states can be found as long-lived transients between the initial, incoherent, and synchronized states. In these cases, it was shown that the chimera's lifetime scales with the size of the system [Tum17]. In [Ome18; Sie14] feedback techniques have been proposed to stabilize transient chimeras in small systems. More recently, network topologies have been proposed in which stable chimera states are found in networks consisting of only six (chaotic) components. [Zha21].

Further progress has been made in increasing the stability of the chimera states for larger ranges of initial conditions. Due to a smaller

<sup>1</sup> Although some sources disagree with this assessment (e.g. [Hau21]), noting that with the modern understanding of chimera states, similar phenomena are described much earlier in [Kan90].

basin of attraction (compared to the synchronized state), chimera states are harder to find [Sch21]. Since then, the situation has changed, and in more recent configurations (e.g. [Zha21]), chimera states can be observed for most initial conditions.

It should be noted that due to its recent development and the notion of a chimera, the state has some ambiguity [Hau21]. While it was initially coined for clusters with matched and unmatched frequency of regular (phase) oscillators, the term is also used for amplitude mismatches (with matching phases) of in systems consisting of coupled chaotic oscillators.

Chimera states are of special interest in the research on biological neuron networks where they are connected with the sleeping patterns and learning in the brain [Wan20; Kan19; Ban19; Rod19], found application in chemical oscillators [Nko13; Rod19] or social studies [Gon14].

Similar to chimera states, the decomposition of a system into clusters of internal synchronization with no inter-cluster synchronization. This cluster synchronization was first described within [Zho06]. In other configurations, components can experience remote synchronization where two components do not share a common synchronized coupling path while still being in sync [Ber20; Wan20].

We conclude this list with the mention of intermittent synchronization. Here, the system fades into and out of a synchronous state. Early research mentions intermittent loss of synchronization and criteria for selecting coupling parameters to stabilize synchronization [Gau96]. Contemporary discourse often focuses on synchronization loss in the context of a neural model [Par11; Ahn17; Rub17]. Intermittent synchronization is often motivated in the context of noise, where external signals can push a system from the synchronized state.

These phenomena can also be observed in combination. In [Zha20] a mixture of intermittent synchronization and chimera states was described. The authors found that even small amounts of noise induced switching of the synchronous cluster. Although none of the clusters is in a permanent synchronous state, each falls in and out of synchronization.

As we have previously discussed (compare Chapter 2), analytical tools are restricted to active experiments, while other methods such as the SMI can be used in passive experiments as well. This assumption continues to hold when seeking to understand partial synchronization. Analytical tools were applied when studying abstract systems (see [Abro4; Par11; Tum17]), alongside numerical tools (e.g. [Kuro2; Ahn17; Ibr21]). When working with real-world systems, numerical tools are even more important (see [Wic13; Tot18; Woj16]).

The methods developed in the previous chapters to identify synchronization can also be used to detect other kinds of synchronization.

In this chapter, we explore various extensions suitable to detect the above-mentioned types of partial synchronization.

We begin the chapter by constructing different aggregations of the SMI for these multi-component systems. These are similar to the aggregations used in Section 3.2. By changing the pattern of aggregation, we seek to be sensitive to a certain type of partial synchronization. Here we also test the extended versions of the SMI for the detection of intermittent and partial synchronization Section 4.2 and Section 4.3.

Section 4.4 shows the detection of chimera states in a network provided by [Zha21] and continues to show a possible reason for the stability of the chimera states.

And finally Section 4.5 tests the performance of the SMI on systems with noise coupling and testing the resilience of different types of networks to noise.

## 4.1 SMI and Partial Synchronization

The SMI as defined in Equation (2.35) is a pairwise measure. To be usable as a synchronization identifier for large clusters of oscillators, we proposed an extension in Section 3.2.2. The construction of the previously proposed ASMI is insufficient for only partially synchronized systems, since systems without (local) synchronization are indistinguishable from a somewhat coherent system.

We propose two extensions to the SMI that increase the contrast between the Partial Synchronization (PAS) and the sporadically coherent system. First, we present a windowed SMI that allows the calculation of the measures of the running window and also a maximum value approach for the pairwise SMI.

We test the application of both methods on intermittent cluster synchronization. The application to chimera states is discussed in Section 4.4.

### 4.1.1 Measures

Within this section, we explore various patterns of aggregation over time. We will refer to a single time series with  $X_i$ . A moment in a time series is denoted with  $X_i[t]$ , a slice of the same is denoted by  $X_i[t : l]$ , with  $t$  being the starting point of the slice and  $l$  the length of the slice.

To be sensitive to temporal unstable synchronization, using the full trajectory of a component is infeasible. By calculating the SMI on windows of the trajectory, we can assess the synchronization localized in the time dimension. We propose the Windowed Synchronized

Mutual Information (WSMI)

$$\text{WSMI}_t^l(X; Y) = \text{SMI}(X_i[t : l]; X_j[t : l]). \quad (4.1)$$

The WSMI allows us to evaluate the temporal development of the synchronization as it is done in intermittent synchronization [Rub17]. In neuronal research, this is often done by reconstructing a phase relationship between neurons [Ahn17].

For larger systems, visually keeping track of all pairwise information (e.g. by plotting the SMI in a matrix) gets out of hand quickly. In section Section 3.2.2 we expected full synchronization and thus we could look at the average of all pairwise SMIs with the ASMI. For PAS this aggregation method is not sufficient. Since we do not expect synchronization of all components at all times, a simple average will lose features of the underlying synchronization patterns. As an alternative, we propose an alternative aggregation method based on finding maximum pairwise synchronization. We define the Maximum Synchronized Mutual Information (MSMI) as

$$\text{MSMI}(X) = \max_{i \neq j} [\text{SMI}(X_i, X_j)] \quad (4.2)$$

which returns the largest synchronization between two components.

Of course, we can combine the method for the WSMI and the ASMI and create a running maximum SMI

$$\max_{i \neq j} [\text{SMI}(X_i[t : l], X_j[t : l])]. \quad (4.3)$$

With a repeated reduction to the maximum of the running window maximum SMI we create a measure that is sensitive to a single instance of intermittent synchronization

$$\max_{i \neq j; t:l} [\text{SMI}(X_i[t : l], X_j[t : l])]. \quad (4.4)$$

However, especially the latter equation should only be applied with care, as the chance of observing a high SMI from spurious correlations increases with many windows, effectively lowering the contrast between spurious and systematic synchronization.

#### 4.1.2 Model

To test the proposed measures, we use a modification of the system used in [Zha21]. Initially thought as an example of strong chimeras, the coupling scheme also produces cluster and intermittent synchronization.

Similarly to Section 3.2, Zhang uses a map to build the dynamics of his system. The dynamics of the map are given by

$$x_i[t + 1] = \left( r l(x_i[t]) + \kappa \sum_j L_{ij} l(x_j[t]) \right) \bmod 1 \quad (4.5)$$



with the function  $l(x) = x(1 - x)$ . The coupling strength to the network is given by  $\kappa$ ,  $r$  is the self-feedback and  $L_{ij}$  gives the elements of the connectivity matrix.

This is in contrast to the logistic function  $f(x)$  used in Chapter 2. On the left-hand side of the sum, the logistic function is completed with the parameter  $r$ . The right-hand side completes it with the general coupling strength  $\kappa$  and the pair-specific coupling  $L_{ij}$ . The main difference taken here is the inversion of the coupling term by changing the sign prior to  $\kappa$ .

A second important difference is the modulo operator  $x \bmod o$ <sup>2</sup>. The parameters in Equation (3.9) are carefully balanced so that the results are bound to  $[0, 1]$ . In Equation (4.5) the boundaries are enforced by the modulo operator.

The specific coupling scheme used in  $L_{ij}$  is described in Section 4.4 and the initial work in [Zha21] in more detail. The general idea found in [Zha21] is that stable chimera states can easily be found in systems that consist of two clusters with an internal ring-like structure and a mean-field inter-cluster coupling.

<sup>2</sup> The modulo operator  $x \bmod o$  introduces periodic boundary conditions. Integer multiples of its parameter  $o$  are subtracted/added from or on  $x$  until the result is within  $[0, o[$ . Negative arguments of the modulo operator are also projected within these bounds.

## 4.2 Intermittent Synchronization

Intermittent synchronization describes systems in which its components are synchronized and incoherent. While there exist some reports of intermittent synchronization in nonlinear science [Bak98], more attention is paid to neuroscience where state changes are expected to be vital for the function of the brain [Ahn11; Ahn17; Rub17].

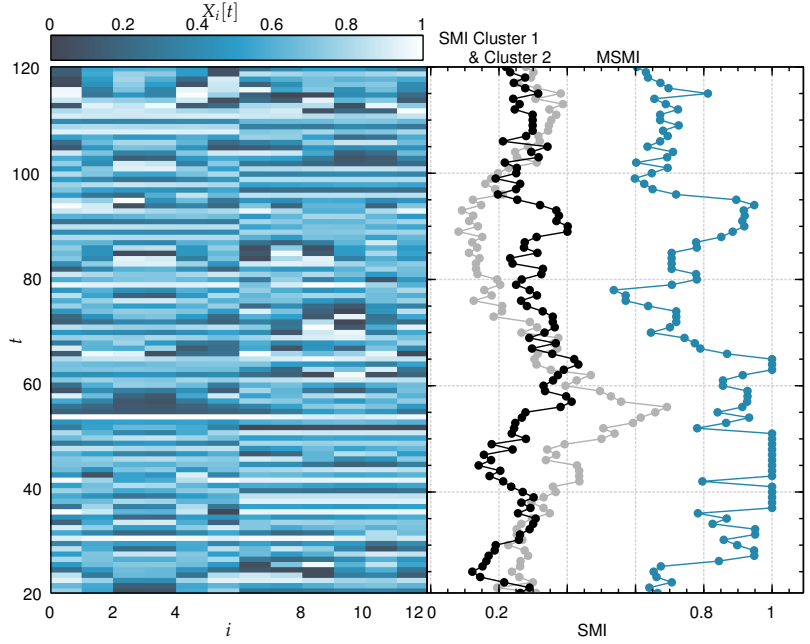
On the basis of Equation (4.5) we found intermittent synchronization with the parameters  $r = 3$  and  $\kappa = 1.3$ . The results are shown in Figure 4.1 with running Windowed Average Synchronized Mutual Information (WASMI) for each cluster and a running MSMI. We see that the running MSMI shows increased values compared to the clusterwise WASMI.

The last phenomenon is due to the fact that the MSMI shows the highest pairwise SMI for each window. As we can see from the time series in Figure 4.1 even within each cluster, the individual components do not experience the same level of synchronization, reducing the WASMI.

In Figure 4.1 we see the limited capabilities of the WASMI to detect intermittent synchronization. As already discussed in Section 2.6.4, estimating the SMI benefits from larger sampling sizes. Synchronization over a limited time can yield insufficient samples for proper distinction from the decoherent phases.

When identifying intermittent synchronization, the user must strike a balance between sample size and the locality of the result. With small sample sizes, the contrast of the SMI between synchronous and decoherent regimes may be small. A larger sample size implies

Figure 4.1: Example for intermittent synchronization. The dynamics are produced with Equation (4.5). The left plot shows the color-coded values of the time evolution for each component  $i$ . Along the time series, we plot the running average WSMI for each cluster  $i \in [1, 6]$ ,  $i \in [7, 12]$ . Additionally, the running ASMI is given. As we see, each cluster shows intermittent synchronization within itself, however, the system is unstable and thus quickly decays into an incoherent state. The clusters are constructed according to the clustering scheme explained previously in Section 4.4.



a larger regime in the trajectory. This limits the locality of the result and, in the case of short periods of synchronization, also the contrast between the synchronized and incoherent regions.

### 4.3 Cluster Synchronization

Cluster Synchronization (CS) is found in systems with partitioned symmetries in their network, e.g., similar coupling for specific cluster [Ber20]. Within such a cluster, the components can then synchronize while not being synchronized to components of other clusters.

Here, we study two (partially) synchronized systems for  $r = 3.9$  with  $\kappa = 1.1$  and  $\kappa = 1.12$  for the system derived in Equation (4.5). In contrast to the results obtained in Section 4.2 and Section 4.4 the results obtained here were generated with a cluster size of 5.

The time series and the local synchronization values for both systems are found in Section 4.3. Next to the time series of the evolution of the components, we plotted the running ASMI calculated for the system and each cluster separately, as well as the running synchronization error

$$\sigma(t) = \left( \frac{1}{N} \sum \left( x_i[t] - \frac{1}{N} \sum x_i[t] \right)^2 \right)^{\frac{1}{2}} \quad (4.6)$$

with  $N = 10$  the total number of oscillators.

Section 4.3 a) shows an example of a system in which both clusters would be identified to be synchronous with itself but not with the other cluster when the measure is only sensitive to IS. When using the SMI, this changes and the system is identified to show global synchronization.

In Section 4.3 b) each cluster still shows IS, however, application of the SMI shows that there is no intercluster synchronization.

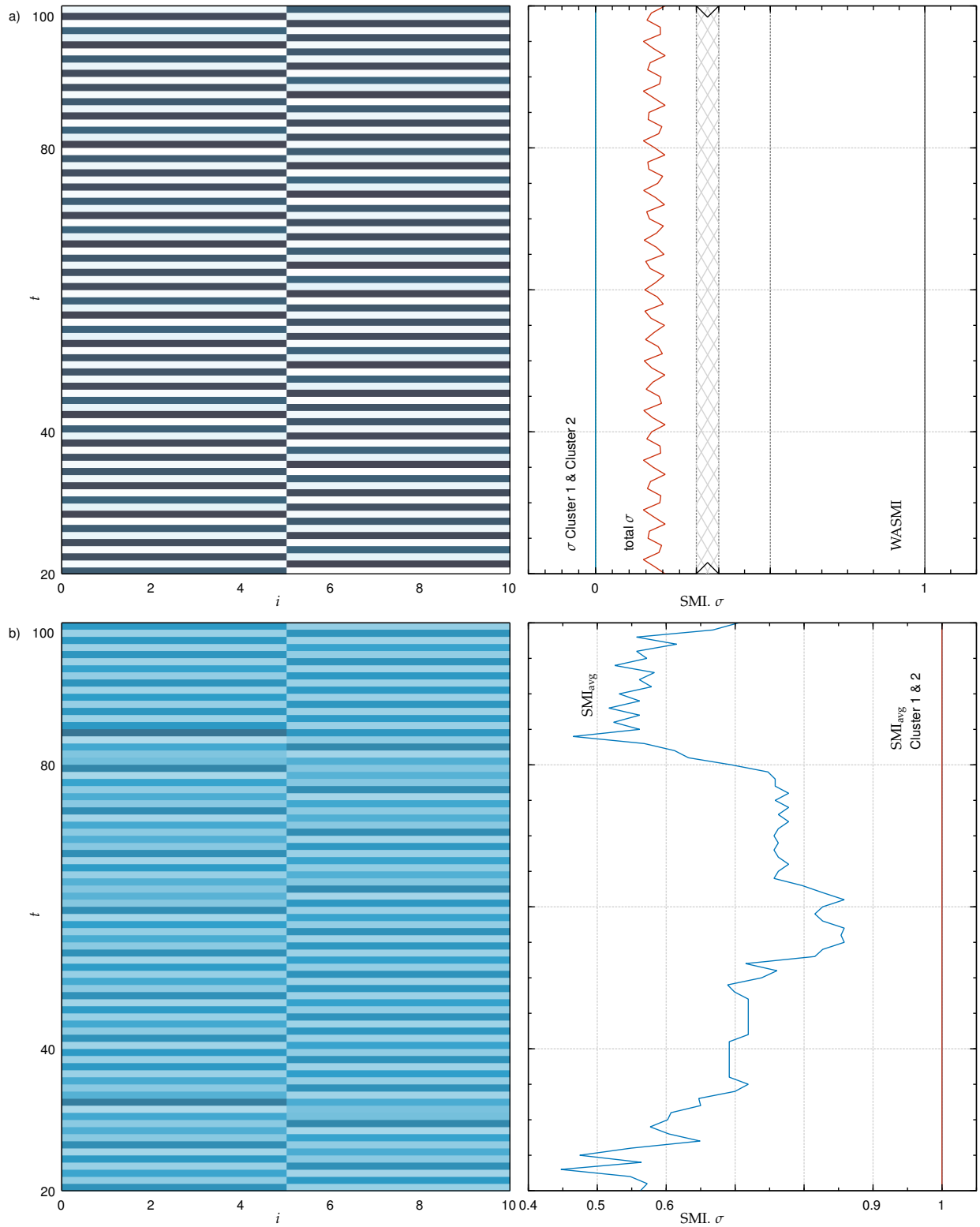


Figure 4.2: An example for cluster synchronization from the dynamics in Equation (4.5). In a) we present a system that experiences cluster synchronization only when considering IS. When calculating the ASMI, the clustering of the synchronization does not present itself. This is contrasted in b), where the ASMI for the complete system shows no synchronization while each cluster in itself is synchronized. The left side of each plot shows the values of each component over time  $t$ . On the right, we see the running average ASMI for the full system and each cluster  $i \in [1, 5]$ ,  $i \in [6, 10]$ .

These results are promising and show that the SMI can easily be adapted to identify CS. Other than in intermittent synchronization, limited sample sizes are of no concern.

#### 4.3.1 Conclusion

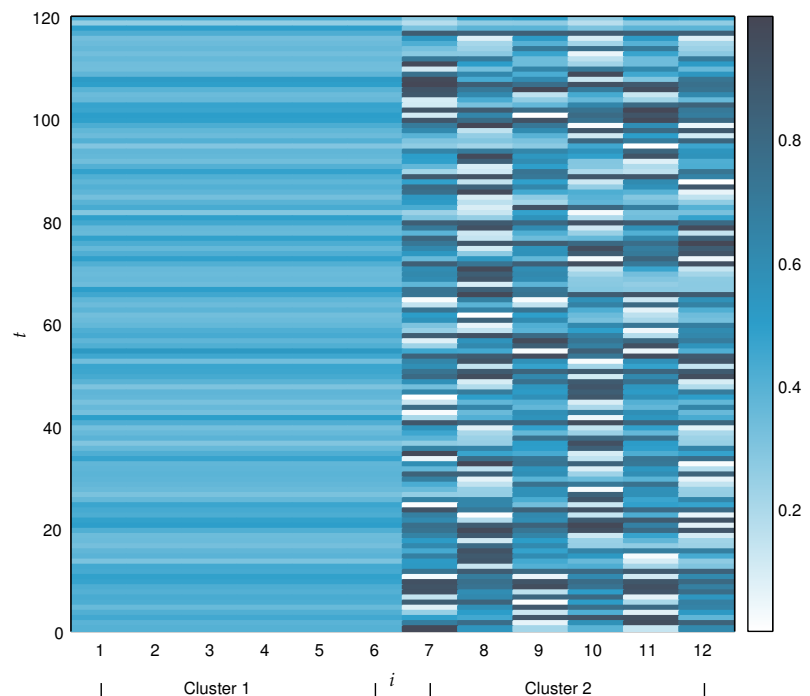
As we have seen, the SMI is well suited for the analysis of cluster synchronization and can be used for intermittent synchronization in which the dynamics change slowly compared to the number of samples. Compared to approaches such as the still widespread synchronization error [Zha20; Ant17] the SMI can identify generalized synchronization and thus allow one to identify more complex synchronization patterns.

We will later study the application of the SMI as a measure for intermittent synchronization in more detail in Section 5.2.

### 4.4 Chimera States

In [Kuro2; Abro4] it was found that specific configurations allow the observation of coherent and incoherent states in the same state. Chimera states are a special case of partial synchronization, where a system experiences a synchronized and incoherent cluster within the same state. An example of such a state is given in Figure 4.3. We

Figure 4.3: Example for a system in a Chimera state. The plot shows the color-coded values for each oscillator  $i$  at time  $t$ . Oscillators  $i \in [1, 6]$  are synchronized with each other while the others ( $i \in [7, 12]$ ) are in an incoherent state. While all oscillators are coupled with each other, the coupling is done in a way where the system can transition into a state where synchronization is only observed within a cluster of the system. The coupling scheme is explained in Section 4.4.1, the plot was derived from the dynamics given in Equation (4.7) for parameters  $r = 2.45$  and  $\kappa = 1.75$ .



see that one half (Cluster 2) of the system experiences full synchronization, while the other half remains incoherent. This was achieved

by following coupling rules described in [Zha21] and which we will explain in more detail in Section 4.4.1.

When scanning parameters, we often find chimera states between a fully synchronized and incoherent regimes. This led to some earlier work, assuming that chimera states are intermediate states of a not-yet synchronized system (see [Wol11]) and it was later shown that it is indeed possible to observe stable chimera states [Cho17; Zha21].

One crucial tool in showing the stability of the chimera state was the Lyapunov exponent, showing that for certain configurations only one of the clusters would show stable synchronization.

As with any other application of the Lyapunov exponent, it works best when the dynamic equations are known, and even then its derivation is not always as forward as the many papers on its derivation show [Wol11; Har19; Zha20].

#### 4.4.1 Method

To construct the chimera states, we follow the proposed method in [Zha21] giving general advice on the construction of coupling schemes for the creation of stable chimera states with regular and non-linear oscillators. We use the proposed method with the now well-known logistic map. We choose a similar coupling as applied in Equation (4.5) where we mostly flip the sign of  $\sigma$

$$x_i[t+1] = \left( rf(x_i[t]) - \kappa \sum_j L_{ij} f(x_j[t]) \right) \bmod 1. \quad (4.7)$$

The authors in [Zha21] propose a setup with two clusters where within each cluster the components can be coupled diffusely while they all see the same field of the second cluster. The coupling scheme encoded in  $L_{ij}$  is visualized in Figure 4.4. The system consists of two clusters with  $i \in [1,6]$  and  $i \in [7,12]$  with next neighbor coupling within each cluster and  $L_{ij} = 1$  and  $L_{ij} = c$  for coupling between the components of a cluster.

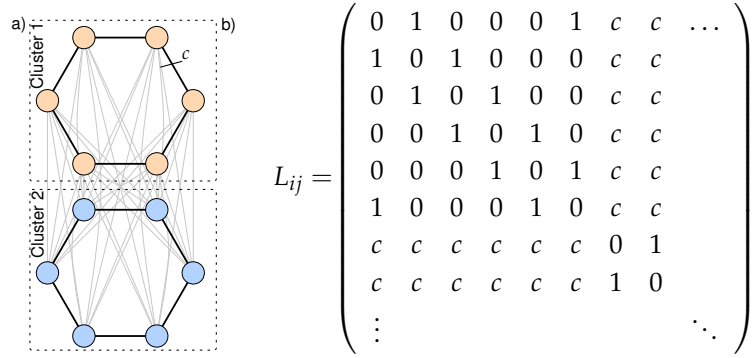
As a result, within a cluster, each oscillator sees the same field from the other cluster and we can write

$$x_i[t+1] = \left( rf(x_i[t]) - \kappa \sum_{j \in G(i)} L_{ij} f(x_j[t]) - \kappa I_{\bar{G}(i)}(t) \right) \bmod 1 \quad (4.8)$$

with  $G(i)$  all elements of the cluster and  $\bar{G}(i)$  all elements of the remaining cluster and  $I_{\bar{G}(i)}(t) = \sum_{j \in \bar{G}(i)} L_{ij} f(x_j[t])$  the mean-field of the other cluster.

For our simulations, we allowed for an equalization time of 10000 steps prior to a recording of the next 120 steps, which we then use for our analysis.

Figure 4.4: Diffuse cluster connection as proposed by [Zha21]. Within each cluster, the oscillators are only coupled to their nearest neighbors. At the same time, each oscillator couples to the mean-field of the cluster of which it is not a part. In a) we show a diagram of this scheme for 6 oscillators in each cluster. A slice of the corresponding coupling matrix  $L_{ij}$  is given in b). In this matrix, the next-neighbor connections have a strength of 1, while the coupling to the mean-field is given by a parameter  $c$ .



#### 4.4.2 Identification of Chimera States

In [Har19; Zha20] the authors derived the Largest Transversal Lyapunov Exponent (LTLE) for one dimensional maps coupled via a matrix  $L_{ij}$  that can be decomposed into its eigenvalues  $v_k$ . The LTLE is given by

$$\text{LTLE}(L) = \max_{2 \leq k} \left[ \lim_{T \rightarrow \infty} \frac{1}{T} \sum_t^T |f'(x_i[t]) - \kappa v_k f'(x_i[t])| \right] \quad (4.9)$$

where  $v_k$  are the sorted eigenvalues of  $L$ .

The LTLE is derived by inserting  $x_i[t]$  obtained for a the simulation of a parameter into the LTLE together with the coupling strength  $\kappa$  and the decomposition of the eigenvalues of  $L$ .

By calculating the LTLE separately for each cluster, we can evaluate the stability of synchronization for each. Chimera states occur when only one LTLE of the two clusters is positive.

For comparison, we calculate the MSMI and ASMI for the same simulated  $x_i[t]$ . The results for the LTLE, MSMI and ASMI are shown in Section 4.4.2 for  $\kappa \in [0, 1]$  and  $r \in [3.7, 4]$ , so that the self-feedback coupling  $r$  ensures chaotic trajectories in the uncoupled case ( $\kappa = 0$ ).

In Section 4.4.2 a) we highlight all areas where the LTLE of only one cluster is positive, Section 4.4.2 b) shows the MSMI, Section 4.4.2 c) the ASMI and Section 4.4.2 d) areas where the ASMI  $< 0.8$  and the MSMI  $> 0.95$ , which we chose as a threshold for chimera states.

Comparing Section 4.4.2 a) and Section 4.4.2 d) we find that indeed the ASMI in combination with the MSMI serves as a good indicator for partial synchronization. Looking at the differences between the LTLE and MSMI based method, some chimera states go undetected when they are created by the finite precision of the simulation. This view is supported in [Zho98] where the authors argue that the LTLE can predict asynchronous systems which then, in the simulation, show as stable synchronous areas when the perturbations are so small that they are lost in the finite precision of the floating point numbers.

A manual check showed that this was indeed the case for the right stripe in Section 4.4.2 d). The differences between the LTLE and the ASMI/MSMI method in the left stripe was in many cases an almost

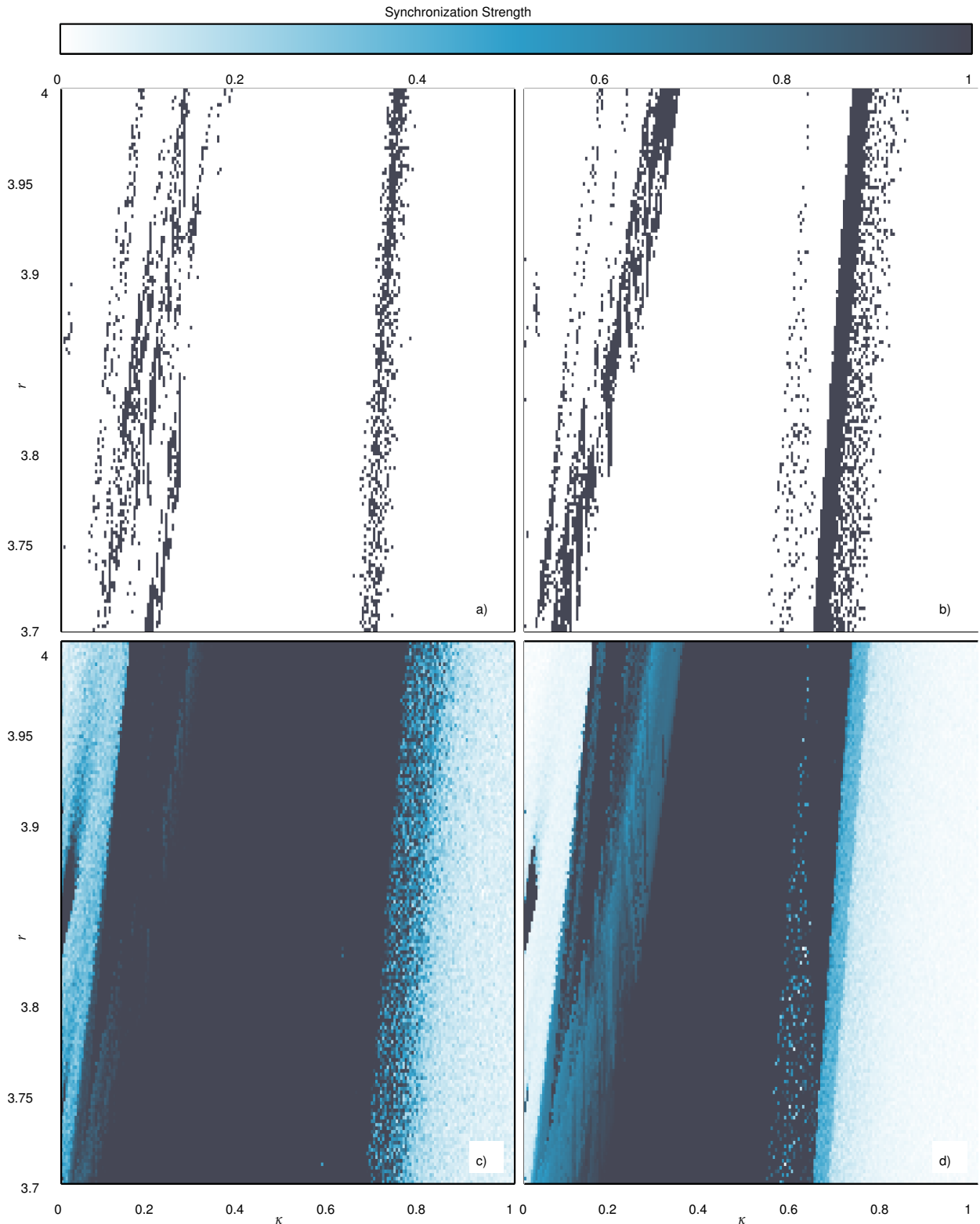


Figure 4.5: SMI based methods can provide good approximations when searching for chimera states compared to the LTLE, however, false positive results are more likely. We compare the results of the LTLE (see Equation (4.9)) with the SMI as a tool for detecting chimera states by scanning the parameter range for  $r$  and  $\kappa$  for Equation (4.7). Each plot a) to d) shows the result for a pair of parameters  $r$  and  $\kappa$ . The LTLE is shown in a) as a reference for our SMI based method. Highlighted are the parameter pairs where the LTLE of only one cluster is positive. In b) we highlight pairs where the  $ASMI < 0.8$  and  $MSMI > 0.95$ . We argue that these are areas where chimera states are likely. A high  $MSMI$  indicates that there are synchronized coupling partners, while a low  $ASMI$  indicates that there is no synchronization between all coupling partners. In c) and d) we present  $ASMI$  and  $MSMI$  to see how the values in b) are created. The method in b) can be a good approximation to the results obtained with the LTLE, but our method identifies more systems as being in a chimera state. We see two possible explanations for this. First, according to [Zho98], synchronization can occur in simulations where the LTLE is greater than 0 due to the finite resolution of floating point numbers. These systems would be identified as synchronous by our method since it is based on the computed system. Second, with the finite precision of SMI estimation, it may be impossible to find thresholds that are sensitive enough to detect chimera states while avoiding false positives altogether.

synchronous system where some spurious synchronization between only two components was detected by the MSMI.

We want to emphasize the fact that the MSMI and ASMI chimera detection methods did not require prior knowledge of the clusters, but still produced good results. This is in contrast to the LTLE based method, where for the analysis the clusters have to be known.

Assuming the same information as available for the LTLE, we show a different plot in Figure 4.6 where we compare a cluster wise ASMI and LTLE with the MSMI and ASMI as a function of  $\kappa$  for  $r = 3.9$ .

Figure 4.6: SMI based methods can be a viable alternative to the LTLE to detect chimera states. This plot compares the detection capabilities for chimera states in a slice of the values presented in Section 4.4.2 ( $r = 3.9$ ). Chimera states are found for parameters where the LTLE of one cluster is positive and the LTLE of the second cluster remains negative (highlighted by a gray background). In a) the ASMI is compared with the MSMI, indicating that regions where the MSMI  $\approx 1$  and the ASMI  $< 1$  are chimera states. In b) we compare the ASMI of each cluster alone. It shows that the MSMI in combination with the ASMI can detect chimera states without prior knowledge of the clusters.

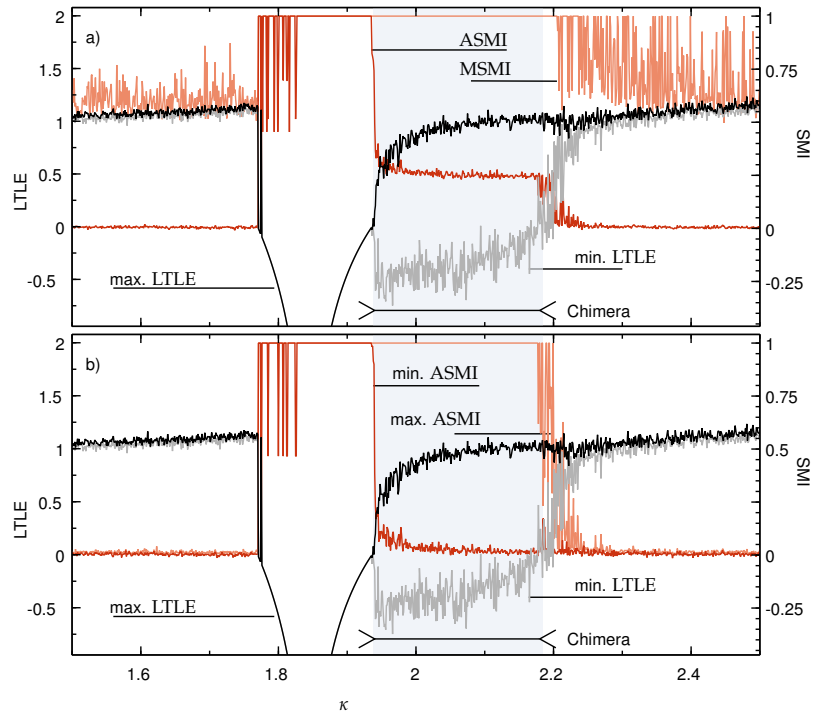


Figure 4.6 a) compare the LTLE directly with the ASMI and MSMI, in Figure 4.6 the minimum and maximum ASMI from both clusters is given for each  $\kappa$ .

Both measures reproduce the values expected from the LTLE with the minimum ASMI dropping when the maximum LTLE becomes positive and both minimum and maximum ASMI dropping with two positive LTLE. Similarly, in Figure 4.6 a) only the ASMI drops with a single positive LTLE. The MSMI continues its high readings until both LTLE readings become positive and then start to show a loss of coherence.

The results show that if the clusters are known from the analysis of the network structure, the SMI can yield results on par with the LTLE while the dynamic equations must not be known. Even without prior knowledge of the coupling, the ASMI in combination with the MSMI can yield meaning full insight into the state of the system. Here, their main competition is IS methods where the SMI shows more



generality.

#### 4.4.3 Delayed Feedback

Much work is dedicated to finding the mechanisms behind the strong chimeras [Zha21; Har19; Cho17; Seto8; Yel14]. In past research, delayed feedback has been shown to stabilize synchronization. While delayed feedback destabilizes synchronization for local coupling, as we have seen already in Figure 3.9 and in [Ant17; Con18], in global coupling, it can have a stabilizing effect. For regular oscillators, this effect was already described in [Ata04; Seto8], it was later shown in [Seto8] that coupling to a delayed mean-field supports the stable chimera states.

Here we argue that the presence of stable chimera states [Zha21; Cho17] is also a consequence of delayed feedback, hidden in the mean-field of the non-diffusive coupling. As a support of this idea, we show that weak delayed feedback coupling can strengthen the stability of synchronization. In contrast to the work in [Seto8] the components of our system will work in their chaotic regime.

As before, we use the logistic map as a base for our investigation and modify the coupling scheme of Equation (4.7) to observe only one cluster and add a delayed global coupling

$$x_i[t+1] = \left( r l(x_i[t]) + \kappa \sum_j L_{ij} l(x_j[t]) + \chi \sum_j l(x_j[t-1]) \right) \bmod 1 \quad (4.10)$$

where  $\chi$  is the coupling strength and  $L_{ij}$  the entries of a coupling matrix for a next neighbor coupling.

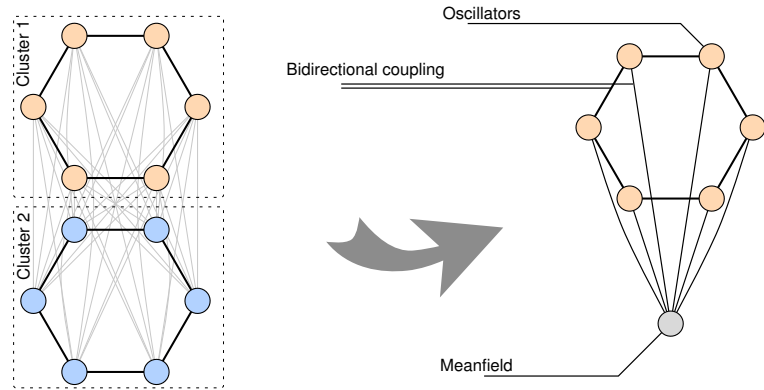
In Figure 4.7 we show the transition of the two clusters proposed in [Zha21] to the mean-field, we assume. For all components of one cluster the field they see from the other cluster is the same, they effectively see a mean-field which we show in Figure 4.7 b). This was already recognized by [Zha21] by introducing  $I$  in Equation (4.8).

We further argue that the volatility of single components is suppressed in the mean-field and thus the effect of self feedback stronger pronounced. In our simplification, this results in step Figure 4.7 c) where we replace the coupling to the mean-field with a global delayed self-feedback.

As the incoherence in the opposing cluster is less pronounced for the first cluster, this incoherence also has a decreased destabilizing effect on the synchronous cluster. The asynchronous cluster, meanwhile, does not profit from the increased coherence in the synchronous cluster. Due to the strong coherence in the synchronous cluster, contributions from his own delayed mean-field are indeed to be expected to be small since other values do not cancel out.

In Section 4.4.3 we show the probability  $p$  of a synchronous system

Figure 4.7: Modification of the coupling scheme presented in Figure 4.4. The coupling to the mean-field of the second cluster is replaced by the mean-field of the same cluster from a previous step. This approach allows us to isolate the self-feedback of clusters.



resulting from 200 samples. For random initial values, the system proposed in Equation (4.10) is simulated, and the SMI is calculated for a length of 1000 values. Each system with an  $\text{SMI} > 0.95$  is considered synchronous. The system is sampled for parameters  $\kappa \in [0, 2.2]$  and  $\chi \in [-0.2, 0.4]$ .

As we can see from Section 4.4.3 the delayed feedback of the global mean-field increases the stability of synchronization for subtractive coupling. The effect is strongest in the area of very weak delayed coupling. In the early example of Equation (4.7)  $c$  was chosen to be 0.2, assuming, as discussed earlier, that the contributions from the single elements in the incoherent cluster cancel out, this results in an effective coupling strength with the delayed feedback of  $c \cdot c = 0.04$  (coupling of the second cluster to the first and the coupling back in the next step).

We have marked the 0.04 line in Section 4.4.3. It shows that in this area the effect of the delay feedback on the size of the synchronous regime is quite pronounced.

But why does it only work for one of the clusters? Well, as we have mentioned before, we see chimera states in between synchronized and incoherent regimes. While one cluster might find synchronization, the other one might have the wrong starting parameters. Also, as we argued earlier, the mean-field seen by a cluster averages out the decoherence of a field, which results in dynamics dominated by the feedback. In a synchronized cluster, especially with IS, the dynamics are dominated by the cluster components (at least for non-flat trajectories), and decoherent cluster has less strong coupling to its old state.

## 4.5 Nondeterministic Synchronization

In all previous examples, we considered pure deterministic systems. In practice, most systems will experience some kind of uncorrelated external noise. The effect of noise on synchronization and partial

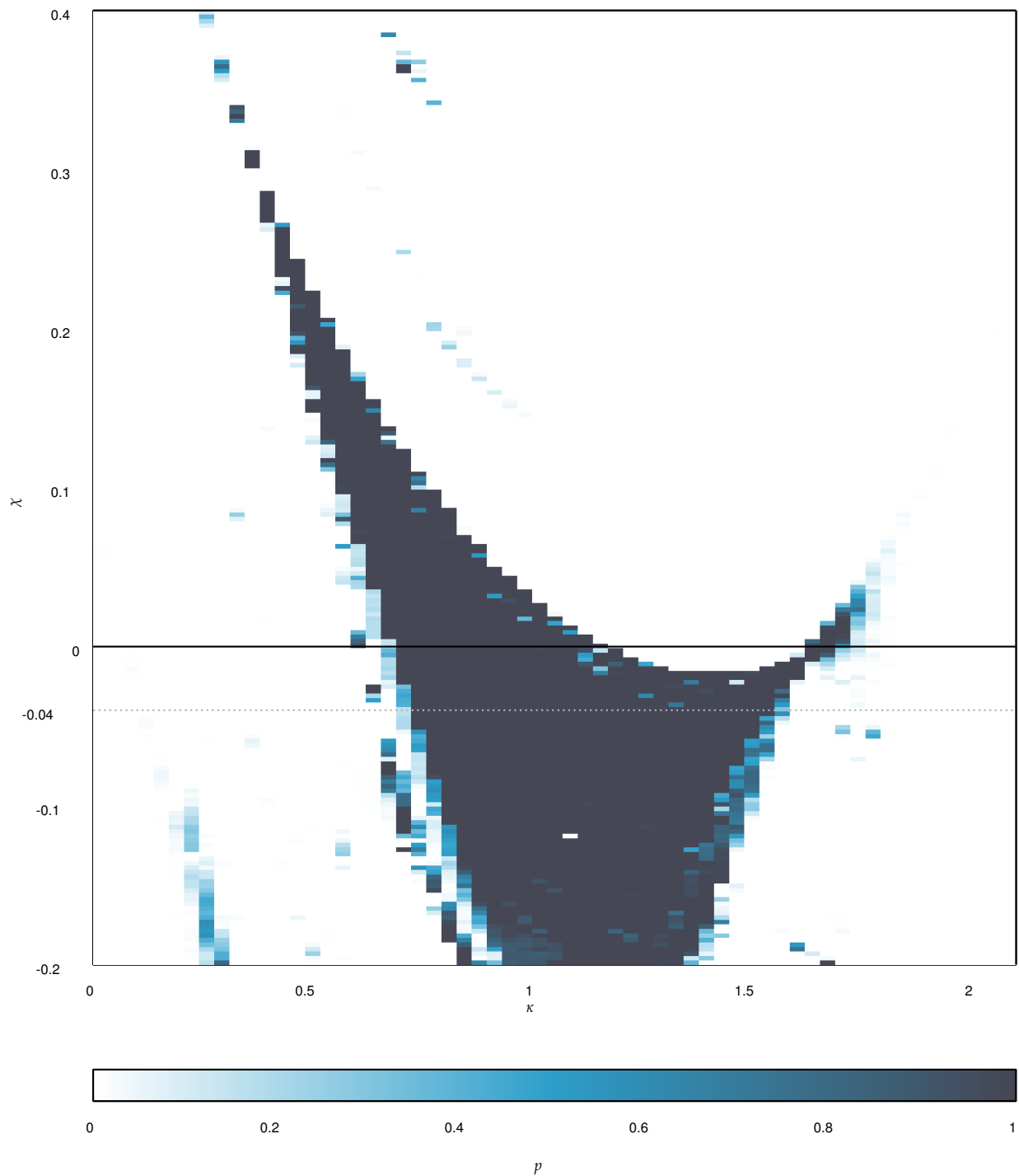
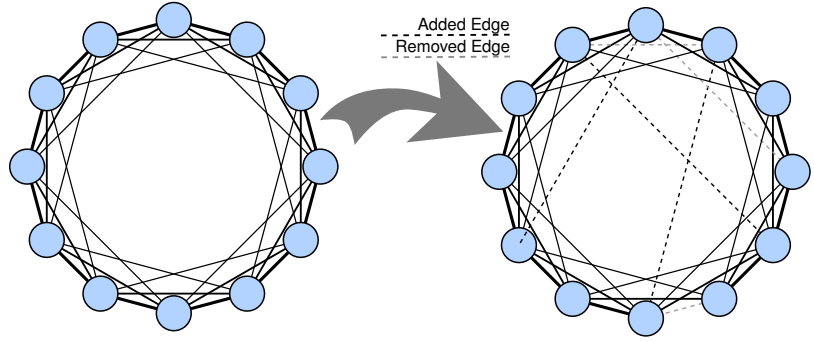


Figure 4.8: Low levels of negative self-feedback can increase the size of the synchronized regime. Probability  $p$  of observing a synchronous state for the parameters  $\kappa$  and  $\chi$ . Each point is sampled for 200 different initial conditions. The plot shows that coupling to the delayed mean-field increases the stability of coupling, especially for a negative coupling. We see that the introduction of some negative delayed feedback (e.g.  $\chi = -0.04$ ) yields a larger stable parameter range for  $\kappa$  than for no ( $\chi = 0$ ) or positive values.

Figure 4.9: By rewiring random connections between single components the Watts & Strogatz algorithm creates a small world network from a  $n$ -next-neighbor network [Wat98].



synchronization has been the focus of research in recent years.

In [Zhazo] the authors find that the synchronous cluster in the chimera state can switch for even comparatively small levels of noise. Here, we examine the synchronization of logistic maps with added noise. In [Kat20] a framework is introduced to describe the synchronization of noisy coupled chaotic oscillators. Early work found that synchronization can be induced with correlated noise terms [Pik84; Zho02; Tero4], recent research even suggests that uncorrelated noise can enable synchronization [Men18].

#### 4.5.1 Methods

We use a system similar to Section 4.1 and Section 4.4, adding a term for uncorrelated noise. We derive an equation

$$x_i[t+1] = \left( rf(x_i[t]) + \kappa \sum_j L_{ij} f(x_j[t]) + u\zeta_i \right) \bmod 1 \quad (4.11)$$

where  $L_{ij}$  are elements of the connection matrix  $L$ . The noise  $\zeta_i$  is generated from a uniform distribution with  $\zeta_i \in [0, 1[$  and without temporal or spatial correlation, its strength is regulated by  $u$ .

We want to study the effects of noise on different types of networks and thus propose different types of networks. This includes a small world network with 200 maps  $L_{200}^S$  and 800 components  $L_{800}^S$ , a globally coupled (all-to-all) system with 50 maps  $L_{50}^G$ , and an 8-next-neighbors network with 200 components  $L_{200}^8$ .

The small-world network is created by the Watts & Strogatz algorithm [Wat98] with a rewiring probability of 0.05. An example of such a small-world network can be seen in Figure 4.9.

#### 4.5.2 Results

We performed a fine-grained analysis for parameters  $\kappa \in [0, 1]$  and coupling to noise  $u \in [0, 0.1]$ . For each set of parameters, we calculate

the ASMI as defined in (Equation (3.14)). The results are shown as a heatmap in Figure 4.10.

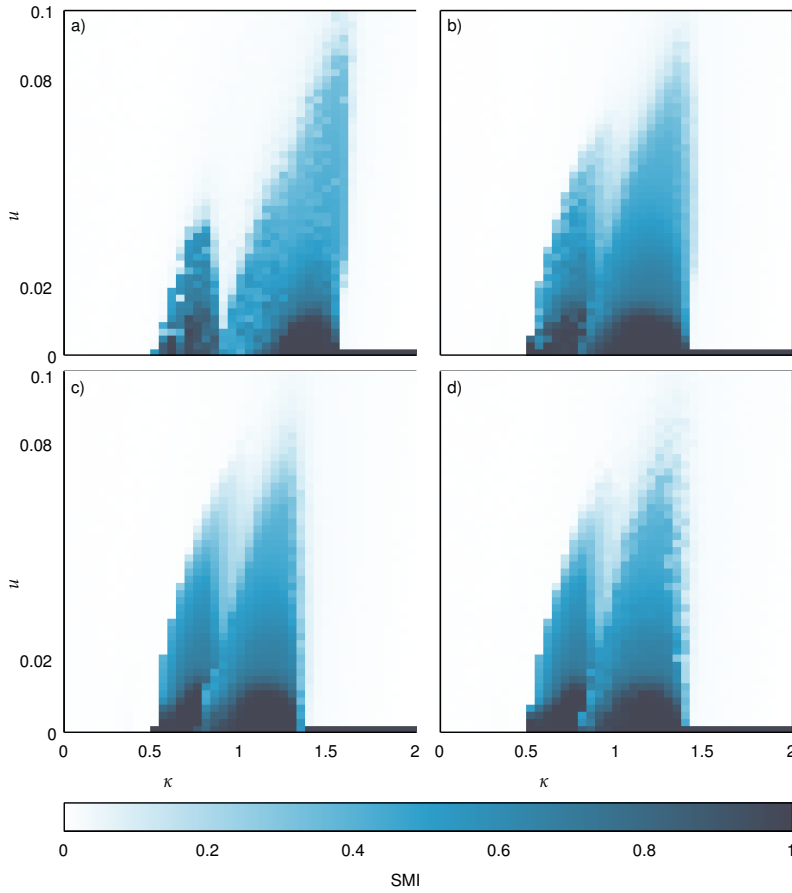


Figure 4.10: We can not see any difference in resilience to noise for different network types in our work, however, we observe that low levels of noise can introduce stable synchronization. Stability of different types of networks against the injection of noise  $u$  into the coupling. For each network the coupling strength  $\kappa$  is varied. The plots a) show a next-neighbor network, b) the next 8 neighbors, c) a Watts-Strogatz network with a rewiring probability of 0.05, and d) the same, but with a size of 800. The robustness of the network to noise is measured with the ASMI.

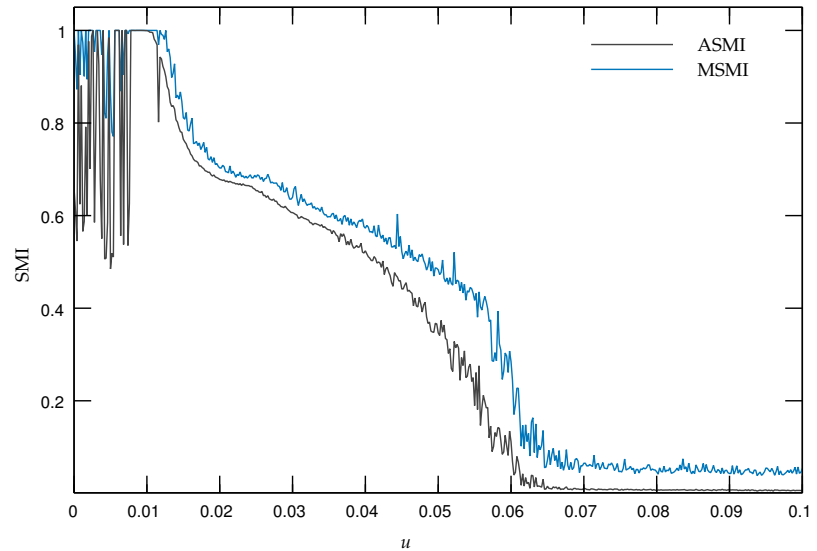
As expected, we observe a general decline in synchronization with induced noise. For all maps, we see that full synchronization is strongest in the center of each synchronous regime, however, higher coupling strength  $\kappa$  often proves to be more resilient to larger noise.

In some of the networks synchronization that initially decayed with increasing noise recovers before it fades off. This can be seen in the right flanks of Figure 4.10 a) and b). While this is similar to the results in [Men18], where the authors see an increase in synchronization stability with noise injection, our results are inconclusive in this regard. Recovery from decoherence is limited to parameters  $\kappa$ , where synchronization occurs already without noise and is preceded by a complete loss of synchronization.

We will take a closer look at noise-stabilized synchronization for the  $L_{200}^S$  system. The region for  $\kappa = 0.8$  has been sampled as a function of the noise coupling  $u$ . The results are shown in Figure 4.11. We see that the synchronization is stable for small noise levels. For  $u \approx 0.01$ , we can see a small plateau before the system enters a decoherent state.

To avoid spurious correlation, we have sampled the SMI for each

Figure 4.11: Low levels of noise can stabilize synchronization. The plot shows the ASMI and MSMI for different noise levels  $\mu$ . For a small noise regime, the systems synchronize reliably. The plot is generated from Equation (4.11) for  $\kappa = 0.8$  as a function of the noise coupling  $\mu$ .



point 1000 times and plotted the mean of these samples along with the variance. For comparison, we also calculated the SMI for each point with the shuffled time series. We see that this increase of the SMI is well reproducible and also well above the SMI produced by uncorrelated series.

### 4.5.3 Discussion

We have seen the effect of noise on different types of networks of coupled logistic maps. We found that the simulated systems were resilient to noise even for values much higher than the precision of the floating point numbers used for the simulation. This is in contrast to effects such as switching chimera states in [Zha20] where the authors found that noise in the limit of their resolution would induce switching of the synchronous cluster.

We could also see that the resilience to noise was strongest for coupling parameters well away from the borders of the synchronous regime, however, partial synchronization ( $ASMI < 1$ ) proved to be persistent for higher coupling values, possibly due to its overall smaller contribution.

The results on a stability-inducing effect of noise were inconclusive, taken from [Men18]. We saw in Figure 4.11 that synchronization can persist in the presence of noise. However, only weak evidence for the synchronization-inducing effect was found in Figure 4.10.

Once again, SMI has shown its versatile applicability. While the LTLE was used in [Zha20] to study the switching of chimera states with noise, its application for non-deterministic systems is limited and also based on Monte-Carlo sampling.

# Synchronization in Real-World Systems

In previous chapters, we used the SMI in combination with computational experiments, testing its sensitivity and limitations in well-known systems and comparing it with other results. We will now apply the SMI on real-world data and to passive experiments.

This implies two major changes in our application. First, the system is effectively a black box for us. We are only able to observe a subset of the phase space that drives the system. This also means that we control none or only a few of the parameters that govern the dynamics of the system. Even where we control some parameters of the experiment, these are expensive, and thus only a limited number of different parameters can be tested.

The second change is the introduction of noise. While in our toy systems noise (introduced by finite floating point errors, for example) was of no concern, we will now expect it as a part of the dynamics as well as in the recording of our data.

In contrast to the toy models in Chapter 3 we also have to drop the expectation of full synchronization. As we have already seen in Chapter 4 the systems will experience a decrease in correlation when perturbed by uncorrelated noise. Certain network structures will experience some intermediate states between fully synchronized and incoherent systems (see, e.g., chimera states in Section 4.4).

In this chapter, we study the correlations of stock indices listed in the Dow Jones. We will compare the results of the SMI with a similar measure based on MI in creating a distance matrix between the return of the respective stock quotes.

Furthermore, we apply the SMI on action potential recordings from the development of neurons from mice hippocampus. We evaluate recordings of single-neuron action potentials that align with each other during growth over several days.

## 5.1 Synchronization in Stock Markets

Economic networks are complex dynamical systems. A large number of agents competing in the market are governed by feedback loops, and delay with imperfect knowledge poses an interesting challenge to our understanding. Therefore, and for the possible earnings, a huge body of research is dedicated to the analysis and description of market dynamics.

A central concept for the price of the stock market is the Efficient Market Hypothesis (EMH). It claims that a stock price reflects all the knowledge available to agents in a market. Any new information will be immediately integrated into the price [Fam70; Malo3].

Based on methods from complexity theory, various studies used historical stock prices to analyze correlations between companies in the markets [Are08; Per11]. The idea behind these approaches is that the market price reflects the underlying state in a phase space—the information available to the market, in terms of the EMH. Another approach tries to reconstruct this phase space [Zha13; Guo19] in order to predict the markets.

We will leave the reflection on these approaches to their respective peers and focus ourselves on the exploration of the historical data. Although the EMH predicts that (without insider trading) no agent can outperform long-term market growth, it does not prohibit correlation between prices. When agents in a market obtain new information, the price of stocks quickly reflect this. Where new information concerns more than one stock, their historical data will show at least local synchronization.

We will use the SMI to analyze the synchronization between the Dow Jones listed stocks over the past 20 years. Due to its technical similarity, we compare the results to a second MI-based measure and show the Minimum Spanning Tree for both results. This approach is similar to previous methods that exploited correlations between stock indices to create networks and minimum spanning trees (MST) [Man99].

The strength of synchronization is considered a candidate for crisis prediction, as some studies found that economic crises are often preceded by increases in the general synchronization between companies [Per11].

A methodically similar work was published in [Wis23] where the authors used MI with a different normalization to study the information flow between companies. However, this work was not carried out under the notion of synchronization. Due to its similarity in implementation, we will compare the results with our own method.



### 5.1.1 Normalized Mutual Information

Many common approaches to searching for correlations use methods such as Pearson's or Spearman rank correlation. Entropy and MI are interesting alternatives since they are also able to identify non-linear correlations. In a previous attempt at non-linear correlation analysis on stock markets, the authors in [Guo18] also used the MI and a maximum normalization with entropy. In [Guo18] an MI-based measure was proposed to measure statistical correlations between stock indices. Similarly to the MI-based synchronization measure SMI, the method is based upon a normalization of the MI. The proposed measure is defined as [Guo18]

$$\text{NMI}(X, Y) = \frac{2I(X; Y)}{H(X) + H(Y)}. \quad (5.1)$$

We have seen in Equation (2.13) that  $I(X, Y)$  is smaller than  $H(X)$  and  $H(Y)$  each, so that NMI can only be 1 if  $H(X) = H(Y)$ .

The authors were able to show that  $1 - \text{NMI}$  meets all the requirements of a metric. The same is not true for SMI, where  $1 - \text{SMI}(X, Y)$  may even vanish for  $H(X) \neq H(Y)$ , violating one of the requirements for a metric

$$m(X, Y) = 0 \Rightarrow p(X) = p(Y). \quad (5.2)$$

### 5.1.2 Method

To analyze the stock market, we construct a graph with each company as a node. Synchronization with other companies gives the strength of the edges between the nodes. We generate the adjacency matrix of this graph by calculating the distance matrix for all pairs of shares. This distance matrix  $D^{\text{SMI}}$  is given by the components

$$D_{ij}^{\text{SMI}} = \text{SMI}(X_i, X_j). \quad (5.3)$$

We immediately see that the adjacency matrix is symmetric (and therefore the graph is undirected) and also positive.

To make the information contained in  $D^{\text{SMI}}$  more accessible, we use the minimum spanning tree (MST) [Kru56] to extract the vital relationships for each company. (Technically, we use the maximum spanning tree, since the synchronization is highest for  $\text{SMI} = 1$ .) With the MST we build a hierarchy of relations between the companies by removing edges with low synchronization. Removing uninteresting edges allows us to identify clusters by eyesight. In conclusion, the MST shows a graph where all nodes are connected without cycles while minimizing the total edge weight.

### 5.1.3 Time Invariance of the Structure

The SMI for each pair of companies is estimated over a set of daily stock prices. In doing so, we assume that the price of each day represents values of the same distribution. However, over 20 years, it is

not clear that this assumption is valid. For example, while the two companies MMM and Boeing generally show some correlation, the 2020 Corona crisis had a stronger impact on Boeing.

In [Per11], the authors have shown that the assumption of a time-independent correlation does not hold before an economic crisis. Since we operate on a more coarse resolution, we are not necessarily sensible to these events.

However, we tested the temporal stability of the SMI by looking at subsets of the historical data. Each time series is divided into four windows of equal length and  $\text{SMI}_W$  is calculated for each window. We then derive a set of entries

$$k \in 1, 2, 3, 4 : D_{ij}^{\text{SMI}_W, k} \quad (5.4)$$

for all companies with the window  $X_i^W$ .

Inevitably, the  $\text{SMI}_W$  will show some variance that can be attributed to the finite sampling size. To distinguish between variance from finite sampling and unstable correlations, we generate a set of surrogate data from the historical data. Although it must have the same sample size as the windowed datasets, the correlations in all datasets should be the same. We generated this surrogate set of data by taking only every fourth value of the historical data. This creates a second data set

$$l \in 1, 2, 3, 4 : D_{ij}^{\text{SMI}_S, l} \quad (5.5)$$

with the  $\text{SMI}_S$  with the *skipped* values  $X_i^S$ .

We then calculate the variance of the  $\text{SMI}_S$  and  $\text{SMI}_W$

$$\sigma_{S/W} = \left[ \sum_{S/W} \sum_i \sum_{j \neq i} \left( \text{SMI}(X_i^{S/W}, X_j^{S/W}) - \overline{\text{SMI}}_{S/W} \right)^2 \right]^{\frac{1}{2}}. \quad (5.6)$$

with the mean

$$\overline{\text{SMI}}_{S/W} = \frac{1}{N} \sum_{S/W} \sum_i \sum_{i \neq j} \text{SMI} \left( X_i^{S/W}, X_j^{S/W} \right) \quad (5.7)$$

and  $N$  is the number of all the terms summed over. In Figure 5.1 we show the variance distribution for  $\sigma_S^2$  and  $\sigma_W^2$ . At first glance, these plots show no visible differences and it seems the variance in the SMI can be attributed to the finite sampling size. We can examine this finding in further detail by comparing candidates for the mean and variance of  $\sigma_{S/W}$  and  $\overline{\text{SMI}}_{S/W}$ . We compare the two distributions following the protocol in [Kru13]. We assume that  $\sigma$  follows a Gamma distribution and with PyMC3, we sample the difference in the parameters of this distribution [Sal16]. The results are shown in Figure 5.2. The assumption, that both distributions originate from the same parameters is well-supported by visual inspection alone. If there is any difference between the parameters of  $X_i^S$  and  $X_i^W$ , they are lost in the resolution of the available data.

While other work shows that the synchronization changes precede major economic events (see [Per11]), we can only assume that these

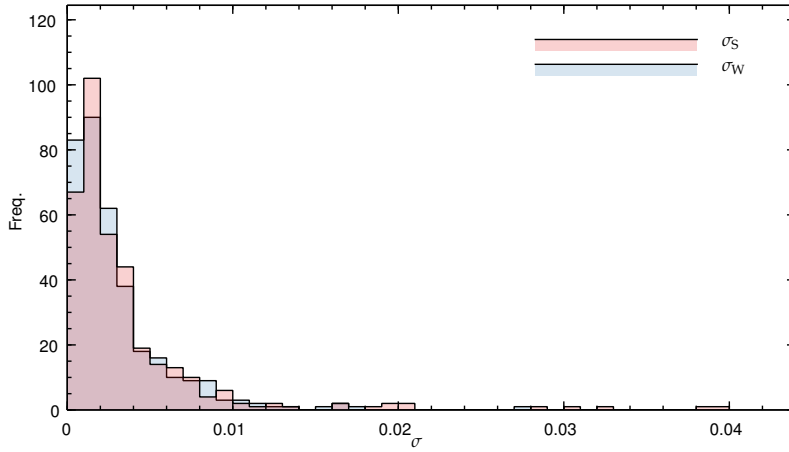


Figure 5.1: We find no evidence of a time-dependent correlation between the stock indices of Dow Jones listed companies. The variance  $\sigma^2$  in the SMI between all pairs of companies in different subsets was calculated. By comparing the distribution of  $\sigma$  of the time-dependent and time-independent subsets, we can test the time series for temporal stability. The time-independent subset is constructed by skipping values  $\sigma_S$ , the time-dependent uses a different set of times  $\sigma_W$ . Importantly, both systems use the same number of samples to compute the SMI. We can recognize a time-dependent system when the distribution of  $\sigma$  in the subsets is different. This plot shows a histogram for all subsets of all time series.

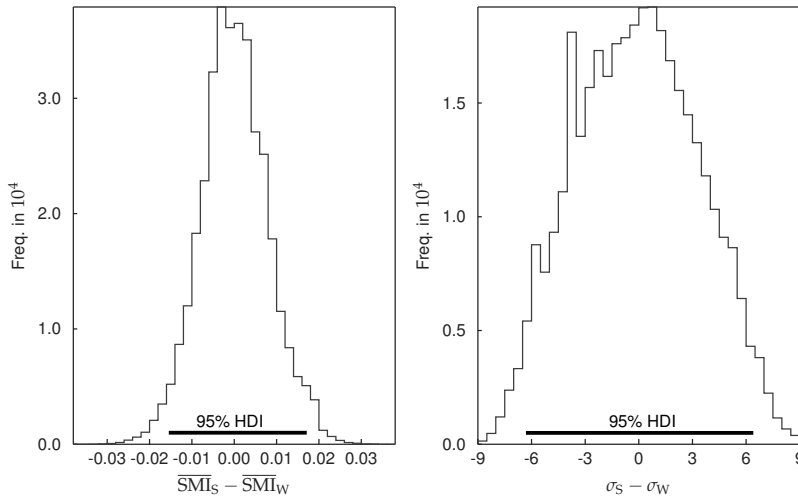


Figure 5.2: Further evidence that our assumption of a time-independent correlation between stock indices is justified. The distribution of the differences between the variance and the mean for  $\text{SMI}_W$  and  $\text{SMI}_S$ . The highest density interval (HDI) contains 0, which is also the center of the distribution.

correlations must quickly relax, affecting the coherence of both timelines only very little over the course of twenty years. Within a time window of a few years, the correlations seem to be stable and our assumption of temporal stability seems to be well-founded.

#### 5.1.4 Results

We analyze historical stock values from companies listed continuously in the DOW Jones index between January 2000 and June 9, 2020. Companies included in the analysis are listed in Table 5.1 together with their abbreviations and a short symbol. The dataset contains a table with daily opening, closing, high and low prices as well as the traded volume for each of the stocks was downloaded from [Yah20].

To calculate the SMI we have to convert the values of the time series of the stock values into symbols. In this analysis, we restrict ourselves to a single symbolization strategy. For a stock  $X^{i,\text{open}}, x_t^{i,\text{open}}$

Table 5.1: Companies continuously listed in the Dow Jones Industrial Average (Dow Jones) from January 2000 to 6th of June 2020. Each company is assigned with an industry which is derived from the Global Industry Classification Standard [Glo18]. For each sector a unique symbol is used as an identifier, shown next to the content. The sectors are: Information Technology (IT), Industrials (IND), Financials (FIN), Consumer Discretionary (COD), Health Care (HLTH), Consumer Staples (COS), Energy (ENG) and Communication Services (COM).

Symbol	Company	Sector	Color Index
IBM	International Business Machines Corporation	IT	◇
CSCO	Cisco Systems, Inc.		
AAPL	Apple Inc.		
INTC	Intel Corporation		
MS	Microsoft Corporation		
V	Visa Inc.		
BA	The Boeing Company	IND	■
MMM	3M		
CAT	Caterpillar Inc.		
UTX	United Technologies Corporation		
GS	The Goldman Sachs Group, Inc.	FIN	○
AXP	American Express Company		
JPM	JPMorgan Chase & Co.		
TRV	The Travelers Companies, Inc.		
MRK	Merck & Co., Inc	HLTH	□
JNJ	Johnson & Johnson		
PFE	Pfizer Inc.		
UNH	UnitedHealth Group Incorporated		
PG	The Procter & Gamble Company	COS	◇
KO	The Coca Cola Company		
WMT	Wallmart Inc.		
WBA	Wallgreens Boots Alliance, Inc		
MCD	McDonald's Corporation	COD	■
HD	The Home Depot, Inc.		
NKE	NIKE, Inc.		
XOM	Exxon Mobil Corporation	ENG	●
CVX	Chevron Corporation		
VZ	Verizon Communications Inc.	COM	◆
DIS	The Walt Disney Company		

are the daily opening values of the stock  $i$ . We will derive the symbols from the relative change

$$\delta x_t^{i,\text{open}} = \log \frac{x_t^{i,\text{open}}}{x_{t-1}^{i,\text{open}}}. \quad (5.8)$$

The symbols are then created by sorting the data into 10 equally distributed bins between the minimum and maximum value of each time series. This generates the symbolized time series  $\tilde{X}^{i,\text{open}}$ . In Section 5.1.5 we compare different methods of symbolization. Here, we restrict ourselves to the above simple binning strategy. We calculate the distance matrix  $D^{\text{SMI}}$  for all stocks  $i$ . Figure 5.3 a) shows the resulting synchronizations for all pairs, ordered by their strength.

To derive the graph of the inter-company synchronizations we calculate the distance matrix  $D^{\text{open}}$  with all pairwise values SMI. Thus, each entry of the distance matrix is given by

$$D_{ij}^{\text{open}} = \text{SMI}(\tilde{X}_i^{\text{open}}, \tilde{X}_j^{\text{open}}) \quad (5.9)$$

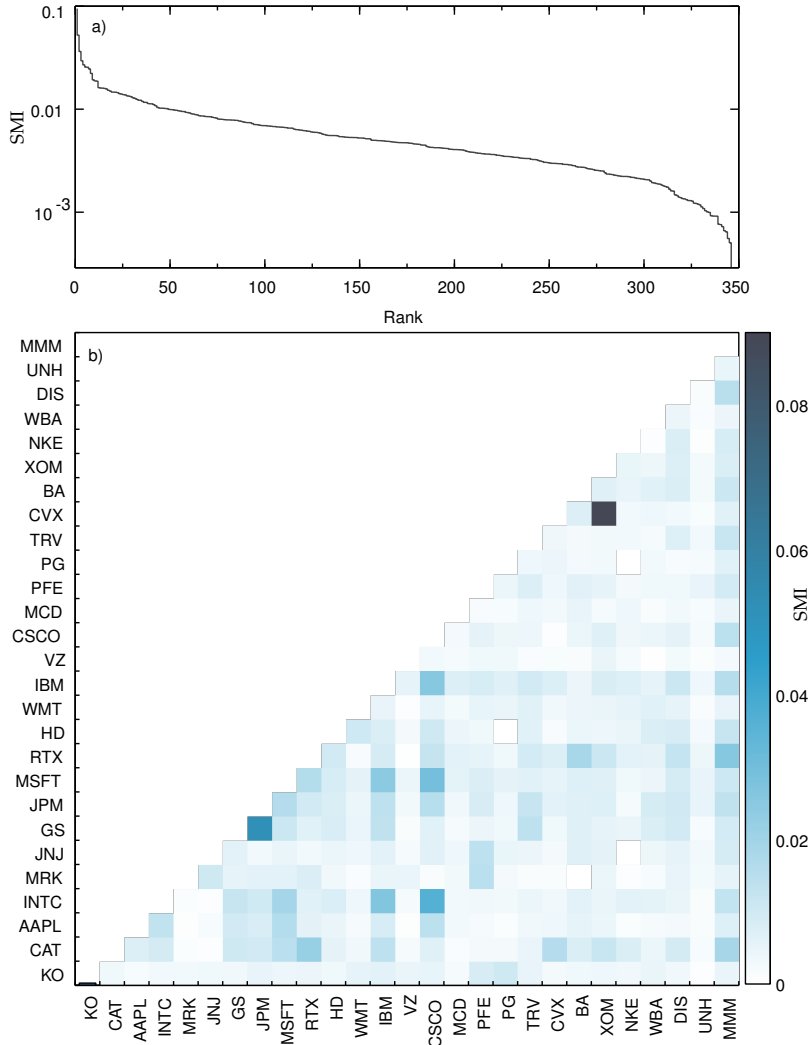


Figure 5.3: There is a significant correlation between the stock prices of many companies, although none of them are synchronized in the way that the models in earlier chapters were. In a), the SMI between all companies is plotted as a function of their rank. In b) we see the matrix of all pairs of SMI between Dow Jones listed companies. For each entry, we computed the SMI, but only plotted those instances where the value was significant. Pairs were considered significant if their z-score (Equation (5.10)) was greater than 100. Since the SMI is symmetric, only one instance of each pair is shown. A list of all companies and the abbreviations used are given in Table 5.1.

To prevent the detection of false synchronization via spurious correlation, we test each entry  $D_{ij}^{\text{open}}$  for its statistical significance. The significance is calculated from surrogate time series created from shuffling the original data. For each pair, 1000 surrogate SMI values are calculated from multiple shuffles. [The92]

By design, these time series do not show any temporal correlation which allows us to estimate the "ground noise" of spurious synchronization. With the mean  $\mu(\cdot)$  and variance  $\sigma^2(\cdot)$  of the surrogate data, the z-score is computed as

$$z(X_i, X_j) = \frac{\text{SMI}(X; Y) - \mu(A^{X_i, X_j})}{\sigma(A^{X_i, X_j})}. \tag{5.10}$$

Entries with z-scores lower than 100 are rejected.

The resulting matrix  $D^{\text{open}}$  is shown in Figure 5.3. A first glance at the matrix shows two pairs with increased synchronization. The highest synchronization is achieved by Goldman Sachs with JP Morgan and Chevron with Exxon. These findings are by itself of little surprise but show that the method is capable of capturing dependen-

cies between companies. Chevron and Exxon are widely expected to be influenced by the current oil price and any projection of it on future markets.

JP Morgan and Goldman Sachs both provide major funds and, thus, are driven by the general health of the financial markets. The general small values of the SMI might initially seem concerning. However, we have to remember that these values are derived for systems that we expect to be driven by noise and possibly a projection from a higher dimension. The conservative limit that we applied to the z-score shows that these values are not generated by spurious correlations but are features of the time series.

With increased confidence in the temporal stability of the SMI we will apply some further analysis on the coarse structures in the graph  $D^{\text{open}}$ . The MST is computed for  $D^{\text{open}}$  as described in Section 5.1.2. The result is shown in Figure 5.4. Companies are color-coded by the sector of businesses they are active in. The company classifications together with the color coding are found in Table 5.1.

As we can see, the sections of commerce of each company are reproduced by the SMI. Companies for industrial products show strong synchronization with each other and are, as a group, connected to energy companies. Since IT companies are the backbone of any operation, it seems surprising that this cluster is not directly connected to the health and consumer-related companies.

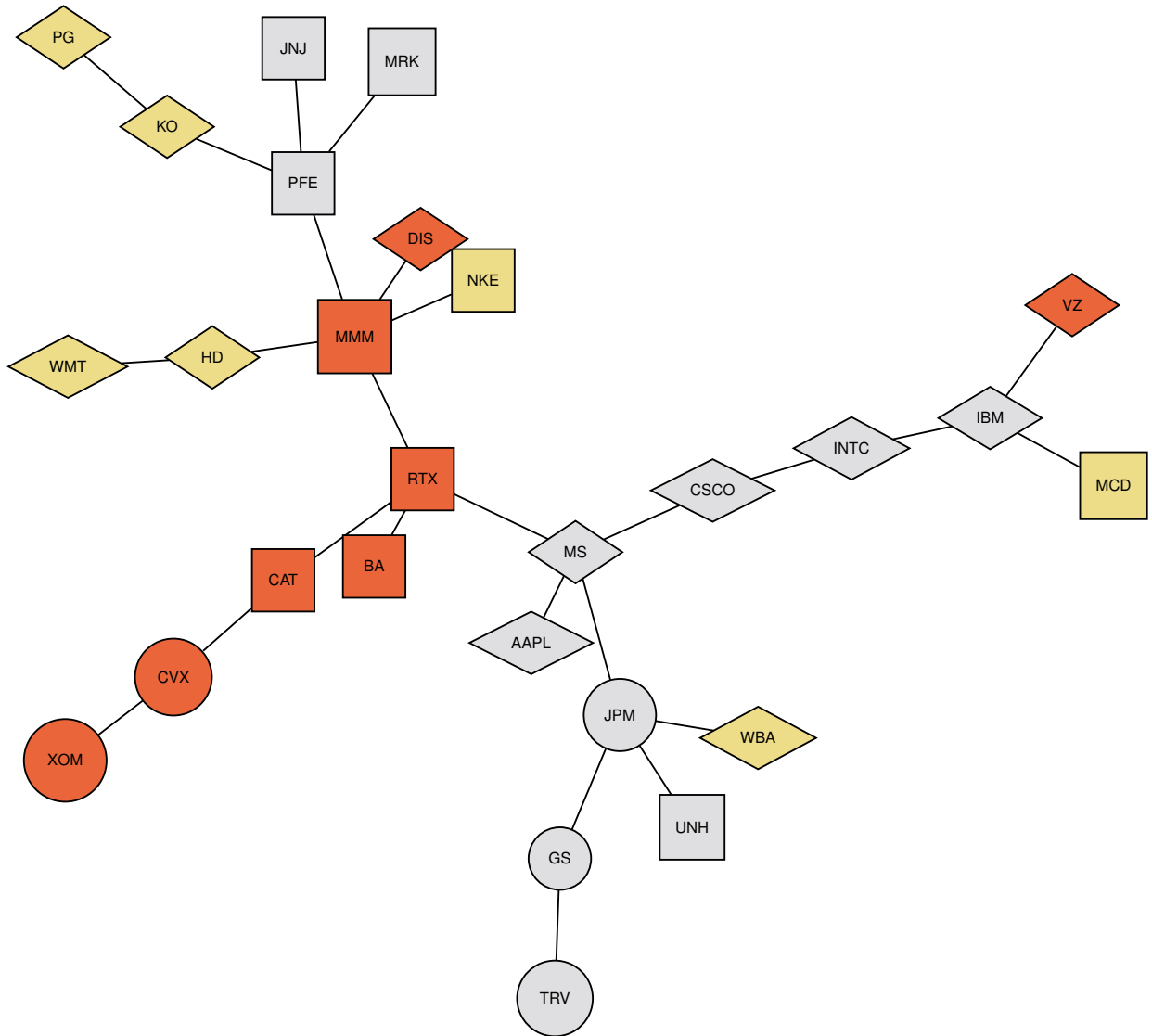


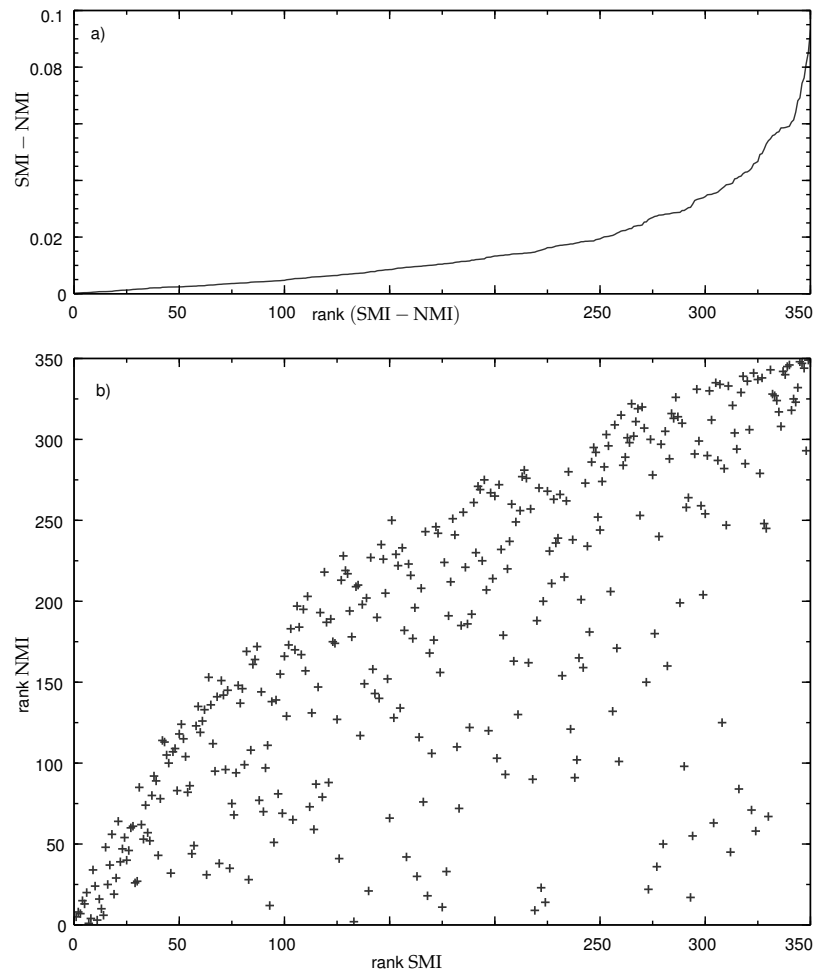
Figure 5.4: The minimum spanning tree is able to replicate the distinction between different industry types of Dow Jones listed companies. The minimum spanning tree is constructed on the inverse of the SMI between a pair of companies and could be more accurately described as a maximum spanning tree. The types of industries assigned to each industry are taken from [Glo18]. The colors represent companies in different types of industry. A list of all companies, their abbreviations, and their industries can be found in Table 5.1.

## 5.1.5 Discussion

Figure 5.4 shows the SMI based synchronization for Dow Jones listed companies, estimated daily open values between January 2000 and June 2020. In most cases, the synchronization between companies reflects their sector as given in [Glo18].

To compare our results to existing methods, we have also calculated the distance matrix  $D$  using the NMI (see Equation (5.1)). In Figure 5.5 we show the absolute differences between SMI and NMI as well as a plot of the projection of the rank for each index calculated by the SMI and NMI.

Figure 5.5: The SMI is not a monotonic projection of the NMI. Both measures are calculated between the stock prices of each company. In a) we see the difference between the two measures for the same pair of companies, sorted from smallest to largest. For b), we computed and assigned a rank to each value. Then, for each company, the rank of the SMI and NMI is plotted.



As with all correlation measurements, we should not forget that increased synchronization does not imply any causation between the companies. Correlations can also arise from third-party drivers or mutual effects. There exist methods for finding common causes in correlation, for example [Koř20; Run19; Run12]. These methods use multivariate MI and conditional MI to find common sources for single events. For economical data, finding well-sampled distributions that can be matched with historical data of stock values is much harder.



## 5.2 Synchronization of Neuronal Systems

Neuronal oscillation can be observed as a regular electric field, measurable even outside the brain. They come in different bands and are a consequence of the summed potential of simultaneously firing neurons [Baş13; Gue17]. Chimera states have been studied in the context of brain patterns in [Wan20; Maj19; Ban19; Bro10], other studies explore the stability of chimera state with *in silico* neuron models [San19; Kan19].

Observations of synchronized states have also been reported outside of fully developed brains in *in vitro* models, e.g. [Kot14]. In this section, we will see that the SMI is a suitable measure for accessing synchronization between neurons. Similar methods exist, such as (general) correlation measures, e.g. cross-correlation [Gon15], transfer entropy [Schoo; Quioo] and Hilbert transformation [Tas98; Lac99].

In contrast to the systems we discussed in previous chapters, synchronization in neurons is event-driven. Instead of continuous coupling, neurons “communicate” by rapid discharge. Peaks in voltage can lead to discharge in other neurons, leading to an avalanche of discharges. The avalanche is ended by a refractory period, in which neurons are insensitive to an outside stimulus.

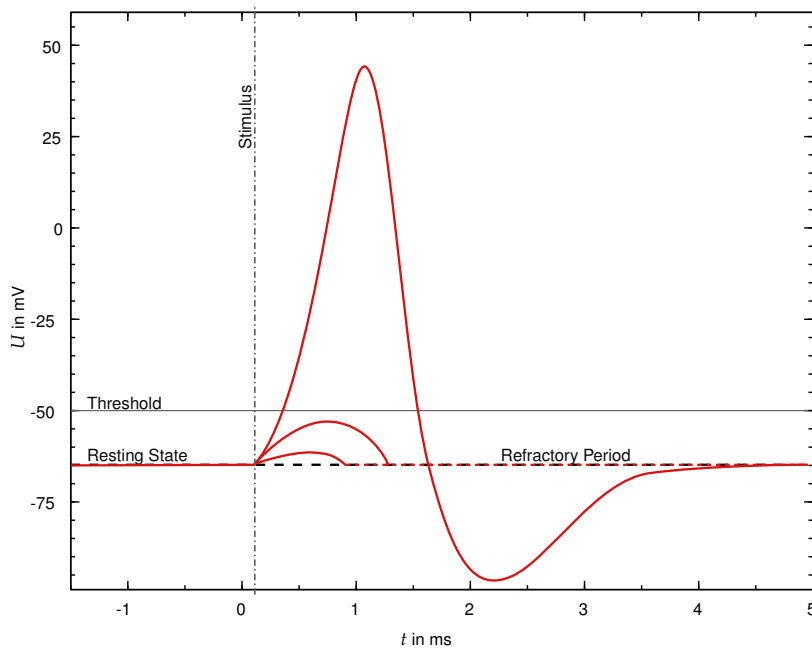


Figure 5.6: Potential in a neuron when exposed to an external stimulus. When the stimulus is strong enough to “push” the potential over the threshold, the cell’s ion channels open and the signal is amplified. The spike of a stimulus is followed by cell depolarization and a refractory period in which the neuron is not susceptible to a new stimulus. Small stimuli that do not exceed the threshold do not resolve into a spike and are “lost” in the neuron.

Essentially, the synchronization is driven by the neurons reset into their base state. An initial small current in a neuron is induced by the firing of other neurons. If this initial current crosses a certain threshold ion channels will open in the neuron and increase the discharge, leading to the observed spike (compare with Figure 5.6).

Neurons build potential by separating positively and negatively charged ions. It is discharged either by external stimulation or spontaneously.

Spontaneous discharge in some neurons can trigger others. If enough neurons spike, an avalanche runs through the system, showing as a synchronized beat.

After every discharge, the potential within the neuron and outside is in an equilibrium, and the potential difference has to be re-established by the neuron. Synchronization between neurons is established by the dead time after each spike, where neurons are incapable of acting on new external information. As signals within the dead time quickly die out, those that match the other neurons rhythm get amplified.

In this section, we will evaluate the emerging synchronization in an *in vitro* model of hippocampal neurons. Action potentials are recorded over the course of 10 days (with recordings starting on day 4).

The action potential of the neurons can be recorded down to a single neuron's resolution. We will use the SMI to evaluate the strength of synchronization between these neurons. While methods using MI are already widely used [Bal17; Gri18], we can provide a mathematical sound base for normalization.

### 5.2.1 Methods

Recordings of action potentials can be analyzed in two ways. Spike timing can be extracted and used for further analysis, so-called spike train analysis. A different approach is the direct comparison of the signals. The latter method is usually some form of linear or non-linear correlation test. Some typical methods include Cross Correlation, Granger Causality, MI [Bal17; Gri18] and Transfer Entropy [Qui00].

In the following, we will use the SMI as the fundamental measure for synchronization between two signals. We use the methods developed in Section 4.1 and Section 3.2.2, more specifically a modification of the WSMI and the MSMI.

Previous work with methods based on information theory used unnormalized MI or transfer entropy, which make the magnitude of the results depend on the chosen symbolization and recording [Qui02]. We provide an absolute measure, where 1 is full synchronization.

### 5.2.2 Experiment

We use a Multi Electrode Arrays (MEA) to record the action potentials. MEAs consist of a small chip with many electrodes installed on them. They are implemented in the model and remain there from day 1 until the experiment is finished. They allow easy activity observation in high-volume experiments, although single cells cannot be targeted. MEAs can be used for *in vivo* and *in vitro* measurements.

[Pino6] MEA experiments allow us to study the development and function of neurons and neuronal systems [Bro16].

Neurons can be extracted in a very early, stem cell like stage or mostly matured. Where in the second case the neurons have mostly developed their firing capabilities and produce strong action potentials, the stem cell neurons' signals are mostly weak and undergo severe changes during their growth. In this experiment, we focused on a model of mature neurons. The experiments were carried out at the Laube laboratory of TU Darmstadt within the work of [Kau21] and were kindly provided for this analysis. Details of the experiments were published in [Kau21].

In preparation for the recordings, the neurons were planted on MEA Chips from Multi Channel Systems MCS GmbH, Reutlingen, Germany. They grew on these plates for up to 10 days, with recordings of the action potential on days 4, 5, 7, and 10. The experiments were conducted "parasitically", which means that they were part of a different experiment further described in the original work in [Kau21]. Action potentials were recorded with a resolution of 0.1 ms / 10 kHz for 60 channels and 2 minutes per sample. For later processing, the raw values were exported to hdf5 [The97] for further processing in *python* and *julia*.

Here, we will use SMI to identify the changing synchronization patterns during synaptic growth in mature neuronal cultures.

### 5.2.3 Results

With the method described in Section 5.2.2, we take measures from day 4, 5, 7 and 10 from the MEA recordings of hippocampal neurons. The batch of models was observed within the last batch of experiments run for the work in [Kau21].

Experiments are usually performed on day 14 when neurons are at their most active. Later, their activity declines before the cells die. In the models selected for later analysis in this work, neuronal activity declined earlier than expected. The highest observed synchronization was on day 10, after which we did not measure any further signals. It is unclear if the conductivity of MEA's electrodes decreased or if the neurons entered cell death earlier than in regular experiments.

In Figure 5.7 we compare the peaks of the action potential in each recording. Figure 5.7 a) shows the neuronal activity on day 4, Figure 5.7 b) on the same day for the same model. For comparison, Figure 5.7 c) shows the activity on day 14 for a healthy experiment.

Since our experiment was conducted only parasitically, we were unable to produce further recordings of the maturing process of the model. We still applied SMI on the existing data. However, we expect that the results will be more pronounced in a healthy model.

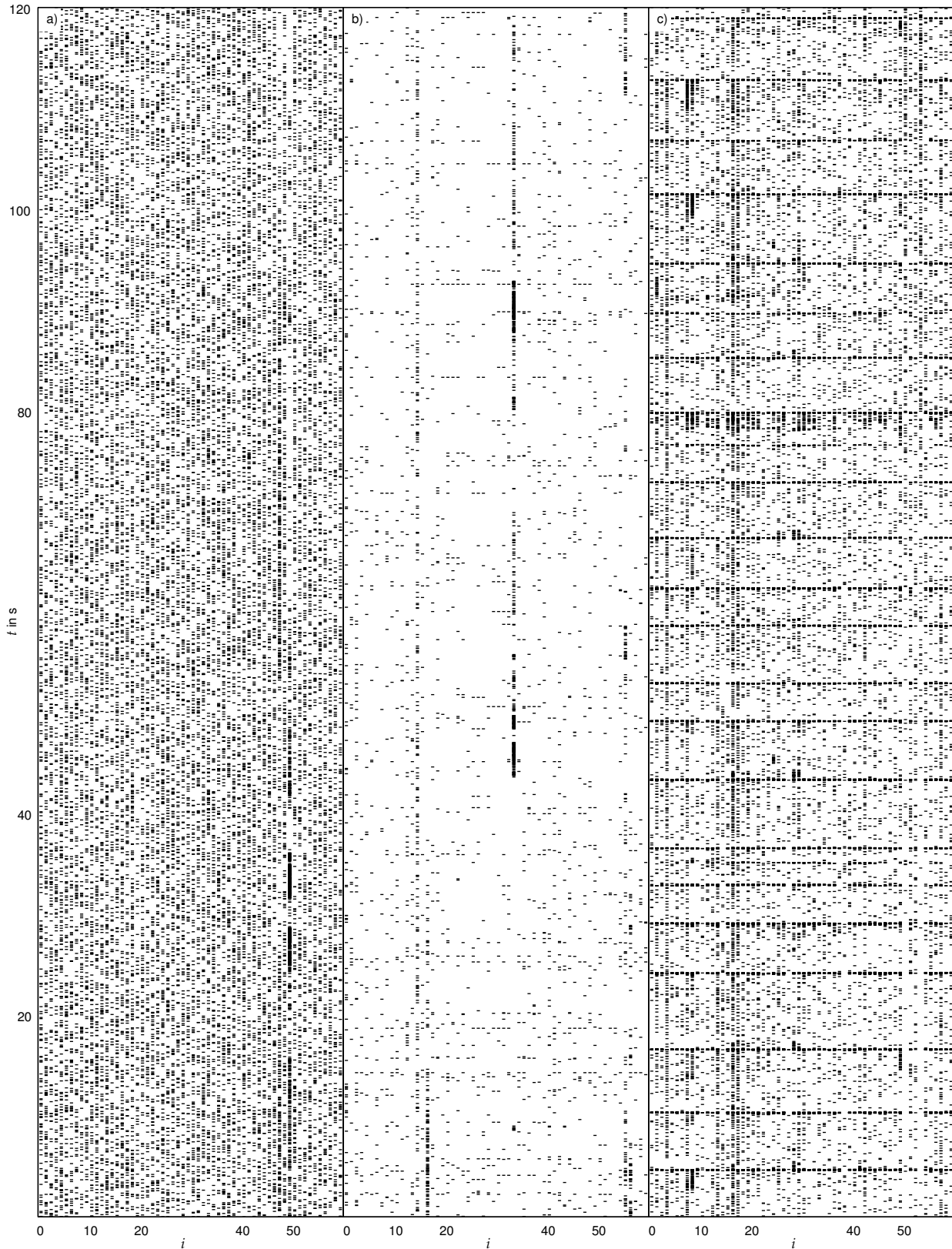


Figure 5.7: Synchronization of neurons during growth of the *in vitro* model of hippocampal neurons. The model monitored for this experiment shows decreased signal strength on day 10 where a lifetime beyond day 14 was expected. From all electrodes  $i$  the peaks are extracted from the recording of the potentials. The peaks are presented for a period of  $t = 120$  s. The sections show for a) on day 5 and b) on day 10. While a) and b) are from the same model, c) are peaks from a different model at day 14. We can see that on day 5, the neurons show high activity. This is in contrast to day 10 of the same model. Activity is depleted, possibly due to stress-induced neuron death. Usually, the highest rates and synchronization are expected for day 14, as shown in a different model in c).

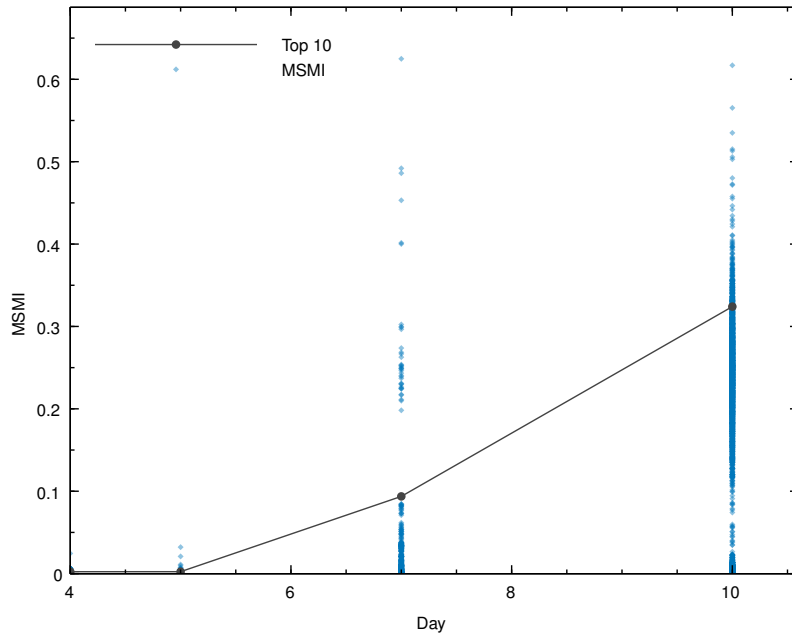


Figure 5.8: Despite the premature cell death of the neurons in our hippocampus *in vitro* model, increased synchronization can be detected. We calculated the MSMI between all pairs of electrodes for days 4, 5, 7, and 10. Furthermore, we calculate the average of the top 10 % MSMIs for each day.

The original signals showed some drifts, where the potential wandered several orders of magnitude of the spike signal over the course of several seconds. These artifacts affect all channels similarly; we removed them by applying a high-pass filter. This was done using a *butter* filter from *scipy's signal* package [Vir20]. The lower frequency cut is at 1 Hz, and for the high frequency it is at 5000 Hz.

Since neurons mainly synchronize via their spikes, we did not want to destroy these signals and both the high and the low pass filters had to be adjusted to leave the signals untouched.

The dynamics of spikes lasts for about 10 to 20 steps (1 ms - 2 ms). This limited the use of a low-pass filter to remove high-frequency noise to only affect a few steps.

On the filtered data, we then applied the SMI between all pairs of channels. For each pair, we calculated the SMI on 10 non-intersecting windows over the course of all 120 seconds. Values of each step in time were sorted into 10 equal-sized bins between the lowest and highest values in each window.

We calculated an average SMI for each pair based on the 10 windows. The results for the pairwise SMI are shown in Figure 5.8.

In addition, we plotted the mean of the highest 10 % SMI readings for each day. Together with the windowed calculation of the SMI, we were able to create a reliable measure without manual pre-processing. Unreliable/dead channels and runaway synchronization measures are taken into account; however, the evaluation of only the 10 % highest values is stable against both types of error.

It shows that the synchronization indicated by the SMI grows while the neurons in the experiment mature.

To validate the findings of increased synchronization, we also studied the action potentials directly. In Figure 5.9 we show some exemplary action potentials for day 5 in Figure 5.9 a) and day 10 in Figure 5.9 b).

The running SMI alongside the action potential is calculated with time windows of 50 steps and values in 10 bins. Due to the small sample size and noisy recordings, the SMI values are strongly elevated compared to the previous calculation with samples consisting of 120,000 values (1/10 of the total time series).

The decreased sample size makes SMI more susceptible to spurious correlation, as also seen in Figure 5.9. However, larger sample sizes delude the effect of spikes on the synchronization.

While the SMI of both Figure 5.9 a) and Figure 5.9 are elevated compared to the results expected from Figure 5.8 the increased synchronization on day 10 shows itself in higher SMI readings.

In Figure 5.9 b) we can see that the local SMI peaks where the action potential shows spikes. This can be seen at  $t = 46.57$  ms and  $t = 45.4$  ms where strong coherent spikes show over all neurons plotted together with a subsequent increase in the SMI.

#### 5.2.4 Discussion

We showed that the synchronization of maturing neurons is accessible via the SMI. An *in vitro* model of hippocampal neurons was observed from day 4 to day 10. The action potential recordings were taken with a MEA. Evaluation with the SMI showed that the synchronization between neurons increases during this period.

As synchronization between neurons is achieved mainly via rapid depolarization of their membrane and thus event-based rather than continuous, the action potential between these events is dominated by noise. These are unfavorable conditions for the SMI as fewer data points are expected to correlate. This can decrease the contrast between decoherent and synchronized states. The problem increases when the noise is correlated between the electrodes of the MEA. In our experiment, we observed a difference in synchronization between the early and late stages of the model.

These results were found despite the model's activity declining early in its experiment life cycle. Usually, experiments with the models are conducted on day 14, when the activity is highest. However, we found that in our model no action potentials were measured after day 10. We expect that in a repeated measurement for healthy models, the SMI can show even stronger contrast than within the current work.

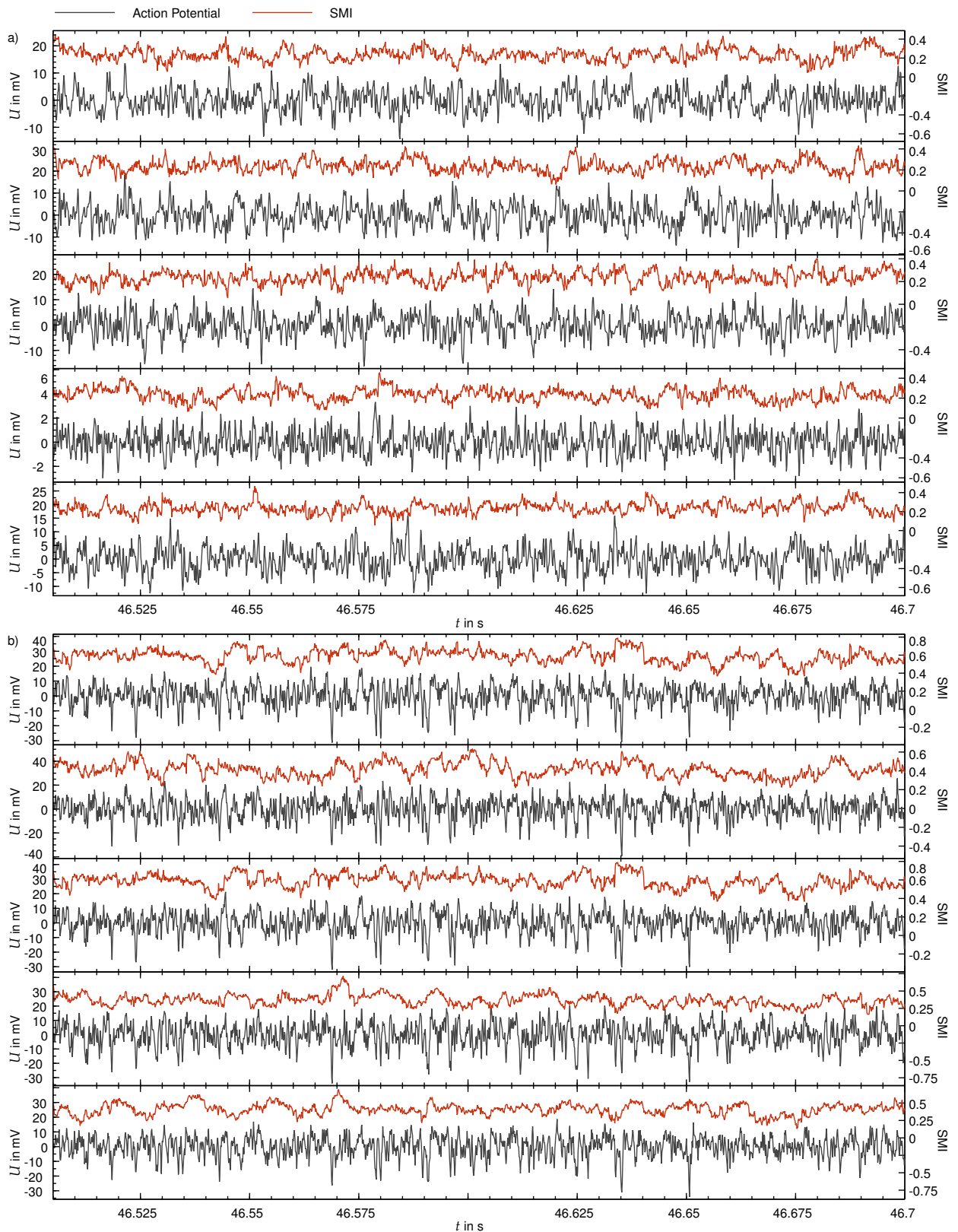


Figure 5.9: An increase of the SMI can be observed close to peaks in the signal. This happens despite the noise that dominates the signal. Potentials were recorded and filtered as described in Section 5.2.2. Additionally, for each channel, the local synchronization for the channel with the highest mutual average synchronization is given. In a) we show recordings of the action potential after 7 and 14 days (a) and b), respectively, over a period of  $\approx 0.2$  s.





## Discussion & Outlook

In this thesis, we investigated a Mutual Information (MI) based approach to identify synchronization in synthetic and real-world data. MI is a method from information theory that measures the general correlation between two variables of a bivariate distribution. Previous work has used the MI as a synchronization measure (e.g. [Pal01]). However, we could not find a formal proof for a relation to previous definitions of synchronization.

Chapter 2 of this thesis rigorously proves that MI measures the degree of synchronization in any complex dynamics. As a base for synchronization, we use generalizations of the concept developed in [Rul95] [Boc01]. As a result, we find that for generalized synchronization, the MI can be used to identify synchronization. For synchronous systems, only the  $I(X;Y)$  will approach the entropy given by  $I(X)$  or  $I(Y)$ .

By normalizing the MI with  $\min[I(X), I(Y)]$ , we derived the Synchronized Mutual Information (SMI). We were able to show that for analytically known joint probability distributions, the SMI can discriminate between synchronous and non-synchronous regimes under the notion of Generalized Synchronization (GS) (see Section 2.6.2). With some minor modifications, it can also be used to detect Lagged Synchronization (LS) and Phase Synchronization (PS). Unlike previous methods based on information theory, the SMI is a 0-1 bound measure. This allows the classification without a "ground truth" in the form of a non-synchronous time series to compare.

Since the true underlying probability distribution between two trajectories is unknown, the performance of the SMI is limited by the available samples. We expect that the SMI will not converge to 1 in any practical application with limited real-world data.

The quality of the SMI estimation is limited by the sample size, discretization strategy, and the estimator of entropy and SMI. These factors are discussed in Section 2.6.4 and in Section 2.6.5. We explore the practical application of the SMI by comparing it to previous work on synchronization. Chapter 3 first checks for GS in a driver-response system, where we can compare it with the auxiliary system method. Second, we replicate previous work on synchronization in networks

of logistic maps proposed by [Ant17].

The first system is presented in Chapter 3 and consists of a Rössler driving a Lorenz oscillator. As a reference, we use the auxiliary system method to detect GS. It introduces an auxiliary response system, identical to the reference system, that replaces the initial parameters by small amounts [Aba96]. In the original work, it is shown that the convergence of the auxiliary and reference systems shows synchronization between the driver and the response system.

Our results show that the SMI is able to distinguish between synchronized and decoherent parameter regimes. These results are obtained while solving a restriction when applying the auxiliary system method: Already in the initial work [Aba96], it was mentioned that in certain circumstances, the auxiliary and reference system may not converge, despite the presence of synchronization. We mitigated the problem by creating an ensemble of auxiliary systems with different displacements. If any pair of auxiliary and reference systems converge, we can be sure of the existence of synchronization. Since our method does not rely on an auxiliary system, it avoids this pitfall.

Furthermore, we observed that our method can even provide reliable results when applied to a reduced phase space. While the initial proof in Section 2.4 requires the knowledge of the full phase space to account for the formal relation between SMI and GS, we see that in certain cases this knowledge might not be necessary. As a result, the method can also be applied to data, where the full phase space is not known like real-world time series. We further explore this application in Chapter 5.

The linear chain of logistic maps allowed us to replicate the results obtained in previous work by [Ant17] and at the same time show us how our method could provide additional insight. In the original work, the authors scanned the parameter space of a linear chain of logistic maps. They found regimes of Identical Synchronization (IS) in this space. We replicated their results for IS and found that an even larger regime of synchronization can be found with the SMI. Our results indicate that other types of synchronization might form a frontier between parameter space areas of the synchronized and decoherent state.

The SMI allows us to use the same approach to determine synchronization between two systems, independently of the dynamics of the system. In other approaches, it is often necessary to tailor the method to the phase-space dynamics of the coupled system (e.g. the Largest Transversal Lyapunov Exponent (LTLE), see [Har19; Zha20]). To scale from two- to multi-component systems, we only need to find a suitable aggregation method, matching our phenomenon of interest.

In Section 3.2 we proposed an extension for the pair-based SMI, allowing us to measure the synchronization state of a multi-component system. While we concentrated on fully synchronized systems in our

work on the linear chain, partially synchronized systems are well-known and subject to recent research. In Chapter 4 we explore the applicability of the methods developed and variants of their own systems with partial synchronization.

We found that aggregation of SMI works best in situations with temporally stable synchronization or at least long-lived synchronized states. Systems where aggregation worked well include chimera states (Section 4.4) and cluster synchronization (Section 4.3). Situations where synchronization between components is only short-lived, such as intermittent synchronization (Section 4.2), were shown to be less reliable. This limitation of the SMI stems from the limited sample size of the synchronous state in our test system for intermittent synchronization.

We continue our investigation in Chapter 4 by injecting uncorrelated noise into the coupling and testing the stability of different types of networks against the injection of noise in the coupling. As expected, uncorrelated noise generally weakens synchronization. We find that within our choice of networks, the resilience to noise was mainly given by the number of coupling partners rather than by the coupling scheme itself. With more connections, the transition between the synchronized and incoherent states seems to smooth out—contributing to a decreased level of noise. Other research suggests that noise can have a positive effect on synchronization in certain cases [Zha20; Kat20]. While we found evidence for noise-assisted stabilization of synchronization, our results on the stabilizing effect of noise were inconclusive.

However, even in these cases, some coherence seems to remain between components—a fact that is captured by a decline of SMI between the frontiers of noisy systems and the synchronized state. This is a problem that real-world systems also experience, where the coupling is rarely without interference from other systems. As the SMI also catches these shades of coherence, in the final chapter, we apply it to measure the coherence between stock prices of Dow Jones listed companies and in an *in vitro* model of hippocampal neurons. We find for both examples that the SMI captures some expected dynamics very well, despite high levels of noise.

In Section 5.1 we assess the general correlation of stock prices between Dow Jones listed companies for closing prices from 20 years. We compare the SMI to a different MI-based method, the NMI. A network of the strongest statistical correlations between companies is created. In this network, we find clusters that reproduce industry sectors. Comparing the properties of the NMI and SMI shows that they assess different aspects of the correlation between companies' stocks.

Closing Chapter 5 is a study of the change in (observed) synchronization during the growth of an *in vitro* model of hippocampal neurons in Section 5.2. In contrast to our previous models, neurons

experience event-driven rather than continuous synchronization. Information about their state is only updated on spikes. Values of the recorded action potential are thus only correlated on these events, while the other parts are dominated by noise. Methods oblivious of spiking events are expected to be at a disadvantage compared to other methods specialized in spiking events.

Nevertheless, we were able to show that the SMI recognized the maturing interneural connections of an *in vitro* model. Over ten days, neuron stem cells matured and established connections with each other. During the observed time period, the spikes in the neuron's action potentials aligned. We were able to show that this process is picked up by the SMI despite a large part of the signal being noise.

## 6.1 Advantages and Limitations of the SMI

As with any method, the SMI comes with its own set of advantages and limitations.

Some methods to find synchronization, like the LTLE, require the knowledge of the analytic dynamic equations to determine the synchronization between two states. In the case of the LTLE a specific formulation of phase space dynamics must be found to be able to evaluate the LTLE. Other methods operate on the observed phase space without the need to understand the underlying dynamics. The SMI falls into the second category.

We were able to show in Section 4.4.2 that the SMI can be on par with the LTLE in correctly identifying synchronized systems. We also showed the performance of noise perturbed systems, something that is not easily accessible to other methods like the LTLE [Zha20].

Unlike competing methods such as IS, SMI is sensitive to a broader understanding of synchronization. We have seen in Section 3.2 that this increased sensitivity can lead to new insights.

For higher-dimensional systems, such as the Lorenz and Rössler systems in Section 1.1.4, we found that our approach required high sampling rates to produce reliable results. Particularly in these high-dimensional cases, the SMI benefits from MI estimators with improved bias correction. When these methods become available, they can replace our choice of the Grassberger estimator. We expect that with improved symbolization strategies, similar results can be obtained with a decreased sampling frequency. Possible strategies were discussed in Section 2.6.4 and Section 2.6.5.

When processing real-world data, the statistical nature of the method means that the noise in the recorded data will have little effect on the results of the SMI. This is in contrast to other methods, such as the Equation (3.11) synchronization error used to detect IS, where the noise adds up and distorts the result.

## 6.2 Outlook

As mentioned in Section 2.6.5, users should be aware not to accidentally use estimators for differential entropy instead of an estimator for Shannon entropy. Although both concepts look conceptually similar, differential entropy does not share all of the properties of Shannon entropy. Differential entropy can produce negative results. Additionally, it is not invariant to changes on its scale.

To show that the SMI can indicate the existence of GS we used several properties of Shannon entropy. Differential entropy does not have all of the properties of Shannon entropy. It is unclear if the relation between MI and GS still holds when the Shannon entropy estimators are replaced by differential entropy estimators.

It is at this point unclear that the upper bound of the SMI will still indicate synchronization when replacing Shannon with differential entropy. As many of the state-of-the-art estimators are constructed for differential entropy, a compatible differential SMI is desirable.

In this thesis, we have discussed pair interactions of coupled dynamical systems. For multi-component systems, as discussed in Section 3.2 and Chapter 4, we have also applied our pair-based approach. We can also foresee oscillators that synchronize with two partners instead of a single one. These types of interaction are detectable with Conditional Mutual Information (CMI). CMI is defined as [Mac03]

$$I(X; Y|Z) = \sum_{x,y,z} p(x,y,z) \frac{p(z)p(x,y,z)}{p(x,z)p(y,z)}. \quad (6.1)$$

In the CMI, prior knowledge of a third system  $Z$  (or more) is used to further investigate the relationship between  $X$  and  $Y$ . With the additional knowledge of  $Z$ , a system where  $I(X; Y) = 0$  can still show  $I(X; Y|Z) > 0$ .  $Z$  provides a "link" between  $X$  and  $Y$ . Conditional MI has been used in previous work to identify the direction of coupling [Li10; Li13]. However, we assume that there are systems where not only pairs of coupled oscillators are synchronized, but the synchronization is with a third, collective state of the coupling partners.

Reviewing recent work on chimera states has shown that most work with chimera states is focused on identifying IS. We are unaware of any limitations that prevent GS in chimera states. One assumption is that IS is computationally easier to implement than GS. We have shown in Section 4.4 that the aggregated SMI is capable of identifying chimera states (even though we are likely to observe IS since the models are based on [Zha21]). With SMI, we have provided a solid base for future work to find chimera states not based on IS but GS.

While we were unable to find such states in this work, future studies may be able to show the existence of these states. One possible candidate is a modification of the coupled Lorenz-Rössler system in Section 3.1. By introducing two clusters of the above driver/response system and coupling a component of each oscillator to the mean-field of the other cluster, we introduce a setup similar to Section 4.4.

Appendix

A

Program for calculating the maximum Lyapunov exponent for a discrete map. The user provides the initial states for the reference `initial_state`, the perturbed trajectory `initial_perturbed_state`. The maximum distance threshold between the reference and the perturbed state, as well as a function for the system dynamics map, a starting distance for the perturbations `d0` and `N` steps to evolve, also have to be provided. The average Lyapunov exponent per step is evaluated by evolving both the perturbed and reference states while tracking their distance. If the distance exceeds the threshold, the perturbed state is reset to distance `d0`. With the function `aligned_vector` the direction of the initial perturbation is maintained during rescaling to `d0`. The distance between the vectors is calculated with the Euclidean norm `norm`. The algorithm was first proposed in [Ben76], several implementations are available; this one is based on the work for [Dat18].

## A.1 Maximum Lyapunov Exponent

```
# User provided variables:
# initial_state, initial_perturbed_state, # d0, threshold, N
# User provided functions:
# map (A function containing the system dynamics and
#     generating the next state given the current)

function norm(vec)
    return sqrt(sum(vec**2))
end

function aligned_vector(source,perturb)
    vec = (perturb - source)
    vec /= norm(vec)
    return vec
end

system_state = initial_state
perturbed_state = initial_perturbed_state

lambda = 0
i = 0
while i < N
    while dist < threshold && i < N
        system_state = map(system_state)
        perturbed_state = map(perturbed_state)
        dist = norm(system_state - perturbed_state)
        i += 1
    end
    a = dist/d0
    lambda += log(a)
    perturbed_state = system_state
        + aligned_vector(system_state, perturbed_state) * d0

    dist = d0
end
lambda = lambda / i
```



# Bibliography

- [Aba96] H. D. I. Abarbanel, N. F. Rulkov, and M. M. Sushchik. “Generalized Synchronization of Chaos: The Auxiliary System Approach”. In: *Phys. Rev. E* 53.5 (May 1, 1996), pp. 4528–4535. DOI: 10.1103/PhysRevE.53.4528.
- [Abro4] D. M. Abrams and S. H. Strogatz. “Chimera States for Coupled Oscillators”. In: *Phys. Rev. Lett.* 93.17 (Oct. 22, 2004), p. 174102. DOI: 10.1103/PhysRevLett.93.174102.
- [Ahn11] S. Ahn, C. Park, and L. L. Rubchinsky. “Detecting the Temporal Structure of Intermittent Phase Locking”. In: *Phys. Rev. E* 84.1 (July 5, 2011), p. 016201. DOI: 10.1103/PhysRevE.84.016201.
- [Ahn17] S. Ahn and L. L. Rubchinsky. “Potential Mechanisms and Functions of Intermittent Neural Synchronization”. In: *Front. Comput. Neurosci.* 11 (May 30, 2017). DOI: 10.3389/fncom.2017.00044.
- [Ame15] V. Ameri et al. “Mutual Information as an Order Parameter for Quantum Synchronization”. In: *Phys. Rev. A* 91.1 (Jan. 2015). DOI: 10.1103/physreva.91.012301.
- [Ant17] C. Anteneodo, J. C. González-Avella, and R. O. Vallejos. “From Synchronous to One-Time Delayed Dynamics in Coupled Maps”. In: *Phys. Rev. E* 95.6 (June 2017). DOI: 10.1103/physreve.95.062213.
- [Arc14] E. Archer, I. M. Park, and J. W. Pillow. “Bayesian Entropy Estimation for Countable Discrete Distributions”. In: *J. Mach. Learn. Res.* 15.81 (2014), pp. 2833–2868. URL: <http://jmlr.org/papers/v15/archer14a.html>.
- [Are08] A. Arenas et al. “Synchronization in Complex Networks”. In: *Phys. Rep.* 469.3 (Dec. 2008), pp. 93–153. DOI: 10.1016/j.physrep.2008.09.002.
- [Ata04] F. M. Atay, J. Jost, and A. Wende. “Delays, Connection Topology, and Synchronization of Coupled Chaotic Maps”. In: *Phys. Rev. Lett.* 92.14 (Apr. 8, 2004), p. 144101. DOI: 10.1103/PhysRevLett.92.144101.
- [Bak98] G. L. Baker, J. A. Blackburn, and H. J. T. Smith. “Intermittent Synchronization in a Pair of Coupled Chaotic Pendula”. In: *Phys. Rev. Lett.* 81.3 (July 20, 1998), pp. 554–557. DOI: 10.1103/PhysRevLett.81.554.
- [Bal17] K. R. Ball et al. “A Multivariate Extension of Mutual Information for Growing Neural Networks”. In: *Neural Netw.* 95 (Nov. 1, 2017), pp. 29–43. DOI: 10.1016/j.neunet.2017.07.009.
- [Ban19] K. Bansal et al. “Cognitive Chimera States in Human Brain Networks”. In: *Sci. Adv.* 5.4 (Apr. 1, 2019), p. 8535. DOI: 10.1126/sciadv.aau8535.
- [Baş13] E. Başar. “Brain Oscillations in Neuropsychiatric Disease”. In: *Dialogues Clin. Neurosci.* 15.3 (Sept. 30, 2013), pp. 291–300. DOI: 10.31887/DCNS.2013.15.3/ebasar.
- [Ben76] G. Benettin, L. Galgani, and J.-M. Strelcyn. “Kolmogorov Entropy and Numerical Experiments”. In: *Phys. Rev. A* 14.6 (Dec. 1, 1976), pp. 2338–2345. DOI: 10.1103/PhysRevA.14.2338.
- [Ber20] R. Berner, J. Sawicki, and E. Schöll. “Birth and Stabilization of Phase Clusters by Multiplexing of Adaptive Networks”. In: *Phys. Rev. Lett.* 124.8 (Feb. 24, 2020), p. 088301. DOI: 10.1103/PhysRevLett.124.088301.

- [Bez17] J. Bezanson et al. “Julia: A Fresh Approach to Numerical Computing”. In: *SIAM Rev.* 59.1 (2017), pp. 65–98. DOI: 10.1137/141000671.
- [Boco0] S. Boccaletti et al. “The Control of Chaos: Theory and Applications”. In: *Phys. Rep.* 329.3 (May 1, 2000), pp. 103–197. DOI: 10.1016/S0370-1573(99)00096-4.
- [Boco1] S. Boccaletti, L. M. Pecora, and A. Pelaez. “Unifying Framework for Synchronization of Coupled Dynamical Systems”. In: *Phys. Rev. E* 63.6 (May 29, 2001), p. 066219. DOI: 10.1103/PhysRevE.63.066219.
- [Boc18] S. Boccaletti et al. *Synchronization: From Coupled Systems to Complex Networks*. 1st ed. Cambridge University Press, Mar. 29, 2018. DOI: 10.1017/9781107297111.
- [Broo0] R. Brown and L. Kocarev. “A Unifying Definition of Synchronization for Dynamical Systems”. In: *Chaos* 10.2 (May 31, 2000), pp. 344–349. DOI: 10.1063/1.166500.
- [Bro10] E. N. Brown, R. Lydic, and N. D. Schiff. “General Anesthesia, Sleep, and Coma”. In: *N. Engl. J. Med.* 363.27 (Dec. 30, 2010). Ed. by R. S. Schwartz, pp. 2638–2650. DOI: 10.1056/NEJMra0808281.
- [Bro16] J. P. Brown et al. “Editor’s Highlight: Evaluation of a Microelectrode Array-Based Assay for Neural Network Ontogeny Using Training Set Chemicals”. In: *Toxicol. Sci.* 154.1 (Nov. 1, 2016), pp. 126–139. DOI: 10.1093/toxsci/kfw147.
- [Cám19] A. de la Cámara, T. Birner, and J. R. Albers. “Are Sudden Stratospheric Warmings Preceded by Anomalous Tropospheric Wave Activity?” In: *J. Clim.* 32.21 (Nov. 1, 2019), pp. 7173–7189. DOI: 10.1175/JCLI-D-19-0269.1.
- [Chi10] D. R. Chialvo. “Emergent Complex Neural Dynamics”. In: *Nat. Phys.* 6.10 (Oct. 2010), pp. 744–750. DOI: 10.1038/nphys1803.
- [Chi60] B. V. Chirikov. “Resonance Processes in Magnetic Traps”. In: *Sov. J. At. Energy* 6.6 (Dec. 1, 1960), pp. 464–470. DOI: 10.1007/BF01483352.
- [Cho17] Y. S. Cho, T. Nishikawa, and A. E. Motter. “Stable Chimeras and Independently Synchronizable Clusters”. In: *Phys. Rev. Lett.* 119.8 (Aug. 24, 2017), p. 084101. DOI: 10.1103/PhysRevLett.119.084101.
- [Chr14] H. Christodoulidi et al. “Phase Transitions in Models of Bird Flocking”. In: *Chaos, Information Processing and Paradoxical Games*. 0 vols. World Scientific, Feb. 24, 2014, pp. 383–398. DOI: 10.1142/9789814602136\_0019.
- [Con18] M. Contreras and C. Anteneodo. “Complete Synchronization of Chaotic Maps under Advection”. In: *Phys. Rev. E* 98.5 (Nov. 2018). DOI: 10.1103/physreve.98.052222.
- [Cov05] T. M. Cover and J. A. Thomas. *Elements of Information Theory*. 2005. 1–748. DOI: 10.1002/047174882X.
- [Dat18] G. Datseris. “DynamicalSystems.Jl: A Julia Software Library for Chaos and Nonlinear Dynamics”. In: *J. Open Source Softw.* 3.23 (Mar. 14, 2018), p. 598. DOI: 10.21105/joss.00598.
- [Fam70] E. F. Fama. “Efficient Capital Markets: A Review of Theory and Empirical Work”. In: *J. Finance* 25.2 (May 1970), p. 383. DOI: 10.2307/2325486.
- [Frä01] O. Fränze. “Alexander von Humboldt’s Holistic World View and Modern Inter- and Transdisciplinary Ecological Research”. In: *Northeast. Nat.* 8 (2001), pp. 57–90. JSTOR: 4130727.

- [Fra05] A. L. Fradkov and R. J. Evans. “Control of Chaos: Methods and Applications in Engineering”. In: *Annu. Rev. Control.* 29.1 (Jan. 1, 2005), pp. 33–56. DOI: 10.1016/j.arcontrol.2005.01.001.
- [Fuj83] H. Fujisaka and T. Yamada. “Stability Theory of Synchronized Motion in Coupled-Oscillator Systems:” in: *Prog. Theor. Phys.* 69.1 (Jan. 1, 1983), pp. 32–47. DOI: 10.1143/PTP.69.32.
- [Gao16] W. Gao, S. Oh, and P. Viswanath. “Demystifying Fixed K-Nearest Neighbor Information Estimators”. In: *ArXiv.org* (Aug. 10, 2016). arXiv: 1604.03006 [cs, math, stat].
- [Gau96] D. J. Gauthier and J. C. Bienfang. “Intermittent Loss of Synchronization in Coupled Chaotic Oscillators: Toward a New Criterion for High-Quality Synchronization”. In: *Phys. Rev. Lett.* 77.9 (Aug. 26, 1996), pp. 1751–1754. DOI: 10.1103/PhysRevLett.77.1751.
- [Gen14] D. Gencaga, N. K. Malakar, and D. J. Lary. “Survey on the Estimation of Mutual Information Methods as a Measure of Dependency versus Correlation Analysis”. In: *AIP Conference Proceedings*. Canberra, ACT, Australia, 2014, pp. 80–87. DOI: 10.1063/1.4903714.
- [Glo18] S. Global. *Global Industry Classification Standard*. 2018. URL: <https://www.spglobal.com/marketintelligence/en/documents/112727-gics-mapbook-2018-v3-letter-digitalspreads.pdf> (visited on 11/24/2020).
- [Gono04] J. M. González-Miranda. *Synchronization and Control of Chaos: An Introduction for Scientists and Engineers*. Imperial College Press, Oct. 2004. DOI: 10.1142/p352.
- [Gon14] J. C. González-Avella, M. G. Cosenza, and M. San Miguel. “Localized Coherence in Two Interacting Populations of Social Agents”. In: *Physica A* 399 (Apr. 1, 2014), pp. 24–30. DOI: 10.1016/j.physa.2013.12.035.
- [Gon15] A. M. González-Montoro et al. “Bootstrap Testing for Cross-Correlation under Low Firing Activity”. In: *J. Comput. Neurosci.* 38.3 (June 1, 2015), pp. 577–587. DOI: 10.1007/s10827-015-0557-5.
- [Gra08] P. Grassberger. “Entropy Estimates from Insufficient Samplings”. Jan. 4, 2008.
- [Gra20] L. J. Gray et al. “Forecasting Extreme Stratospheric Polar Vortex Events”. In: *Nat. Commun.* 11.1 (1 Sept. 15, 2020), p. 4630. DOI: 10.1038/s41467-020-18299-7.
- [Gra88] P. Grassberger. “Finite Sample Corrections to Entropy and Dimension Estimates”. In: *Phys. Lett. A* 128.6-7 (Apr. 1988), pp. 369–373. DOI: 10.1016/0375-9601(88)90193-4.
- [Gri18] E. D. Gribkova, B. A. Ibrahim, and D. A. Llano. “A Novel Mutual Information Estimator to Measure Spike Train Correlations in a Model Thalamocortical Network”. In: *J. Neurophysiol.* 120.6 (Sept. 5, 2018), pp. 2730–2744. DOI: 10.1152/jn.00012.2018.
- [Gro13] C. Gros. *Complex and Adaptive Dynamical Systems*. Berlin, Heidelberg: Springer Berlin Heidelberg, 2013. DOI: 10.1007/978-3-642-36586-7.
- [Gue17] R. Guevara Erra, J. L. Perez Velazquez, and M. Rosenblum. “Neural Synchronization from the Perspective of Non-linear Dynamics”. In: *Front. Comput. Neurosci.* 11 (2017). DOI: 10.3389/fncom.2017.00098.
- [Guo18] X. Guo, H. Zhang, and T. Tian. “Development of Stock Correlation Networks Using Mutual Information and Financial Big Data”. In: *PLOS ONE* 13.4 (Apr. 18, 2018), e0195941. DOI: 10.1371/journal.pone.0195941.

- [Guo19] Z. Guo, L. Chen, and P. Liu. “Short-Term Stock Forecasting Based on Phase Space Reconstruction and Cluster Analysis”. In: *2019 11th Int. Conf. Intell. Hum.-Mach. Syst. Cybern. IHMSC*. Vol. 2. Aug. 2019, pp. 50–53. DOI: 10.1109/IHMSC.2019.10107.
- [Har19] J. D. Hart et al. “Topological Control of Synchronization Patterns: Trading Symmetry for Stability”. In: *Phys. Rev. Lett.* 122.5 (Feb. 8, 2019), p. 058301. DOI: 10.1103/PhysRevLett.122.058301.
- [Har20] C. R. Harris et al. “Array Programming with NumPy”. In: *Nature* 585.7825 (Sept. 17, 2020), pp. 357–362. DOI: 10.1038/s41586-020-2649-2.
- [Hau21] S. W. Haugland. “The Changing Notion of Chimera States, a Critical Review”. In: *J. Phys. Complex.* 2.3 (June 2021), p. 032001. DOI: 10.1088/2632-072X/ac0810.
- [Hiro04] M. W. Hirsch and R. Devaney. *Differential Equations, Dynamical Systems, and an Introduction to Chaos*. 2nd ed. Pure and Applied Mathematics a Series of Monographs and Textbooks 60. Academic Press, 2004. DOI: 10.1016/C2009-0-61160-0.
- [Hir13] M. W. Hirsch, S. Smale, and R. L. Devaney. “14 - The Lorenz System”. In: *Differential Equations, Dynamical Systems, and an Introduction to Chaos (Third Edition)*. Ed. by M. W. Hirsch, S. Smale, and R. L. Devaney. Boston: Academic Press, Jan. 1, 2013, pp. 305–328. DOI: 10.1016/B978-0-12-382010-5.00014-2.
- [Hum]h A. von Humboldt. *Tagebücher Der Amerikanischen Reise IX: : Varia. Obs. Astron. de Mexico a Guanaxuato, Torullo, Toluca, Veracruz, Cuba. Voy. De La Havana à Philadelphia. Geologie de Guanaxato, Volcans de Torullo et de Toluca. Voayge de Veracruz à La Havana et de La Havana à Philadelphia. Torulla*. 19. Jh. URL: [https://digital.staatsbibliothek-berlin.de/werkansicht?PPN=PPN779884841&PHYSID=PHYS\\_0041&DMDID=DMDLOG\\_0001](https://digital.staatsbibliothek-berlin.de/werkansicht?PPN=PPN779884841&PHYSID=PHYS_0041&DMDID=DMDLOG_0001).
- [Ibr21] M. M. Ibrahim et al. “Lag Synchronization of Coupled Time-Delayed FitzHugh–Nagumo Neural Networks via Feedback Control”. In: *Sci. Rep.* 11.1 (1 Feb. 16, 2021), p. 3884. DOI: 10.1038/s41598-021-82886-x.
- [Jay63] E. T. Jaynes. *Information Theory and Statistical Mechanics*. Brandeis University Summer Institute in Theoretical Physics v. 3. Prentice Hall, 1963.
- [Kan19] L. Kang et al. “A Two-Layered Brain Network Model and Its Chimera State”. In: *Sci. Rep.* 9.1 (1 Oct. 7, 2019), p. 14389. DOI: 10.1038/s41598-019-50969-5.
- [Kan90] K. Kaneko. “Clustering, Coding, Switching, Hierarchical Ordering, and Control in a Network of Chaotic Elements”. In: *Physica D* 41.2 (Mar. 1990), pp. 137–172. DOI: 10.1016/0167-2789(90)90119-A.
- [Kan94] H. Kantz. “A Robust Method to Estimate the Maximal Lyapunov Exponent of a Time Series”. In: *Phys. Lett. A* 185.1 (Jan. 1994), pp. 77–87. DOI: 10.1016/0375-9601(94)90991-1.
- [Kat20] Y. Katoh and H. Kori. “Noise Stability of Synchronization and Optimal Network Structures”. In: *Chaos* 30.1 (Jan. 1, 2020), p. 013148. DOI: 10.1063/1.5121341.
- [Kau21] R. Kaur. “DNA Breaks Regulate Neuronal Activity: NMDA-receptor and Ionizing Radiation-Mediated DNA Double-Strand Breaks Govern Activity Regulating Early-Response Gene Expression”. Darmstadt: Technische Universität Darmstadt, 2021, 77 Seiten. DOI: 10.26083/tuprints-00019655.
- [Knu97] D. E. Knuth. *The Art of Computer Programming*. 3rd ed. Reading, Mass: Addison-Wesley, 1997. 3 pp.

- [Koř20] J. Kořenek and J. Hlinka. “Causal Network Discovery by Iterative Conditioning: Comparison of Algorithms”. In: *Chaos* 30.1 (Jan. 2020), p. 013117. DOI: 10.1063/1.5115267.
- [Kös12] J. Köster and S. Rahmann. “Snakemake—a Scalable Bioinformatics Workflow Engine”. In: *Bioinformatics* 28.19 (Oct. 1, 2012), pp. 2520–2522. DOI: 10.1093/bioinformatics/bts480.
- [Kot14] K. Kotani et al. “Population Dynamics of the Modified Theta Model: Macroscopic Phase Reduction and Bifurcation Analysis Link Microscopic Neuronal Interactions to Macroscopic Gamma Oscillation”. In: *J. R. Soc. Interface* 11.95 (June 6, 2014), p. 20140058. DOI: 10.1098/rsif.2014.0058.
- [Krao4a] A. Kraskov. *Synchronization and Interdependence Measures and Their Applications to the Electroencephalogram of Epilepsy Patients and Clustering of Data*. NIC Series 24. Jülich: NIC-Secretariat, Research Centre Jülich, 2004. 89 pp.
- [Krao4b] A. Kraskov, H. Stögbauer, and P. Grassberger. “Estimating Mutual Information”. In: *Phys. Rev. E* 69.6 (June 23, 2004), p. 066138. DOI: 10.1103/PhysRevE.69.066138.
- [Kru13] J. K. Kruschke. “Bayesian Estimation Supersedes the t Test.” In: *J. Exp. Psychol* 142.2 (2013), pp. 573–603. DOI: 10.1037/a0029146.
- [Kru56] J. B. Kruskal. “On the Shortest Spanning Subtree of a Graph and the Traveling Salesman Problem”. In: *Proc. Am. Math. Soc.* 7.1 (1956), pp. 48–50. DOI: 10.2307/2033241.
- [Kuro2] Y. Kuramoto and Battogtokh. “Coexistence of Coherence and Incoherence in Nonlocally Coupled Phase Oscillators.” In: *Nonlinear Phenom. Complex Syst.* 5.4 (2002), pp. 380–385. URL: <http://www.j-npcs.org/abstracts/vol2002/v5no4/v5no4p380.html>.
- [Kur75] Y. Kuramoto. “Self-Entrainment of a Population of Coupled Non-Linear Oscillators”. In: *Int. Symp. Math. Probl. Theor. Phys.* Ed. by H. Araki. Berlin, Heidelberg: Springer, 1975, pp. 420–422.
- [Lac99] J. P. Lachaux et al. “Measuring Phase Synchrony in Brain Signals”. In: *Hum. Brain Mapp.* 8.4 (1999), pp. 194–208. DOI: 10.1002/(sici)1097-0193(1999)8:4<194::aid-hbm4>3.0.co;2-c.
- [Law18] Z. D. Lawrence and G. L. Manney. “Characterizing Stratospheric Polar Vortex Variability With Computer Vision Techniques”. In: *J. Geophys. Res. Atmospheres* 123.3 (2018), pp. 1510–1535. DOI: 10.1002/2017JD027556.
- [Let10] C. Letellier and V. Messenger. “Influences on Otto e. Rössler’s Earliest Paper on Chaos”. In: *Int. J. Bifurcation Chaos* 20.11 (Nov. 1, 2010), pp. 3585–3616. DOI: 10.1142/S0218127410027854.
- [Li10] X. Li and G. Ouyang. “Estimating Coupling Direction between Neuronal Populations with Permutation Conditional Mutual Information”. In: *NeuroImage* 52.2 (Aug. 15, 2010), pp. 497–507. DOI: 10.1016/j.neuroimage.2010.05.003.
- [Li13] J. Li, X. Liu, and G. Ouyang. “Permutation Conditional Mutual Information and Its Application to Epileptic EEG”. In: *2013 Int. Conf. Comput. Sci. Appl.* 2013 International Conference on Computer Sciences and Applications (CSA). Wuhan, China: IEEE, Dec. 2013, pp. 733–736. DOI: 10.1109/CSA.2013.176.
- [Lop91] F. Lopes da Silva. “Neural Mechanisms Underlying Brain Waves: From Neural Membranes to Networks”. In: *Electroencephalogr. Clin. Neurophysiol.* 79.2 (Aug. 1, 1991), pp. 81–93. DOI: 10.1016/0013-4694(91)90044-5.

- [Lor63] E. N. Lorenz. "Deterministic Nonperiodic Flow". In: *J. Atmos. Sci.* 20.2 (Mar. 1, 1963), pp. 130–141. DOI: 10.1175/1520-0469(1963)020<0130:DNF>2.0.CO;2.
- [Mac03] D. J. C. MacKay. *Information Theory, Inference, and Learning Algorithms*. Vol. 7.2. Copyright Cambridge University, 2003. 640 pp. DOI: 10.1198/jasa.2005.s54.
- [Maj19] S. Majhi et al. "Chimera States in Neuronal Networks: A Review". In: *Phys. Life Rev.* 28 (Mar. 1, 2019), pp. 100–121. DOI: 10.1016/j.plrev.2018.09.003.
- [Mal03] B. G. Malkiel. "The Efficient Market Hypothesis and Its Critics". In: *J. Econ. Perspect.* 17.1 (Mar. 2003), pp. 59–82. DOI: 10.1257/089533003321164958.
- [Man99] R. N. Mantegna. "Hierarchical Structure in Financial Markets". In: *Eur. Phys. J. B* 11.1 (Sept. 1, 1999), pp. 193–197. DOI: 10.1007/s100510050929.
- [Mas01] C. Masoller and n. H. Zanette. "Anticipated Synchronization in Coupled Chaotic Maps with Delays". In: *Physica A* 300.3 (Nov. 15, 2001), pp. 359–366. DOI: 10.1016/S0378-4371(01)00362-4.
- [Mat98] M. Matsumoto and T. Nishimura. "Mersenne Twister: A 623-Dimensionally Equidistributed Uniform Pseudo-Random Number Generator". In: *ACM Trans. Model. Comput. Simul.* 8.1 (Jan. 1998), pp. 3–30. DOI: 10.1145/272991.272995.
- [Maz08] F. Mazzocchi. "Complexity in Biology". In: *EMBO Rep.* 9.1 (Jan. 1, 2008), pp. 10–14. DOI: 10.1038/sj.embor.7401147.
- [McB15] M. McBeath and R. C. Krynen. "Velocity of the Human Stadium or Mexican La Ola Wave: Systematic Variations Due to Type and Direction". In: *J. Vis.* 15.12 (Sept. 1, 2015), pp. 748–748. DOI: 10.1167/15.12.748.
- [Men18] J. H. Meng and H. Riecke. "Synchronization by Uncorrelated Noise: Interacting Rhythms in Interconnected Oscillator Networks". In: *Sci. Rep.* 8.1 (1 May 3, 2018), p. 6949. DOI: 10.1038/s41598-018-24670-y.
- [Nato4] K. Natarajan et al. "Nonlinear Analysis of EEG Signals at Different Mental States". In: *Biomed. Eng. Online* 3.1 (Mar. 16, 2004), p. 7. DOI: 10.1186/1475-925X-3-7.
- [Nemo4] I. Nemenman, W. Bialek, and R. de Ruyter van Steveninck. "Entropy and Information in Neural Spike Trains: Progress on the Sampling Problem". In: *Phys. Rev. E* 69.5 (May 24, 2004), p. 056111. DOI: 10.1103/PhysRevE.69.056111.
- [Nko13] S. Nkomo, M. R. Tinsley, and K. Showalter. "Chimera States in Populations of Nonlocally Coupled Chemical Oscillators". In: *Phys. Rev. Lett.* 110.24 (June 14, 2013), p. 244102. DOI: 10.1103/PhysRevLett.110.244102.
- [Oes07] C. Oestreicher. "A History of Chaos Theory". In: *Dialogues Clin. Neurosci.* 9.3 (Sept. 2007), pp. 279–289. DOI: 10.31887/DCNS.2007.9.3/coestreicher.
- [Olio7] T. E. Oliphant. "Python for Scientific Computing". In: *Comput. Sci. Eng.* 9.3 (2007), pp. 10–20. DOI: 10.1109/MCSE.2007.58.
- [Oli15] H. M. Oliveira and L. V. Melo. "Huygens Synchronization of Two Clocks". In: *Sci. Rep.* 5.1 (July 2015). DOI: 10.1038/srep11548.
- [Ome18] I. Omelchenko et al. "Optimal Design of Tweezer Control for Chimera States". In: *Phys. Rev. E* 97.1 (Jan. 25, 2018), p. 012216. DOI: 10.1103/PhysRevE.97.012216.
- [Ouy20] H. Ouyang, X. Xu, and G. Zhang. "Tracking and Load Sway Reduction for Double-Pendulum Rotary Cranes Using Adaptive Nonlinear Control Approach". In: *Int. J. Robust Nonlinear Control* 30.5 (2020), pp. 1872–1885. DOI: 10.1002/rnc.4854.

- [Pal01] M. Paluš et al. “Synchronization as Adjustment of Information Rates: Detection from Bivariate Time Series”. In: *Phys. Rev. E* 63.4 (Mar. 28, 2001), p. 046211. DOI: 10.1103/PhysRevE.63.046211.
- [Pal93] T. N. Palmer. “Extended-Range Atmospheric Prediction and the Lorenz Model”. In: *Bull. Am. Meteorol. Soc.* 74.1 (Jan. 1, 1993), pp. 49–66. DOI: 10.1175/1520-0477(1993)074<0049:ERAPAT>2.0.CO;2.
- [Par11] C. Park and L. L. Rubchinsky. “Intermittent Synchronization in a Network of Bursting Neurons”. In: *Chaos* 21.3 (Sept. 2011), p. 033125. DOI: 10.1063/1.3633078.
- [Pec15a] L. M. Pecora and T. L. Carroll. “Synchronization of Chaotic Systems”. In: *Chaos Interdiscip. J. Nonlinear Sci.* 25.9 (Sept. 2015), p. 097611. DOI: 10.1063/1.4917383.
- [Pec15b] L. M. Pecora and T. L. Carroll. “Synchronization of Chaotic Systems”. In: *Chaos* 25.9 (Apr. 16, 2015), p. 097611. DOI: 10.1063/1.4917383.
- [Pec90] L. M. Pecora and T. L. Carroll. “Synchronization in Chaotic Systems”. In: *Phys. Rev. Lett.* 64.8 (Feb. 1990), pp. 821–824. DOI: 10.1103/physrevlett.64.821.
- [Per11] T. K. Peron and F. A. Rodrigues. “Collective Behavior in Financial Markets”. In: *EPL* 96.4 (Nov. 2011), p. 48004. DOI: 10.1209/0295-5075/96/48004.
- [Piko1] A. Pikovsky, M. Rosenblum, and J. Kurths. *Synchronization: A Universal Concept in Nonlinear Sciences*. Cambridge: Cambridge University Press, 2001. DOI: 10.1017/CB09780511755743.
- [Pik84] A. S. Pikovskii. “Synchronization and Stochastization of Nonlinear Oscillations by External Noise”. In: *Nonlinear Turbul. Process. Phys.* (1984), p. 1601. URL: <http://adsabs.harvard.edu/abs/1984ntpp.proc.1601P>.
- [Pik97] A. Pikovsky et al. “Phase Synchronization of Chaotic Oscillations in Terms of Periodic Orbits”. In: *Chaos* 7.4 (Dec. 1997), pp. 680–687. DOI: 10.1063/1.166265.
- [Pino6] J. Pine. “A History of MEA Development”. In: *Advances in Network Electrophysiology: Using Multi-Electrode Arrays*. Ed. by M. Taketani and M. Baudry. Boston, MA: Springer US, 2006, pp. 3–23. DOI: 10.1007/0-387-25858-2\_1.
- [Pro20] A. Provata and I. E. Venetis. “Chimera States in Leaky Integrate-and-Fire Dynamics with Power Law Coupling”. In: *Eur. Phys. J. B* 93.8 (Aug. 24, 2020), p. 160. DOI: 10.1140/epjb/e2020-10252-9.
- [Qui00] R. Quian Quiroga, J. Arnhold, and P. Grassberger. “Learning Driver-Response Relationships from Synchronization Patterns”. In: *Phys. Rev. E* 61 (5 Pt A May 2000), pp. 5142–5148. DOI: 10.1103/physreve.61.5142.
- [Qui02] R. Quian Quiroga et al. “Performance of Different Synchronization Measures in Real Data: A Case Study on Electroencephalographic Signals”. In: *Phys. Rev. E* 65.4 (Mar. 15, 2002), p. 041903. DOI: 10.1103/PhysRevE.65.041903.
- [Rac17] C. Rackauckas and Q. Nie. “DifferentialEquations.jl – A Performant and Feature-Rich Ecosystem for Solving Differential Equations in Julia”. In: *J. Open Res. Softw.* 5 (May 25, 2017), p. 15. DOI: 10.5334/jors.151.
- [Ram19] G. M. Ramírez-Ávila et al. “Modeling Fireflies Synchronization”. In: *A Mathematical Modeling Approach from Nonlinear Dynamics to Complex Systems*. Ed. by E. E. N. Macau. Nonlinear Systems and Complexity. Cham: Springer International Publishing, 2019, pp. 131–156. DOI: 10.1007/978-3-319-78512-7\_8.

- [Rego4] M. H. V. V. Regenmortel. “Reductionism and Complexity in Molecular Biology”. In: *EMBO reports* 5.11 (Nov. 1, 2004), pp. 1016–1020. DOI: 10.1038/sj.embor.7400284.
- [Rod19] J. Rode et al. “Chimera States on a Ring of Strongly Coupled Relaxation Oscillators”. In: *Front. Appl. Math. Stat.* 5 (2019). DOI: 10.3389/fams.2019.00031.
- [Rös76] O. E. Rössler. “An Equation for Continuous Chaos”. In: *Phys. Lett. A* 57.5 (July 12, 1976), pp. 397–398. DOI: 10.1016/0375-9601(76)90101-8.
- [Ros96] M. G. Rosenblum, A. S. Pikovsky, and J. Kurths. “Phase Synchronization of Chaotic Oscillators”. In: *Phys. Rev. Lett.* 76.11 (Mar. 11, 1996), pp. 1804–1807. DOI: 10.1103/PhysRevLett.76.1804.
- [Ros97] M. G. Rosenblum, A. S. Pikovsky, and J. Kurths. “From Phase to Lag Synchronization in Coupled Chaotic Oscillators”. In: *Phys. Rev. Lett.* 78.22 (June 1997), pp. 4193–4196. DOI: 10.1103/physrevlett.78.4193.
- [Rub17] L. L. Rubchinsky, C. Park, and S. Ahn. “Dynamics of Intermittent Synchronization of Neural Activity”. In: *Advances in Dynamics, Patterns, Cognition: Challenges in Complexity*. Ed. by I. S. Aranson et al. Nonlinear Systems and Complexity. Cham: Springer Int. Pub., 2017, pp. 263–275. DOI: 10.1007/978-3-319-53673-6\_16.
- [Rue71] D. Ruelle and F. Takens. “On the Nature of Turbulence”. In: *Rencontres Phys.-Mathématiciens Strasbg.-RCP25 12* (1971), pp. 1–44.
- [Rul95] N. F. Rulkov et al. “Generalized Synchronization of Chaos in Directionally Coupled Chaotic Systems”. In: *Phys. Rev. E* 51.2 (Feb. 1, 1995), pp. 980–994. DOI: 10.1103/PhysRevE.51.980.
- [Run12] J. Runge et al. “Escaping the Curse of Dimensionality in Estimating Multivariate Transfer Entropy”. In: *Phys. Rev. Lett.* 108.25 (2012), pp. 1–5. DOI: 10.1103/PhysRevLett.108.258701.
- [Run19] J. Runge et al. “Detecting and Quantifying Causal Associations in Large Nonlinear Time Series Datasets”. In: *Sci. Adv.* 5.11 (Nov. 1, 2019), eaau4996. DOI: 10.1126/sciadv.aau4996.
- [Sal16] J. Salvatier, T. V. Wiecki, and C. Fonnesbeck. “Probabilistic Programming in Python Using PyMC3”. In: *PeerJ Comput. Sci.* 2 (Apr. 6, 2016), e55. DOI: 10.7717/peerj-cs.55.
- [Sal18] M. Saleh, Y. Esa, and A. Mohamed. “Applications of Complex Network Analysis in Electric Power Systems”. In: *Energies* 11.6 (6 June 2018), p. 1381. DOI: 10.3390/en11061381.
- [Sano1] J. S. Sanders and A. C. Fabian. “Adaptive Binning of X-ray Galaxy Cluster Images”. In: *Mon. Notices Royal Astron. Soc.* 325 (July 1, 2001), pp. 178–186. DOI: 10.1046/j.1365-8711.2001.04410.x.
- [San19] M. S. Santos et al. “Spike-Burst Chimera States in an Adaptive Exponential Integrate-and-Fire Neuronal Network”. In: *Chaos* 29.4 (Apr. 1, 2019), p. 043106. DOI: 10.1063/1.5087129.
- [Schoo] T. Schreiber. “Measuring Information Transfer”. In: *Phys. Rev. Lett.* 85.2 (2000), pp. 461–464. DOI: 10.1103/PhysRevLett.85.461.
- [Sch21] E. Schöll. “Chimeras in Physics and Biology: Synchronization and Desynchronization of Rhythms”. In: *Zeit Nat. Kult. Vorträge Anlässl. Jahresversamml. Am 20 21 Sept. 2019 Halle Saale* (2021). In collab. with M. Community, p. 67. DOI: 10.26164/LEOPOLDINA\_10\_00275.



- [Seto8] G. C. Sethia, A. Sen, and F. M. Atay. “Clustered Chimera States in Delay-Coupled Oscillator Systems”. In: *Phys. Rev. Lett.* 100.14 (Apr. 11, 2008), p. 144102. DOI: 10.1103/PhysRevLett.100.144102.
- [Sha48] C. E. Shannon. “A Mathematical Theory of Communication”. In: *Bell Syst. Tech. J.* 27.4 (Oct. 1948), pp. 623–656. DOI: 10.1002/j.1538-7305.1948.tb00917.x.
- [Sie14] J. Sieber, O. E. Omel’chenko, and M. Wolfrum. “Controlling Unstable Chaos: Stabilizing Chimera States by Feedback”. In: *Phys. Rev. Lett.* 112.5 (Feb. 5, 2014), p. 054102. DOI: 10.1103/PhysRevLett.112.054102.
- [Sli11] J. Slingo and T. Palmer. “Uncertainty in Weather and Climate Prediction”. In: *Philos Trans A Math Phys Eng Sci* 369.1956 (Dec. 13, 2011), pp. 4751–4767. DOI: 10.1098/rsta.2011.0161.
- [Sta16] S. Stammer, S. Katzenbeisser, and K. Hamacher. “Correcting Finite Sampling Issues in Entropy L-Diversity”. In: *Priv. Stat. Databases*. Ed. by J. Domingo-Ferrer and M. Pejić-Bach. Cham: Springer International Publishing, 2016, pp. 135–146. DOI: 10.1007/978-3-319-45381-1\_11.
- [Tas98] P. Tass et al. “Detection of n:M Phase Locking from Noisy Data: Application to Magnetoencephalography”. In: *Phys. Rev. Lett.* 81.15 (Oct. 12, 1998), pp. 3291–3294. DOI: 10.1103/PhysRevLett.81.3291.
- [Tero4] J.-n. Teramae and D. Tanaka. “Robustness of the Noise-Induced Phase Synchronization in a General Class of Limit Cycle Oscillators”. In: *Phys. Rev. Lett.* 93.20 (Nov. 12, 2004), p. 204103. DOI: 10.1103/PhysRevLett.93.204103.
- [The92] J. Theiler et al. “Testing for Nonlinearity in Time Series: The Method of Surrogate Data”. In: *Phys. Nonlinear Phenom.* 58.1-4 (1992), pp. 77–94. DOI: 10.1016/0167-2789(92)90102-S.
- [The97] The HDF Group. *Hierarchical Data Format, Version 5*. 1997. URL: <https://www.hdfgroup.org/HDF5/>.
- [Tim18] I. Timofejeva et al. “Synchronization Measure Based on a Geometric Approach to Attractor Embedding Using Finite Observation Windows”. In: *Complexity* 2018 (Aug. 8, 2018), e8259496. DOI: 10.1155/2018/8259496.
- [Tot18] J. F. Totz et al. “Spiral Wave Chimera States in Large Populations of Coupled Chemical Oscillators”. In: *Nature Phys.* 14.3 (3 Mar. 2018), pp. 282–285. DOI: 10.1038/s41567-017-0005-8.
- [Tsi09] Ch. Tsitouras. “Runge-Kutta Pairs of Orders 5(4) Using the Minimal Set of Simplifying Assumptions”. In: *AIP Conference Proceedings* 1168.1 (Sept. 9, 2009), pp. 69–72. DOI: 10.1063/1.3241561.
- [Tum17] L. Tumash et al. “Stability of Amplitude Chimeras in Oscillator Networks”. In: *EPL* 117.2 (Jan. 1, 2017), p. 20001. DOI: 10.1209/0295-5075/117/20001.
- [Ucho5] A. Uchida et al. “Synchronization and Communication with Chaotic Laser Systems”. In: *Progress in Optics*. Vol. 48. Elsevier, Jan. 1, 2005, pp. 203–341. DOI: 10.1016/S0079-6638(05)48005-1.
- [Vau10] J. Vaughan, D. Kim, and W. Singhose. “Control of Tower Cranes With Double-Pendulum Payload Dynamics”. In: *IEEE Trans. Control Syst. Technol.* 18.6 (Nov. 2010), pp. 1345–1358. DOI: 10.1109/TCST.2010.2040178.

- [Vir20] P. Virtanen et al. “SciPy 1.0: Fundamental Algorithms for Scientific Computing in Python”. In: *Nat. Methods* 17 (2020), pp. 261–272. DOI: 10.1038/s41592-019-0686-2.
- [Wan20] Z. Wang and Z. Liu. “A Brief Review of Chimera State in Empirical Brain Networks”. In: *Front. Physiol.* 11 (2020). DOI: 10.3389/fphys.2020.00724.
- [Wat98] D. J. Watts and S. H. Strogatz. “Collective Dynamics of ‘Small-World’ Networks”. In: *Nature* 393.6684 (6684 June 1998), pp. 440–442. DOI: 10.1038/30918.
- [Wic13] M. Wickramasinghe and I. Z. Kiss. “Spatially Organized Dynamical States in Chemical Oscillator Networks: Synchronization, Dynamical Differentiation, and Chimera Patterns”. In: *PLOS ONE* 8.11 (Nov. 15, 2013), e80586. DOI: 10.1371/journal.pone.0080586.
- [Wis23] J. Wissmann and K. Hamacher. “Mutual Information as a Measure for Synchronization”. In: *Rev. J. Phys. Math. Gen.* (— 2023).
- [Woj16] J. Wojewoda et al. “The Smallest Chimera State for Coupled Pendula”. In: *Sci. Rep.* 6.1 (1 Oct. 7, 2016), p. 34329. DOI: 10.1038/srep34329.
- [Wol11] M. Wolfrum and O. E. Omel’chenko. “Chimera States Are Chaotic Transients”. In: *Phys. Rev. E* 84.1 (July 8, 2011), p. 015201. DOI: 10.1103/PhysRevE.84.015201.
- [Wor15] B. Worley and R. Powers. “Generalized Adaptive Intelligent Binning of Multiway Data”. In: *Chemometr. Intell. Lab. Syst.* 146 (Aug. 2015), pp. 42–46. DOI: 10.1016/j.chemolab.2015.05.005.
- [Yah20] Yahoo. *Yahoo Finance*. June 9, 2020. URL: [finance.yahoo.com](https://finance.yahoo.com).
- [Yao17] J.-L. Yao et al. “Chaos-Based Wireless Communication Resisting Multipath Effects”. In: *Phys. Rev. E* 96.3 (Sept. 25, 2017), p. 032226. DOI: 10.1103/PhysRevE.96.032226.
- [Yel14] A. Yeldesbay, A. Pikovsky, and M. Rosenblum. “Chimeralike States in an Ensemble of Globally Coupled Oscillators”. In: *Phys. Rev. Lett.* 112.14 (Apr. 11, 2014), p. 144103. DOI: 10.1103/PhysRevLett.112.144103.
- [Yeou2] R. W. Yeung. *A First Course in Information Theory*. Information Technology–Transmission, Processing, and Storage. New York: Kluwer Academic/Plenum Publishers, 2002. 412 pp.
- [Zha13] H. Zhang, J. Liang, and Z. Chai. “Stock Prediction Based on Phase Space Reconstruction and Echo State Networks:” in: *J. Algorithms Comput. Technol.* (Mar. 1, 2013). DOI: 10.1260/1748-3018.7.1.87.
- [Zha20] Y. Zhang et al. “Critical Switching in Globally Attractive Chimeras”. In: *Phys. Rev. X* 10.1 (Feb. 24, 2020), p. 011044. DOI: 10.1103/PhysRevX.10.011044.
- [Zha21] Y. Zhang and A. E. Motter. “Mechanism for Strong Chimeras”. In: *Phys. Rev. Lett.* 126.9 (Mar. 5, 2021), p. 094101. DOI: 10.1103/PhysRevLett.126.094101.
- [Zhoo2] C. Zhou and J. Kurths. “Noise-Induced Phase Synchronization and Synchronization Transitions in Chaotic Oscillators”. In: *Phys. Rev. Lett.* 88.23 (May 28, 2002), p. 230602. DOI: 10.1103/PhysRevLett.88.230602.
- [Zhoo6] C. Zhou and J. Kurths. “Hierarchical Synchronization in Complex Networks with Heterogeneous Degrees”. In: *Chaos* 16.1 (Mar. 2006), p. 015104. DOI: 10.1063/1.2150381.
- [Zho98] C. Zhou and C.-H. Lai. “Synchronization with Positive Conditional Lyapunov Exponents”. In: *Phys. Rev. E* 58.4 (Oct. 1, 1998), pp. 5188–5191. DOI: 10.1103/PhysRevE.58.5188.

# Academic career

Name Jan Wissmann

## Career

- since 2021 **kidaton mexxon GmbH**  
Data Analyst and Developer
- 2017-2020 **Technical University Darmstadt, Germany**  
**Mathematical modeling and data analytics**  
**FB Biologie**  
Research assistant (Wissenschaftlicher Mitarbeiter )
- since 2017 **Technical University Darmstadt, Germany**  
Ph.D. candidate in the group of Prof. Dr. Kay Hamacher
- 2014 **Ege University, Izmir Turkey**  
Erasmus Scholarship
- 2014-2016 **Technical University Darmstadt, Germany**  
Master Student
- Dec. 2016 Master of Science, Physics  
Thesis:  
"Simulation of a Møller Polarimeter for the S-DALINAC in the Energy Range between 30 and 130 MeV"
- 2010 - 2014 **Technical University Darmstadt, Germany**  
Bachelor Student
- May 2014 Bachelor of Science, Physics  
Thesis:  
"Design and construction of radiation shielding for the scrapers in the extraction beamline of the S-DALINAC"

## Contributions

### 2022 **Peer Reviewed Journal**

D. Bauer, J. Wissmann, A. Moroni, G. Thiel, K. Hamacher, "Weak Cation Selectivity in HCN Channels Results From  $K^+$ -Mediated Release of  $Na^+$  From Selectivity Filter Binding Sites", *Function*, Volume 3, Issue 3, 2022, zqac019. doi:10.1093/function/zqac019

### 2016 **Conference Contribution**

L. Jürgensen , T. Bahlo, C. Burandt, T. Kürzeder, N. Pietralla, S. Weih, J. Wissmann, F. Hugh, "A high-energy-scrapersystem for the S-DALINAC extraction – Design and installation", *Proceedings of IPAC2016, Busan, Korea*, p. 101. ISBN 978-3-95450-147-2

### 2016 **Conference Contribution**

J. Wissmann, T. Bahlo, J. Enders, T. Kuerzeder, N. Pietralla "Aperture studies and detector geometry optimization for the S-DALINAC Moeller polarimeter using GEANT4", *Verhandlungen der Deutschen Physikalischen Gesellschaft v. 51(4)*. ISSN 0420-0195

### 2016 **Conference Contribution**

T. Bahlo, J. Enders, T. Kuerzeder, N. Pietralla, J. Wissmann, "Challenges in designing a very compact 130 MeV Moeller polarimeter for the S-DALINAC", *Verhandlungen der Deutschen Physikalischen Gesellschaft v. 51(4)*. ISSN 0420-0195

# Danksagung

Der größte Dank gilt natürlich meinem Doktorvater Kay. Seine Offenheit gegenüber meiner Arbeitsweise, sein Vertrauen in meine Arbeit und die vielen Hilfestellungen bei der Themenfindung haben meine Dissertation erst möglich gemacht.

Außerdem bedanke ich bei Benno Liebchen für die Übernahme des Zweitgutachtens.

Weiterhin vielen Dank an Frank, Tobi und Ben fürs Korrektur lesen und das Feedback.

Another thank you goes to Rajvinder Kaur. Thank you for the interesting and idea sparking collaboration on the activity of neurons and the discussion on your research.

Hier möchte ich auch Gerd Thiel erwähnen, der immer wieder weitere interessante Projekte mit seiner Gruppe und dann natürlich Daniel finden konnte.

Daneben gibt es natürlich noch die anderen Mitglieder meiner AG. Vielen Dank für die gute Zeit und das nette Miteinander. Neben den wissenschaftlichen Anregungen und Diskussionen waren natürlich auch die vielen Kickerrunden wichtig: Vielen Dank Micha, Tobi, Ben, Max und meinen Büronachbarn Patrick, Daniel und Philipp für die lebendige Zeit, die Bestellungen im Schnitzelhaus und Raupe<sup>41</sup>.

Wichtig zu erwähnen ist hier auch noch die Unterstützung meiner Eltern. Ihr habt während der ganzen Promotion mit mir gefiebert und mich unterstützt, immer ein offenes Ohr für mich gehabt. Und natürlich habe ich auf dem Weg dahin auch schon viele Jahre vorher auf eure Unterstützung bauen können.

Und zu guter Letzt möchte ich mich noch bei meiner Frau und Partnerin Sarah bedanken. Du bist in der finalen Phase meiner Thesis aus Kairo in mein Leben gekommen und hast dann mit mir den wahrscheinlich anstrengsten Teil meiner Arbeit miterlebt. Trotz das wir uns nur kurz kannten, hast du die ganzen Ungewissheiten und Durcheinander mit mir in kauf genommen. Danke für das Vertrauen, die Geduld und die neuen Abenteuer, die jetzt auf uns warten.